Miniaturized Microwave Cavities for Industrial Applications

THÈSE N^{O} 5493 (2012)

PRÉSENTÉE LE 5 OCTOBRE 2012

À LA FACULTÉ DES SCIENCES ET TECHNIQUES DE L'INGÉNIEUR
LABORATOIRE D'ÉLECTROMAGNÉTISME ET ACOUSTIQUE
PROGRAMME DOCTORAL EN GÉNIE ÉLECTRIQUE

ÉCOLE POLYTECHNIQUE FÉDÉRALE DE LAUSANNE

POUR L'OBTENTION DU GRADE DE DOCTEUR ÈS SCIENCES

PAR

Maddalena VIOLETTI

acceptée sur proposition du jury:

Prof. S. Süsstrunk, présidente du jury
Prof. A. Skrivervik Favre, directrice de thèse
Prof. J. Bartolic, rapporteur
Dr C. Dehollain, rapporteur
Dr L. Vietzorreck, rapporteur

ÉCOLE POLYTECHNIQUE
FÉDÉRALE DE LAUSANNE
Suisse
2012

Alla mia famiglia.

A Luca.

Abstract

Microwave cavities, or microwave resonators, are used in a variety of applications, including filters, oscillators, frequency meters, and tuned amplifiers. The ever-increasing demand for compact and/or portable telecommunication systems drives the need for further miniaturization of such structures for improved integration. In this thesis, new miniature microwave cavity solutions are proposed, which are useful in at least two scopes of application.
In the first scope, the new devices are used as microwave front-ends of a short-range radar system for on-line blade tip monitoring in gas turbines (i.e. land-based large-frame turbines, aero-derivatives and aero-engines).
In general, microwave sensors are advantageous for blade tip sensing: contrary to other existing techniques, they can survive to high temperatures for extended period of operation, unaffected by contaminants, like gases and dirt. Nonetheless, the microwave front-end of such systems is of difficult implementation, due to the strict thermal-mechanical constraints of the specific field of application (i.e. a large temperature change, the presence of vibrations, dirt and combustion by-products) and the tight requirements on the size of candidate probe designs. Antenna-based solutions are currently used as tip monitoring probes, with the disadvantage of being complex structures with radiation characteristics that are not entirely well suited for short range sensing. As a valid alternative, we propose two cavity-based probe solutions, namely a miniature waveguide resonator probe and a coaxial resonator probe, which represent an elegant compromise between robustness, miniaturization and simplicity of operation. Tests in laboratory and on real turbine engines demonstrated the suitability of such devices for the aimed application and several improved characteristics with respect to other comparable techniques, like antenna-based and eddy-current sensors.
In the second scope, the new proposed solutions are used as microwave resonators in miniature rubidium atomic clocks. Attempts to miniaturize such kind of systems are usually limited by the dimensional constraints of standard microwave cavity resonators (MWR) , which account for a large part of the volume of the physics package.
We propose a new miniature MWR based on a loop-gap resonator structure, also referred to as the μ-LGR. This cavity design meets the desired field configuration for the atomic clock operation and achieves an interesting size-reduction. A laboratory experiment of an atomic clock integrating the μ-LGR achieved unmatched results of stability compared to other microcell clocks. Finally, we propose a miniature planar MWR for the integration of 2D microfabricated cells.
Keywords: blade tip monitoring, tip clearance, tip timing, aero-derivatives, aero-engines, turbomachinery, coaxial resonators, waveguide resonators, antennas, microwave sensors, microwave cavity, atomic frequency standard, rubidium atomic clock, loop-gap resonator.

Abstract (in italiano)

Le cavità a microonde, o risonatori a microonde, sono utilizzati in una varietà di applicazioni, inclusi filtri, oscillatori, frequenzimetri, e amplificatori sintonizzati. La crescente richiesta di sistemi di telecomunicazione compatti e/o portatili richiede la miniaturizzazione di tali strutture per migliorarne l'integrazione. In questa tesi, sono proposte nuove soluzioni per cavità a microonde miniaturizzate, utili in almeno due ambiti di applicazione.
Nel primo ambito, i nuovi dispositivi a microonde sono usati come front-end di sistemi radar a corto raggio per il monitoraggio on-line del rotore di turbine a gas di varia taglia. In generale, i sensori a microonde sono vantaggiosi per questo tipo di rilevamento: contrariamente ad altre tecniche esistenti, possono sopravvivere a temperature elevate per lunghi periodi di funzionamento, indisturbati da agenti inquinanti, come gas e polveri. Tuttavia, il front-end a microonde di tali sistemi è di difficile attuazione, a causa dei severi vincoli termomeccanici del campo specifico di applicazione (cioè un ampio cambiamento di temperatura, la presenza di vibrazioni, sporco e sottoprodotti di combustione) e i requisiti stringenti sulle dimensioni delle potenziali soluzioni di sonda. Sensori basati su antenne sono attualmente utilizzati per il monitoraggio del rotore, con lo svantaggio di essere strutture relativamente complesse, con caratteristiche di radiazione che non sono interamente adatte per il rilevamento a corto raggio. Come valida alternativa, proponiamo due soluzioni basate su cavità, vale a dire una sonda basata su di un risonatore a guida d'onda e una sonda a risonatore coassiale, che rappresentano un compromesso elegante tra robustezza, miniaturizzazione e semplicità di funzionamento. Prove di laboratorio e su motori a turbina reali hanno dimostrato l'idoneità di tali dispositivi per l'applicazione mirata e diverse caratteristiche migliorate rispetto ad altre tecniche analoghe, come sensori basati su antenne e sensori a correnti parassite.
Nel secondo campo di applicazione, le nuove soluzioni proposte sono utilizzate come risonatori a microonde (MWR) miniaturizzati per orologi atomici al Rubidio. I tentativi di miniaturizzare questo tipo di sistemi sono generalmente limitati dai vincoli dimensionali dei risonatori a microonde standard, che occupano una parte considerevole del volume del pacchetto fisico. In questa tesi, proponiamo un nuovo MWR in miniatura basato su un risonatore loop-gap, a cui ci riferiamo con il nome di μ-LGR. Questo tipo di cavità ottiene la configurazione del campo desiderata per il funzionamento dell'orologio atomico e raggiunge un interessante riduzione di dimensioni. Un esperimento di orologio atomico svolto in laboratorio ed integrante il μ-LGR ha dato risultati di stabilità impareggiati da altri orologi a microcelle. Proponiamo, inoltre, una soluzione di MWR miniaturizzato planare per l'integrazione di celle 2D microfabbricate.
Parole chiave: monitoraggio del rotore, tempo di arrivo, motori a turbina, aero-derivati, risonatore a guida d'onda, risonatore coassiale, sensori ad antenna, sensori a microonde, cavità a microonde, standard di frequenza atomico, orologio atomico al rubidio, risonatore loop-gap.

Acknowledgements

I would like to acknowledge all those people that contributed to this PhD thesis work at many different levels, with their encouragement and help, and by being part of my life, beyond any distance.
First of all, I owe my deepest gratitude to my supervisor, Professor Anja K. Skrivervik, for her support and her precious advices all along this thesis, and to Professor Juan R. Mosig, who gave me the opportunity of joining LEMA and doing this work.
My genuine appreciation goes to the members of my PhD thesis jury, Professor Sabine Süsstrunk, Professor Juraj Bartolic, Professor Catherine Dehollain, and Professor Larissa Vietzorreck, who kindly accepted to review and evaluate the present work, providing me with valuable comments and remarks that greatly helped to improve the consistency of this thesis manuscript.
I would like to acknowledge Jean-François Zürcher, whose experience, sound knowledge and guidance was essential to the accomplishment of this work. I am also grateful to Philippe Vosseler, Jean-Paul Brugger and the staff of the ACI and AEM workshops at EPFL for their flawless work.
I owe my sincere estimation to my research partners Qin Xu, Michaël Hafner and Dr. Dominique Vez of the SMART project, and Christoph Affolderbach, Matthieu Pellaton, Yves Pétremand and Prof. Gaetano Mileti of the SINERGIA project for sharing their knowledge and expertise and for their close help and support.
I warmly thank Madame Eulalia Durussel for being a reference in many different ways and countless occasions.
I would also like to express my appreciation to Professor Hervé Lissek and the group of Acoustics, from whom I got interesting research perspectives during my staying at LEMA.
A very special thanks goes to Michael Mattes, for his considerate advices and remarks, and Roberto Torres, for his patience, support and priceless help in the preparation of this thesis.
My gratitude and affection goes also to my thesis mate Eden, for the walks-and-talks and his encouragements during the hard writing period.
A big hug and my warmest thoughts go to my friends in Switzerland that made my stay unique and unforgettable. Gabriela, Laleh and Ruzica, thank you for the moments we spent together, sharing our views and cheering each other up in many ways. To my LEMA people through these years, Sergio, Frédéric, Juliane, Nuno, Rafal, David, Benji, Thanos, Ioannis, Apostolos, Mohsen, Jovanche, Baptiste, Michele, to my past and present officemates Francesco, Ruzica, Marc and Eduardo, to the sporty italians Marco and Gabriele: a big thank you for all the moments we lived in and out of the lab.
I cannot forget greeting my dear mates Andrea "Coppolo", Lisa "Schnitzel", Tiago, Josh,

Valentina, Fabio and Marco "Mancio" with whom I shared laughters, trips and the most brilliant moments. I wish also to express all my affection and appreciation to a bunch of people that really made many days brighter: Alessia, Carlotta, Fabrizia, Ilaria, Marzia, Paola, Rosie, AleDiGioia, AleDeSimone, Andrea Panza, Andrea Pr18, Christian, Ciro, Livio, Luca, and Simone (i "Pourquoi Pas?").
Finally, my infinite gratitude goes to my parents Vincenzo e Chiara, for their affection, their wisdom and their unconditional support, that never failed giving me strength in every step of my life, and to my best friend and fiancé Luca, whose presence and love never ceased filling me with courage, comfort and happiness through these years, despite time and distance. To them, with all my heart, I dedicate this thesis.

Table of Contents

1 Introduction

The term *microwave* refers to signals with frequencies between 300 MHz (3×10^8 Hz) and 300 GHz (3×10^{11} Hz), Fig. 1.1 shows the microwave frequency band within the electromagnetic spectrum. The period, $T = 1/f$, of a microwave signal then ranges from 3 ns (3×10^{-9} sec) to 3 ps (3×10^{-12} sec), respectively and the corresponding electrical wavelength, $\lambda = c/f$, ranges from 1 mm to 1m (where c = 3×10^8 m/sec, the speed of light in a vacuum) [1]. In quantum physics, electromagnetic radiation is considered to be a flow of photons of energy hf, where f is the frequency and h is Planck's constant ($4.14\cdot10^{-15}$ eV or $6.63\cdot10^{-34}$ Js). Thus, a microwave photon has an energy comprised between $1.2\cdot10^{-6}$ and $1.2\cdot10^{-3}$ eV [2].

The wavelength of a microwave signal is of the same order of magnitude as the devices used to produce and transmit it. For this reason, it is not possible to assume that devices are dimensionless points in space, as it is in circuit theory approximations. Also, the voltage V is not defined in a unique way, since the electric field does not derive from a scalar potential. On the other hand it is neither possible to assume that devices become large with respect to the wavelength, as it is for geometrical optics.

Microwave problems must be considered in terms of electric and magnetic fields, as defined in Maxwell's model. It is in the nature of this model that mathematical complexity arises, as Maxwell's equations involve vector differential or integral operations on vector field quantities, and these field are functions of spatial coordinates.

Just as the high frequencies and small wavelengths of microwave energy make for difficult analysis and design of microwave components, these same factors provide unique applications for microwave systems. This is because of the following considerations:

- As antenna gain is proportional to the electrical size of the antenna, more antenna gain is possible at high frequencies, for a given physical antenna size.

- The wide frequency bands available at microwaves are favorable for radio communications. The rate of transmission of a channel is directly proportional to its bandwidth so that over the frequency range comprised between 330 MHz and 300 GHz, 999 times more information can be transmitted over a specified time period than in all the lower frequency bands taken together.

- The electromagnetic propagation within the ionosphere is similar to that in a waveguide. Signals at frequencies lower than 10-40 MHz (cut-off frequency) are partially or totally reflected, while higher frequency signals travel across ionosphere, but experience distortion, which decreases with frequency. Microwave signals, well above the ionospheric cut-off, are weakly affected, at sufficiently small power levels. For this rea-

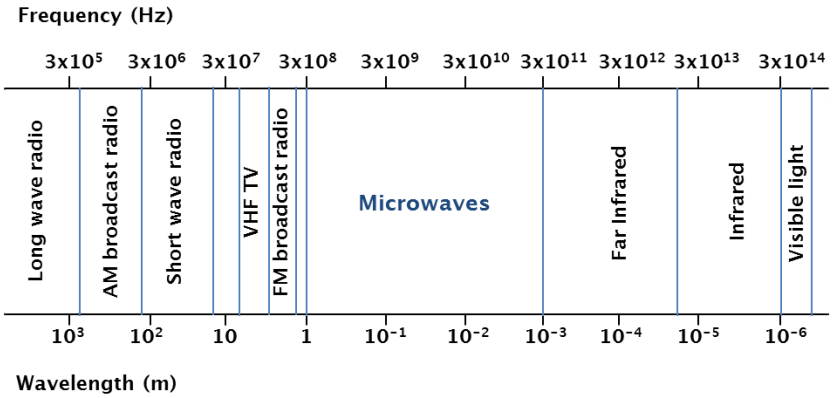

Typical Frequencies		Approx. Band Designations	
AM broadcast band	535 - 1605 KHz	L - band	1 - 2 GHz
Shortwave radio	3 - 30 MHz	S - band	2 - 4 GHz
FM broadcast band	88 - 108 MHz	C - band	4 - 8 GHz
VHF TV (2 - 4)	54 - 72 MHz	X - band	8 - 12 GHz
VHF TV (5 - 6)	76 - 88 MHz	Ku - band	12 - 18 GHz
UHF TV (7 - 13)	174 - 216 MHz	K - band	18 - 26 GHz
UHF TV (14 - 83)	470 - 890 MHz	Ka - band	26 - 40 GHz
Microwave ovens	2.45 GHz	U - band	40 - 60 GHz

Figure 1.1: The electromagnetic spectrum

son, microwaves are used for communication links (both terrestrial and with orbiting satellites) and space transmissions.

- The effective reflection area (RCS) of a radar target depends on the ratio of the object size to the wavelength. At microwave frequencies a moving targeted object will produce a distinct time-varying pattern on the received signal level, also called *motion signature*. This fact often make microwave frequencies the preferred band for radar applications.

- Several molecular, atomic and nuclear resonances occur at microwave frequencies, creating a variety of applications in the areas of science, remote sensing, medical diagnostics and treatment, and cooking methods. As an example, microwave heating is utilized for the cooking of food, the drying and thermal processing of numerous materials, the medical treatment of a number of diseases by hyperthermia, and the detection and measurement of moisture contained within materials.

- The energy of a molecular bond is several orders of magnitude larger than the energy belonging to a microwave photon. This means that, at microwave frequencies, a single photon does not possess sufficient energy to break a chemical link, for instance by photoelectric effect. This can happen at higher frequencies (in the visible spectrum, ultraviolet, X and gamma rays) where a single photon has enough energy to extract an electron and cause ionization.
  Microwaves are thus a *non-ionizing* form of radiation.

- The most stable known atomic oscillators, hydrogen, cesium, and rubidium exhibit extremely stable oscillations within the microwave range. As a result, all the atomic clocks and frequency standards utilize microwaves.

1.1 Microwaves in Industry and Science

The applications of microwaves can be divided into two categories, depending on the whether the wave is used to transmit information or just energy. The first category includes wireless communications, terrestrial and satellites communication links, radar, radioastronomy, microwave thermography, material permittivity measurements. In all cases, the transmission link incorporates a receiver whose function is to extract the information, that in some way modulates the microwave signal.
The second category of applications include microwave drying, polymerization, fusion, consolidation and treatment in general of various materials (for printing, textile, construction, pharmaceutical industries and foundries) like paper, leather, wood, concrete, ceramics, ferrites etc. Also food industry has taken advantage of microwaves for food processing (first experiments of food treating with microwaves dates back to the mid-40s [3] and it is now a well established technique) and preservation [4]. In this category of applications there is no modulating signal and the electromagnetic wave interacts directly with certain solid or liquid materials.

1.2 Microwave Sensors

The capability to measure has always been a need and an important issue in industry and science. As the production processes are becoming automatized, the measurement technology is becoming even more important, and sensors are often required to enable contactless, non destructive, on-line, and real-time measurements.
A large number of sensors available today are based on the interaction between electromagnetic energy and matter. Depending on the operating frequency, the applications and technology involved are different, ranging from moisture measurement to tomographic imaging.
Microwave sensor technology was first developed during the 1960s, but soon demonstrated to be bulky, expensive and unreliable. Moreover, there was a lack of good mathematical models suitable for understanding material properties and a need for efficient calculating and data acquisition technology. At present, microwave technology can be considered mature and data processing technologies exist that enable us to have a better sensing ability and deeper knowledge of the materials we want to measure. We know that the interaction between the EM wave and a given medium has effects on the wavefront (like attenuation, bending, delay and reflection) that depend on the relative permittivity ε_r and relative permeability μ_r and, consequently, on the physical properties of the medium. We also know that it is possible

to transmit, receive and guide microwaves in a desired way. This facts allow us to measure physical quantities using microwaves. We can classify the devices that can be found in literature into different categories, depending on how the electromagnetic interaction occurs, how it is then processed, which features of the object are to be measured. In the following, we focus on two classes of sensors, that are the subject of this work. Examples of some possible applications are given to provide the reader with an idea of the evolution and current state of the described technology:

1.2.1 Reflection and Radar Sensors

Reflection or *radar sensors* measure the signal reflected back from an object, either with contact or at distance from it. A number of properties can be extracted by the amplitude and phase of the reflection coefficient. For example, information on the roughness of the surface of the target can be obtained by the study of the back-scattered signal, the distance and relative movement of the object can be related to the Time-of-Arrival (ToA) of the reflected wave and to the change of frequency, i.e. Doppler effect. Different kinds of radar sensors exist using continuous wave or pulses, fixed or swept frequency, measuring time, amplitude or change of frequency.
Important applications are the measurement of the level of liquid in tanks in the presence of flammable and corrosive substances and dirt, thickness of underground substrates like deposition layers and ice coating and buried objects, as reported in [5, 6]. Examples of microwave sensors used for short range detection and measurement are reported for obstacles detection in automotive industry [7], measurement of plasma turbulence in nuclear experimentation [8], and monitoring displacement in mechanical devices [9].
Finally, radar sensors allows the measurement of those vibrations predicting fatigue failures, so that countermeasures can be taken. This is true in many different industrial contexts, as in [10, 11].

1.2.2 Microwave Resonator Sensors

In *resonator sensors*, the wave is sent back and forth between two reflecting discontinuities in a transmission line, eventually forming a standing wave at resonance frequencies. Frequency at which the resonance occurs depends on the resonator size in terms of wavelengths. It is, thus, affected at each passage of the wave by the real parts of the relative permittivity and permeability (ε'_r and μ'_r, , respectively) of the object to be measured, which is usually inserted in the center of the transmission line. Thanks to this, the resonator is able to amplify perturbations caused by any small and low-loss objects, providing very accurate measurement results. The speed of decay of waves (i.e. the Quality factor Q) is affected by the imaginary parts of the relative permittivity and permeability, ε''_r and μ''_r respectively.
Resonator sensors exist in a number of different shapes and sizes depending on the requirements of the application. As reported by [12], applications of hollow cavity resonators include

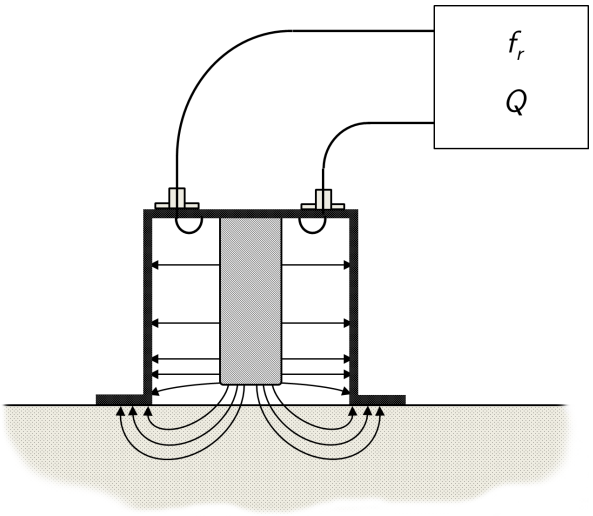

Figure 1.2: Cut view of a coaxial resonator sensor used for contact measurement of a planar surface.

scanning sensors in the UHF band, for measurement of moisture in paper-like materials, using either the fringing field radiating from an aperture or a split cavity to compare the resonant frequency of moist paper to the one of dry paper.

A very interesting and widely used example of contacting resonator sensor is the open-ended coaxial cable probe, which is held against the material to be measured, as shown in Fig. 1.2. Several authors have reported results with open-ended coaxial resonators used as probes for measurement of flat or soft surfaces [13–15]. The fields of application range from measuring the permittivity of biological substances and materials to moisture in building walls. Miniaturized versions are used in medicine for intrusive measurements. Advantages are portability, nondestructive testing of large objects, and small size of measurement area, though the method is not suitable for very rough surfaces.

Flow meters for particulate materials employing cavity resonators are able to measure speed and density of the flow, by detecting changes in resonance frequency, as in [16, 17] .

Microwave sensors for non-contacting characterization of metal objects and composites have been reported by several authors [15, 18, 19].

Air humidity in harsh environmental conditions, like in dryers and ovens, is easily measured by means of cylindrical cavities resonating in the TE_{011}, as in [20]. This mode is particularly suitable for measurements in the presence of a dirty environment. The electric field of the TE_{011} mode is zero on the walls, so that thin layers of resin or dust do not affect the sensor performance. It also allows the use of relatively simple open-end cavities, so that the air can flow through.

Several applications exist where the permittivity of a material sample is monitored while being heated or cured (e.g. epoxy) with microwaves. For example, heating can be performed with multi-mode applicators while material is monitored at a lower frequency where the

sensor acts like a single-mode cavity. Other sensors use single-mode cavities for treatment of the material and measurement on the same frequency.
Other interesting applications of hollow cavities include temperature transponders for implanted devices consisting of miniature cavities filled with dielectric of high relative permittivity ε_r, techniques to measure the piston stroke in combustion engines where the cylinder acts like a variable-length resonator as the piston moves, meters for the determination of water content in oil emulsions. Also, a number of degenerate components of the cavity resonance modes can be used to measure the characteristics of anisotropic materials.

1.2.3 Advantages and Drawbacks of Microwave Sensors

Some general considerations are possible even though the suitability of the different kinds of sensor are dependent on their field of application:

- microwave sensors do not require physical contact with the measuring object. On-line measurements are thus possible, without interference with other processes,
- microwaves are able to "see through" materials (exception made for metals). Consequently it is possible to obtain a volumetric representation of the measured object,
- microwave sensors are fairly insensitive to environmental conditions (such as the presence of vapor, rain, dust, high temperatures, corrosive substances), unlike infrared, semiconductor or optical sensors),
- at microwave frequencies, the influence of dc conductivity disappears,
- at the power levels normally used for microwave sensing, microwave are considered safe (we have non-ionizing radiation),
- the microwave sensors do not affect the characteristics or the integrity of the material under test.

On the other hand,

- components begin to be very expensive at high frequencies,
- the sensors are often adapted for a specific application and are not very versatile. For instance, microwave meters should be calibrated individually to be able to test different materials,
- the sensor can be sensitive to unwanted parameters, thus compensation is in some cases necessary,
- the centimeter wavelengths limits the achievable spatial resolution.

1.3 Miniaturization Techniques

The demand of commercial and military mobile wireless systems is ever-increasing, for which low power operation and compactness are features of paramount importance. The great level of integration achieved by solid state devices allows to realize very compact mobile wireless systems with miniaturized high-performance Transmit/Receive (T/R) modules. This fact has encouraged the development of a number of different miniaturization techniques for RF front-end devices, i.e. sensors and transducers. In this context, transducers like antennas and resonators can be put in analogy, as they are both devices used to transform electric currents in electromagnetic (EM) fields. Antennas are usually required to produce an efficient EM wave radiation, while resonators are used for the purpose of EM filtering and amplification of signals (EM field, current and voltage) for a given injected microwave power.
Similarly to resonant antennas, resonators of all the different kinds (cavities, coaxial and helical resonators, strips, two-conductor line and slot-line resonators, etc.) can be reduced in size at a given working frequency by means of a number of different techniques. Existing miniaturization approaches include meandering, folding and wrapping of the radiator metallic part; capacitive or inductive loading; shorting plates, pins or ground plane; utilization of ground slots (to widen or create new bands); dielectric or meta-materials loading (see for example [21–24].
Compact size is always achieved at the expense of the antenna performances, with deteriorated efficiency, gain, bandwidth and polarization, difficult feeding and tuning, higher losses. Study of the effect of antenna size reduction was initiated in the 40s [25–27] and has been refined by several authors [28, 29]. Similarly, size-reduced resonators can suffer of difficult feeding and tuning, higher losses leading to a poor quality factor Q, which is anyway limited by the small volume of the cavity. Of course, also a decreased range and quality of radiation is a concern when the resonator is used as a radar sensor.
In this thesis we consider different devices based on resonating cavities of different kinds. In Chapter 2 and 3 we will treat open-ended circular waveguide and coaxial resonators, used as short-range radar sensors. In this case, the approach of miniaturization privileged low-loss dielectric loading. In chapter 4 and 5 we will treat printed Loop-Gap resonators (LGR), used to produce the desired EM field distribution. Here, we use temperature-stabilized dielectric materials loading and lumped elements loading, both for size reduction and fine-tuning.

1.4 Objectives

The work presented within this manuscript has been developed in the frame of two projects:

SMART*, founded by the **Commission for Technology and Innovation (CTI)**, in collaboration with **MSS**, Switzerland.
The main objective of this project was to develop small-size high-temperature microwave

*Small Microwave Antenna for Rotating Turbo-machinery

sensors at 6 GHz and 24 GHz fulfilling the specific requirements of strategically important land-based gas turbine and aero-engines applications.

SINERGIA - MACQS[†], founded by the **Swiss National Science Foundation (FNS)**, in collaboration with the **Université de Neuchâtel (UNINE)**, Switzerland.
The main objective of this project was to develop and study the key building blocks that are required for the realization of a Miniature Atomic Clock. The project followed a multi-disciplinary approach, involving scientific teams specialized in the fields of atomic physics, microwave engineering, micro fabrication, material science, and photonics.
Website of the project: *http://macqs.epfl.ch*

The general research goal was the development of miniaturized microwave devices for industrial applications, allowing accurate and low cost sensing of different parameters.
The first objective of this thesis was the investigation and development of novel compact microwave sensors for real-time blade tip clearance (BTC) and blade tip timing (BTT) measurement in land-based gas turbines, aero-engines and aero-derivatives. These two parameters are critical for the efficiency, safety and cost-effective maintenance of rotating turbo-machinery. For instance, tighter BTC reduce air leakage over the blade tips, increasing turbine efficiency and, in the case of aircrafts-mounted rotors, allowing the engine to meet performance and thrust goals with less fuel burn and lower inlet temperatures. While producing the same performance at lower temperatures, the hot section components would have increased life-time, thus beneficially affecting the engine service life (Time on Wing, TOW) [30]. BTT measurement allows to monitor the mechanical integrity of rotating blades by providing a measure of blade vibration. By doing this, asynchronous vibrations due to rotor operational changes (e.g. blade flutter, rotating stall or compressor surge) or anomalous signals advanced blade or disk deterioration can be detected and damages can be avoided through prompt reaction [11, 31]. Simulation models and statistical methods exist for the purpose of health risk evaluation and prognosis of gas turbine blades, as reported in [32]. Nevertheless, on-line BTC and BTT measurement is necessary to enable real-time prognostics and maintenance by means of the dynamic adjustment of blade tip clearance and other parameters in the turbine hot section, which should be optimized on the basis of the working condition of the rotor. This is even more true for turbines mounted on aircrafts that experience significant operational variations through the different phases of flight. Real time health monitoring systems, such as closed-loop Active Clearance Control Systems (ACCS) systems and Non-intrusive Stress Measurement Systems (NSMS), use data provided by sensing devices mounted in the case of the turbine. The measuring probes, which are in direct view of the passing blade, experience the turbine harsh environment, with corrosive gases, dirt and temperatures from -30°C to more than 1000°C depending on the sensor location inside the turbine. For this reason they are required to operate reliably and extensively in such extreme conditions, be appropriately sealed and compact in order to avoid perturbing the turbine performance.
Many sensing technologies are used to conceive sensors for the purpose of rotor and blade

[†]Miniature Atomic Clocks and Quantum Sensors

health monitoring, based on optics [33, 34], capacitance [35–37] or inductance measurements, eddy-currents [38] and magnetic fields. Within this context, this thesis investigates and proposes different sensor devices based on microwave technology which were proven to be suitable for the measurement of BTC and BTT in land-based gas turbines (at the operating frequency f_{op} of 6 GHz), aero-engines and aero-derivatives (f_{op} = 24 GHz). The novel proposed solutions, a BTC 24 GHz waveguide resonator probe and a BTT 6 GHz coaxial resonator probe, are protected by a patent application [39]. The second objective of this thesis is the development of novel miniaturized microwave resonators (MWR) to be integrated in the physics package of compact or chip-scale atomic clocks and quantum sensors, using rubidium (^{87}Rb) atomic frequency standards (RAFS).

Atomic frequency standards (atomic clocks) achieve unmatched frequency stability over long periods of time by exploiting a well-defined atomic transition for steering the output frequency of a quartz oscillator [40]. Very compact (0.5 to 2 liters volume) atomic Rb-cell clocks are based on atoms confined in small vapor-cells and have found a large number of applications, including digital communication, navigation systems, network synchronization, and others [41]. In view of mobile and battery-powered applications, there is an increasing demand for more radically miniaturized and low-power frequency standards.

The past decade has seen rapid progress in the development of chip-scale atomic clocks (CSAC), achieving high level of integration and low power consumption, while showing a fractional frequency instability (Allan deviation) several orders of magnitude better than a quartz oscillator of comparable size and power consumption [40, 42].

Most approaches to CSAC were based on the CPT scheme [40], while the optical-microwave double-resonance (DR) scheme [41, 43] - although allowing for better clock stability - was only rarely studied [44, 45]. In the DR scheme using a ^{87}Rb cell - that will be explained more in detail in Chapter 4 - a microwave cavity is used to couple near-resonant microwave radiation to the atoms.

For the miniaturization of a DR atomic clock, the size reduction of the microwave cavity or resonator (MWR) to well below the wavelength of the atomic transition (6.835 GHz in the case of ^{87}Rb) has been a long-standing issue. Solutions were developed for Rb cells down to $\approx$1 cm size (see for example [46–48]), but only few microwave structures for mm-scale cells are reported [45].

This thesis introduces different new MWR designs, for use with 3D and 2D micro-fabricated Rb cells, as those described in [49]. Among the novel proposed solutions, a miniaturized MWR based on a printed multilayered Loop-Gap Resonator (LGR), also referred to as the μ-LGR, is protected by a patent application [50].

1.5 Outline and Original Contributions

This section summarizes the layout and the contents of the chapters of this thesis. Each chapter contains a selective literature review related to the material presented in it. The original contributions by the author are presented in Chapter 3 and Chapter 5.

Chapter 2 provides an overview on health monitoring techniques for rotating machinery (as land-based gas turbines, aero-engines and aero-derivatives) the importance of real-time blade monitoring and the challenges related to this field of application. A state of the art of existing blade monitoring techniques is given, which includes capacitive, inductive, eddy-current, optical and microwave sensors. Advantages and drawbacks of microwave sensors technology are discussed, in order to justify its suitability for the specific field of application.

In this work a number of different microwave probe solutions are investigated, either based on antennas or resonators. The theoretical aspects are reviewed, which are necessary to understand the principle of operation of such structures, and their suitability for the purpose of health monitoring of rotating machinery. Also, a comparison between antenna-based sensors and resonator-based sensors is given, in order to understand the advantages and drawbacks of the two approaches for the aimed application.

Chapter 3 the original contributions from the author are presented. The first one consists of a circular waveguide-based microwave sensor suitable for tip clearance measurement in aero-engines and aero-derivatives, at the operating frequency of 24 GHz. The second one consists of a coaxial-based microwave sensor suitable for tip timing in large-frame turbines, at the operating frequency of 6 GHz. Both sensors represent compact, robust and low cost solutions which are novel designs for the specific field of application (European patent application n° 11181622).

In order to conceive the proposed novel solutions, preliminary investigations were carried out on an existing patch antenna-based sensor, working at 5.8 GHz. The study allowed to propose another possible design consisting of a 24 GHz Planar Inverted-F Antenna (PIFA) sensor, which is presented in details.

Chapter 4 provides an overview on a second investigated field of application for microwave cavities, namely the conception of miniature microwave resonators (MWR) for Rubidium atomic clocks. In particular, we introduce Double-Resonance (DR) Rubidium (^{87}Rb) atomic frequency standards (RAFS) and provide a state of the art of the existing solutions for miniaturized MWR suitable for integration in a (^{87}Rb) atomic clock, operating at the (^{87}Rb) resonance frequency of 6.835 GHz. Theoretical concepts on microwave cavities are reviewed and the parameters relevant for the study of such structures for application in an atomic clock system are given. Finally, a specific cavity structure known as Loop-Gap Resonator (LGR) is presented, that is useful for understanding the principle of operation of the solutions proposed in Chapter 5.

Chapter 5 the original contributions from the author are presented. The first one is a new MWR design consisting of a printed multilayered LGR coupled to a coaxially fed loop-shaped micro-strip and suitable for 3D microfabricated Rubidium cells, which is

referred to as the μ-LGR (European Patent Application n° 12155696). The preliminary studies on the new MWR design, and the steps leading to an optimized solution for prototyping are discussed. Results from a laboratory atomic clock experiment with a μ-LGR prototype are also presented. Finally, other possible candidate solutions, consisting of miniature planar resonators suitable for 2D Rubidium cells, are investigated.

Chapter 6 summarizes the thesis objectives and the most relevant features of the original contributions. The results obtained are reviewed and discussed in order to propose possible improvements and perspectives for future work.

Bibliography

[1] D. M. Pozar, *Microwave Engineering.* Addison-Wesley Publishing Company, Inc., 1990.

[2] F. E. Gardiol, *Introduction to Microwaves.* Artech Hose, Inc., 1984.

[3] P. L. Spencer, "Method of treating foodstuffs," *United States Patent No. 2,495,429*, Jan. 24, 1950.

[4] J. Thuery, *Microwaves: Industrial, Scientific and Medical Applications.* Artech House, Inc., 1992.

[5] O. Edvardsson, "An fmcw radar for accurate level measurements," in *Microwave Conference, 9th European*, Sept. 1979, pp. 712 –715.

[6] P. Jakkula, P. Ylinen, and M. Tiuri, "Measurement of ice and frost thickness with an fm-cw radar," in *Microwave Conference, 10th European*, Sept. 1980, pp. 584 –587.

[7] L. Giubbolini, "A multistatic microwave radar sensor for short range anticollision warning," *Vehicular Technology, IEEE Transactions on*, vol. 49, no. 6, pp. 2270–2275, Nov. 2000.

[8] E. Mazzucato, "Microwave imaging reflectometry for the measurement of turbulent fluctuations in tokamaks," *Plasma Phys. Control. Fusion*, vol. 46, no. 1271, 2004.

[9] D. W. Holmes, "Sensors and methods for sensing displacement using radar," *United States Patent No. 5,760,731*, June 2, 1998.

[10] M. Tiuri and J. Hyyrylainen, "Microwave radar for measuring vibrations on power transmission lines," in *Microwave Conference, 13th European*, Sept. 1983, pp. 663–666.

[11] P. Tappert, M. Mercadal, and A. von Flotow, "The last few minutes prior to a fatigue blade failure in an axial compressor: Observations of blade vibration and blade lean," in *Aerospace Conference, IEEE*, Mar. 2007, pp. 1–8.

[12] E. Nyfors and P. Vainikainen, *Industrial Microwave Sensors.* Artech House, 1989.

[13] J.-F. Zürcher and F. E. Gardiol, "Nondestructive microwave measurements of materials' moisture in building walls," in *Proc. IMEKO Congress Int. Measurement Confederation, Moscow*, May 1979, pp. 393–398.

[14] D. Xu, L. Liu, and Z. Jiang, "Measurement of the dielectric properties of biological substances using an improved open-ended coaxial line resonator method," *IEEE Trans. microwave Theory Tech.*, vol. Vol. MTT-38, No. 12, 1987.

[15] R. Zoughi, *Microwave Nondestructive Testing and Evaluation.* Kluwer Academic Publishers, The Netherlands, 2000.

[16] S. Kobayashi and S. Miyahara, "A particulate flow meter using microwaves," in *Proc. IMEKO*, Prague, 1985, pp. 112 –119.

[17] A. Penirschke, M. Puentes, H. Maune, M. Schussler, A. Gaebler, and R. Jakoby, "Microwave mass flow meter for pneumatic conveyed particulate solids," in *IEEE Instrumentation and Measurement Technology Conference, I2MTC*, May 2009, pp. 583 –588.

[18] R. V. Williams, "Application of microwave techniques in the iron and steel industry," in *ISA Proc. Nat. Conf. Inst. for Iron and Steel*, 1967.

[19] S. Kharkovsky and Z. Tao, "Measurement and monitoring of gap in concrete-metal structures using microwave sensor technologies," in *IEEE InternationalInstrumentation and Measurement Technology Conference (I2MTC)*, May 2012, pp. 2440–2443.

[20] A. Toropainen, P. Vainikainen, and E. Nyfors, "Microwave humidity sensor for difficult environmental conditions," in *17th European Microwave Conference*, Sept. 1987, pp. 887 –891.

[21] A. K. Skrivervik, J. F. Zürcher, O. Staub, and J. R. Mosig, "PCS antenna design: the challenge of miniaturization," *IEEE Antennas Propag. Mag.*, vol. 43, no. 4, pp. 12–27, Aug. 2001.

[22] K. Sarabandi, R. Azadegan, H. Mosallaei, and J. Harvey, "Antenna miniaturization techniques for applications in compact wireless transceivers," *XXVIIth URSI General Assembly, Maastricht*, vol. 51, no. 3, pp. 421 – 429, Aug. 2002.

[23] R. Azadegan and K. Sarabandi, "A novel approach for miniaturization of slot antennas," *Antennas and Propagation, IEEE Transactions on*, vol. 51, no. 3, pp. 421 – 429, Mar. 2003.

[24] M. Bialkowski, A. Razali, A. Boldaji, K.-H. Cheng, and P. Liu, "Miniaturization techniques of multiband antennas for portable transceivers," in *Electromagnetics in Advanced Applications (ICEAA), 2010 International Conference on*, Sept. 2010, pp. 283 –286.

[25] H. Wheeler, "Fundamental limitations of small antennas," *Proceedings of the IRE*, vol. 35, no. 12, pp. 1479–1484, Dec. 1947.

[26] L. J. Chu, "Physical limitations of omni-directional antennas," *Journal of Applied Physics*, vol. 19, no. 12, pp. 1163–1175, Dec. 1948.

[27] R. F. Harrington, "Effect of antenna size on gain, bandwidth and efficiency," *Journal of Research of the National Bureau of Standards - D. Radio Propagation*, no. 64D, pp. 1–12, Jan.-Feb. 1960.

[28] J. S. McLean, "A re-examination of the fundamental limits on the radiation q of electrically small antennas," *Antennas and Propagation, IEEE Transactions on*, vol. 44, no. 5, p. 672, May 1996.

[29] M. Gustafsson, C. Sohl, and G. Kristensson, "Physical limitations on scattering and absorption of antennas," in *2nd European Conference on Antennas and Propagation, EuCAP*, Nov. 2007, pp. 1–6.

[30] S. B. Lattime and B. M. Steinetz, "Turbine engine clearance control systems: Current practices and future directions," in *38th AIAA Joint Propulsion Conference and Exhibit*, July 7-10, Indianapolis, IN, 2002.

[31] M. Mercadal, A. von Flotow, and P. Tappert, "Damage identification by nsms blade resonance tracking in mistuned rotors," in *Aerospace Conference, IEEE Proceedings.*, vol. 7, 2001, pp. 3263–3277.

[32] N. Goel, A. Kumar, V. Narasimhan, A. Nayak, and A. Srivastava, "Health risk assessment and prognosis of gas turbine blades by simulation and statistical methods," in *Proc. Canadian Conference on Electrical and Computer Engineering*, May 4-7, 2008.

[33] G. Sarma and J. Barranger, "Capacitance-type blade-tip clearance measurement system using a dual amplifier with ramp/dc inputs and integration," *Instrumentation and Measurement, IEEE Transactions on*, vol. 41, no. 5, pp. 674 –678, Oct. 1992.

[34] M. Drumm and W. Hause, "High performance rotor monitoring," in *Digital Avionics Systems Conference, 2000. Proceedings. DASC. The 19th*, vol. 2, 2000, pp. 6E4/1 –6E4/8.

[35] A. B. Vakhtin, S.-J. Chen, and S. M. Massick, "Optical probe for monitoring blade tip clearance," in *47th AIAA Aerospace Sciences Meeting Including The New Horizons Forum and Aerospace Exposition*, January 5-8, Orlando, FL, 2009.

[36] H. S. Dhadwal, A. Mehmud, R. Khan, and A. Kurkov, "Integrated fiber optic light probe: Measurement of static deflections in rotating turbomachinery," *Review of Scientific Instruments*, vol. 67, no. 2, pp. 546–552, Feb. 1996.

[37] T. Fabian, F. B. Prinz, and G. Brasseur, "Capacitive sensor for active tip clearance control in a palm-sized gas turbine generator," *IEEE Transactions on Instrumentation and Measurement*, vol. 54, no. 3, pp. 1133–1143, June 2005.

[38] C. Roeseler, A. von Flotow, and P. Tappert, "Monitoring blade passage in turbomachinery through the engine case (no holes)," in *Aerospace Conference Proceedings, IEEE*, vol. 6, 2002, pp. 3125–3129.

[39] M. Violetti, A. K. Skrivervik, Q. Xu, J. Geisheimer, and G. Egger, "Device and method for monitoring rotor blades of a turbine," *European Patent Application No. 11181622*, Sept. 16, 2011.

[40] S. Knappe, "MEMS atomic clocks," in *Comprehensive Microsystems*. Elsevier B.V., 2008, vol. 3.

[41] J. Camparo, "The rubidium atomic clock and basic research," *Physics Today*, pp. 33–39, Nov. 2007.

[42] *SA.45s CSAC Chip Scale Atomic Clock datasheet*, Symmetricom Inc., San Jose CA, USA, document DS/SA.45s CSAC/123010/pdf, 2010.

[43] M. Pellaton, C. Affolderbach, Y. Pétremand, N. de Rooij, and G. Mileti, "Study of laser-pumped double-resonance clock signals using a microfabricated cell," *Physica Scripta*, vol. T149, 014013, 2012.

[44] R. Lutwak *et al.*, "The chip-scale atomic clock - coherent population trapping vs. conventional interrogation," *Proc. 34th Annual Precise Time and Time Interval (PTTI) Meeting*, pp. 1–12, Dec. 2002.

[45] A. M. Braun *et al.*, "RF-interrogated end-state chip-scale atomic clock," *Proc. 39th Annual Precise Time and Time Interval (PTTI) Meeting*, pp. 233–248, Nov. 2007.

[46] H. Schweda, G. Busca, and P. Rochat, "Atomic frequency standard," *European patent EP 0561261*, 1997.

[47] J. Deng, "Subminiature microwave cavity for atomic frequency standards," *Proc. of IEEE International Frequency Control Symposium and PDA Exhibition*, pp. 85–88, 2001.

[48] B. Xia, S. Zhong, D. An, and G. Mei, "Characteristics of a novel kind of miniature cell cavity assembly for rubidium frequency standards," *IEEE Trans. on Instrum. and Measurement*, vol. 55, pp. 1000–1005, 2006.

[49] Y. Pétremand, C. Affolderbach, R. Straessle, M. Pellaton, D. Briand, G. Mileti, and N. F. De Rooij, "Microfabricated rubidium vapour cell with a thick glass core for small-scale atomic clock applications," *J. Micromech. Microeng.*, vol. 22(2), 025013, 2012.

[50] M. Violetti, C. Afforderbach, F. Merli, G. Mileti, and A. K. Skrivervik, "Microwave resonator, quantum sensor, and atomic clock," *European Patent Application No. 12155696*, February 16, 2012.

2 Health Monitoring Techniques for Rotating Machinery

2.1 Outline of the Chapter

In this chapter, we introduce a novel microwave sensing system for blade tip monitoring in gas turbines.
First, the main characteristics and principle of operation of turbine engines are presented. The importance of turbine health monitoring is discussed and an overall view on the existing monitoring approaches is given. In particular, we are interested in those systems that enable active real-time control of the tip clearance and time-of-arrival of the turbine rotating blades, namely ACCS and NSMS.
Second, we introduce a novel microwave sensor system suitable for the purpose of blade tip monitoring. The system is able to measure displacement smaller than the transmitted wavelength, thanks to a phase-based microwave measurement technique that is described in greater detail in section 2.6.1.
The system uses non-contact displacement probes mounted in the turbine shell, so that they are in direct view of the target to measure (i.e. the rotating blade tip). The conception of the end-part of the system (i.e. the measuring probes) is one of the subjects of this thesis. Two resonator-based radar sensor designs and an antenna-based sensor design (a 24 GHz circular waveguide resonator probe, a 6 GHz circular coaxial resonator probe, and a 24 GHz PIFA probe) are presented in detail in Chapter 3. In this Chapter (from Section 2.7.1) we provide the theoretical background necessary to understand the principle of operation of the proposed solutions.
Finally, we compare the resonator-based sensors with antenna-based sensors and discuss the advantages and drawbacks of the two technologies for the aimed field of application.

2.2 Turbine Engines

The most powerful and efficient engines use turbine rotors to increase their thrust. In turbine engines various pressurized propellents can be used to spin the turbine, like water, steam, air or gas. The design of the turbine largely depends on the propellent being used but the same operating principle applies for all the types of turbine. Here we will focus on turbine engine fueled by pressurized hot gas.
Gas turbines engines can be found in power plants, military and commercial aircrafts and helicopters. In all modern gas turbine engines, the engine produces its own pressurized gas by

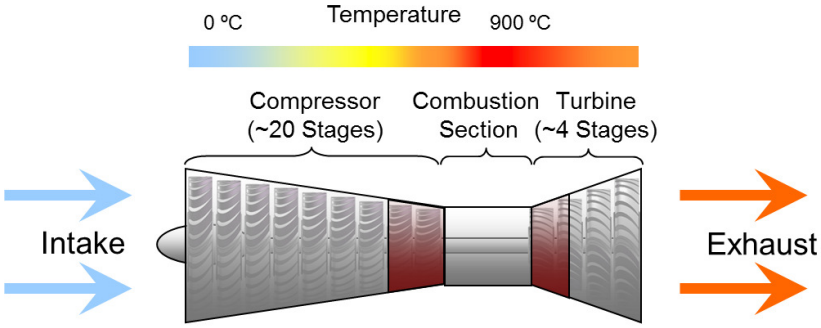

Figure 2.1: Schematics of an axial-flow jet turbine.

burning substances like propane, natural gas, kerosene or jet fuel. The heat that is produced from burning the fuel expands air, and the high-speed rush of this hot air spins the turbine. If compared to their piston counterparts, gas turbine engines can provide greater power with less weight and smaller volume. On the other hand, a gas turbine engine is much more expensive and less dynamic than a piston engine of the same size: gas turbines tend to use more fuel when they are idling, and they are less responsive at startup or to fluctuating power load.

A simple gas turbine comprises three main sections: a compressor, a combustion chamber, and a power-generating turbine, as schematized in Fig. 2.1. Air from the intake is fed through a rotating compressor stage, where a series of fan blades reduces the air volume while increasing the air pressure of a factor of ∼30. The compressed air flows into the combustion chamber, where fuel is being continuously injected. The resulting combustion creates a flow of hot, expanding gases. These gases flow over a turbine with a set of fan blades. Since the turbine is connected to the compressor by an axle, part of the power of the exhaust gases is used to drive the compressor. The shaft is then used to drive a machine or generate electricity.

The gas turbine engine operates on a thermodynamic cycle (i.e. the Brayton cycle), where atmospheric air is compressed, heated, and then expanded, with the excess of power produced by the expander (i.e. the turbine) over that consumed by the compressor used for power generation. The power produced by an expansion turbine and consumed by a compressor is proportional to the absolute temperature of the gas passing through the device. Consequently, it is advantageous to operate the expansion turbine at the highest practical temperature achievable with economic materials and internal blade cooling technology and to operate the compressor with inlet air flow at as low a temperature as possible (an inter-cooling circuit can be added at the compressor stage to further decrease the temperature of the air inlet to the combustion chamber). Gas turbine exhaust can reach temperatures of about 500°C for smaller industrial turbines and up to 600°C for aero-derivatives, while turbine hot section can touch from 800°C to over 1000°C depending on the application.

Different types of gas turbines exist, along with several ways to classify them. For the purpose

of this thesis, we will group existing rotor-based machines into three main categories, so that we can distinguish the features relevant for this work, that are blade size, temperature range of operation, and envelope or profile of operation:

- **Jet turbine engines**, generally found on civil and military aircrafts, are optimized to produce thrust from exhaust gases (turbojets). For some engines, there may be a free wheeling turbine stage on its own coaxial shaft, driving a front-mounted fan (turbofan) or propeller (turboprop).
  They are lighter and smaller compared to their land-based counterparts, reaching temperatures over 1300°C. Their operation profile is subjected to variable power loads depending on the different phases of flight (startup, shut down, restart, takeoff, re-acceleration, etc.), so that responsiveness is a priority, especially in supersonic vehicles.

- **Aero-derivatives** are basically aircraft engines adapted for electrical power generation in industrial and marine applications. As their aircraft-mounted counterparts, they can handle changing power loads more quickly and can provide a high power-to-weight ratio.

- **Large-frame industrial turbines** usually have bigger and heavier frames compared to aero-derivatives. Industrial gas turbines can be gigantic and putting them in operation can take several minutes, depending on the turbine cycle configuration (simple, combined, co-generation). Industrial turbines are used in context where efficiency (up to 60% [1]) is a priority rather than size, weight or dynamism. They are required to produce hundreds of MW of power at a stable regime even for several hours per day, depending on the demand, plant capacity and fuel costs.

In general, turbines are complex structures that can require very long production processes (more than a year for some large-frame plant turbines) and frequent and costly maintenance. The issue of preserving the structural health and improving the efficiency of such delicate machines has been investigated by several authors and groups since their introduction in industrial applications for generation of electricity and jet propulsion.
Furthermore, the ever-increasing need for powerful, efficient engines and cost-effective maintenance have pushed for research in the field of active control systems. Active control systems acquire data which are critical for the engine operation and enable closed-loop parameter control and dynamic adjustment based on the operating profile. Feedback on engine health can be derived from physical models using indirect measurements of engine parameters (like rotation speed or temperature) but the most accurate information is provided by those systems that are able to acquire in-situ real-time data from the harshest sections of the turbine, as it is explained in the following sections.

2.3 The importance of Blade Tip Monitoring

For monitoring and prognosis of turbo-machinery, an important area of interest is a means to measure in real-time the relative position of rotating parts, especially in the turbine hot

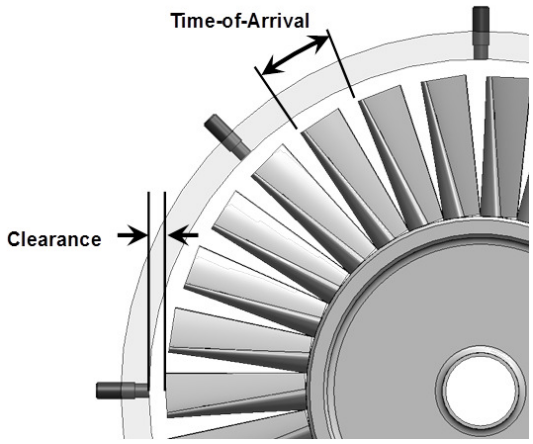

Figure 2.2: Blade tip clearance and Time-of-arrival in a turbine.

section [2]. Information on machine health is provided by the dimensional measurement of each passing blade and the rotor-case instantaneous distance (ToA and clearance in Fig. 2.2), allowing closed-loop parameter control and condition-based maintenance in inaccessible areas.

2.3.1 Blade Tip Clearance Measurement

Clearances change during operation of the engine, and vary depending on rotor speeds, temperature, and deterioration of both rotating and stationary engine parts. In particular, blade tips and shrouds wear over time, due mainly to rubbing when clearances are too tight. The deterioration of engine parts may result in increased Exhaust Gas Temperature (EGT) - which accelerates the gas path erosion process - but also in case distortion and rotor shaft bending. On the other hand, large clearances have a direct impact on engine efficiency. As an example, at the high-pressure turbine (HPT) stage, 1% of reduction in Specific Fuel Consumption (SFC) and 1°C decrease of EGT can be obtained by reducing the blade tip clearance of 0.0254 mm, as reported in [3]. By decreasing the EGT, the life of hot gas path components can be prolonged, while reducing the SFC limits NO_x and CO_2 emissions.
For these reasons real-time clearance control systems that are able to detect and dynamically reduce clearances while avoiding blade rubs represent a key tool for improvement in gas turbine design, operation and services [4].

2.3.2 Blade Tip Timing

The measurement of the blade time-of-arrival (ToA), or Blade Tip Timing (BTT), is primarily aimed to monitor the mechanical integrity of rotating blades by providing a measure of blade vibration. The measurement consists in detecting the time at which a reference point on a rotating blade tip passes a stationary point. In the absence of blade structural vibration, the

ToA only depends on the rotational speed of the blade. However, when a structural vibration occurs, the ToA depends on the amplitude, frequency and phase of vibration.
By accurately measuring the blade ToA, any anomalous signal predicting advanced blade failures can be detected and damages can be avoided through prompt reaction.
BTT is therefore a key measurement for predicting components life and enabling condition-based maintenance. It enables safety monitoring during early testing of new turbine engine designs and helps validate prototypes during development and engine testing. Finally, it enables the measurement of asynchronous vibrations caused by blade flutter, rotating stall and compressor surge.
The turbine locations where BTT brings the most benefits are the early stages of the low-pressure compressor up to the rear stages of the high-pressure compressor.

2.4 Challenges of On-line Blade Tip Monitoring

Although the need for active monitoring of turbine blade is present in literature, such measurement are difficult to make because of the nature of turbine systems. Turbine are among the most advanced and complex machines in the world, and the environment within a turbine is extremely hostile. Sensors are required to survive the turbine harsh environment while providing adequate measurements for extended periods of operation. Environmental conditions, required precision, and speed are the most challenging aspects in sensor development for turbine prognostics and clearance monitoring [5].
Measurement probes mounted in turbines must be capable of withstanding a wide range of temperatures and vibrations. Especially in aircrafts-mounted turbines, the air temperature at certain altitudes is well below 0°C, while the gas inside the combustion chamber of the turbine can reach above 1300°C. These large temperature extremes are hardly tolerable for many sensors technologies, as explained more in detail in Section 2.5. At the same time, turbine sensors must operate under vibrations for long periods of time, so that mechanical robustness and measurement sensitivity are essential.
Finally, sensors performance must not be affected by dirt and other contaminants (e.g. corrosive gases and combustion products) that are present in the hot section of a turbine. For instance, optical devices would hardly maintain quality of measurement due to the obscuration of the sensor window.
Blade tip sensing technology also requires great precision of measurement required by the applications of this data. Turbine clearances are typically on the order of 0%-4% of the total blade height [6], ranging up to 3 mm in most turbine engines. In order to manage these clearances effectively, the measurements must be significantly more precise than this, with a resolution on the order of tens of micrometers (less than 0.025 mm). Smaller turbines, like those mounted on aircrafts or aero-derivatives, need even better resolution because of scaling.
BTT measurements require high precision, in order to detect the vibrations in blades. These vibrations can range up to 0.01°, which corresponds to a tangential motion of 0.75 mm for a 50 cm turbine disk. Consequently, the sensor should have enough tangential resolution to

discriminate these small motions.
A final concern related to the implementation of turbine blade monitoring sensors is the high speed required for data processing. Military aviation turbines operate at speeds of more than 18000 rpm. Considering typical disk dimensions, with a diameter of 51 cm and 64 blades spinning at this speed, each blade will make one complete revolution once every 52 μsec, and several points must be sampled on each blade for proper analysis. Thus, a data acquisition rate of at least 5 MHz is required and data logging or processing must be fast enough to keep up with it. Advances in computation are now making this possible but still not trivial.
The algorithms that enable efficient processing of the data acquired by blade tip clearance monitoring sensors will not be treated in detail in this thesis. An overview on existing computational solutions for detecting foreign object damage (FOD), crack fatigue, and disk integrity through BTC and BTT control can be found in [7].

2.5 Existing Sensing Techniques

Various sensing technologies have been proposed to measure turbine blades during operation, including electromechanical, capacitive, eddy current, optical, and microwave probes.
Below, a non-exhaustive state-of-the-art of the most used existing methods is provided, along with the main features, advantages and drawbacks of the described solutions.

2.5.1 Electromechanical Sensors

Electromechanical devices use mechanical movement and electricity to enable measurements. One of the first developed solution [8] requires that the rotating drum is covered by a conductive coating and grounded. Then, an electrode is mechanically moved by a stepper motor towards the drum until a discharge arc is established across the gap. The clearance is derived from the voltage of the charge and the amount of movement of the motor. This solution is limited to few samples per seconds while the resolution is limited by the pass of the stepper motor. A more compact version of the described probe is proposed in [9]. The sensor endured operation at 1500°C , showing an accuracy of 25μm over a 6mm range. However, the sensor is only used to measure the longest blade, in order to avoid being hit by the disk while being mechanically moved towards the blades. Increased capabilities are obtained by attaching to the electromechanical probe a frequency modulated capacitance probe (FMCP) [6] in order to refine the measurement. The principle of operation of the FMCP is better described in the following paragraph.

2.5.2 Capacitive Sensors

Capacitive sensors measure the electrical capacitance between a probe mounted in the turbine wall and the passing blade. The rotor must be electrically conductive and ground for the method to be applicable. The capacitance is then related to the dielectric constant ε_r of the

material between the turbine shell and the blade (generally a mixture of air and gas), the area of the two facing elements S, and the clearance between the probe and the blade tip d [10], as in Eq. :

$$C = \frac{\varepsilon_r \cdot S}{d} \tag{2.1}$$

Usually, measurements are rather difficult due to the small surfaces involved and the relatively large clearances. To overcome this, the FMCP is proposed in [6] that links the value of the capacitance to a frequency modulated oscillator. With this approach, the change in capacitance drives a change in the frequency of the oscillator, which is demodulated and measured at high resolution. Then, the change in clearance is calculated by comparing the measurement with a calibration curve. A small change in clearance drives a significant change in capacitance so that the combination with an electromechanical probe is advantageous, as reported above.
An interesting solution consisting of a static FMCP is presented in [11], that achieves measurement resolution of 60 μm over a range of 203 μm. When tested in the high pressure turbine stage, the effects of temperature on the electrical properties of the probe were too important and the measurements invalid. However, further improvements of the system were carried out which are presented and discussed in a recent publication [12]
Other developments are reported, aiming to improve the spatial resolution (Drumm and Hause) and the operability of probes in the hottest sections of the turbine [10] even tough the high temperatures reaching over 1300°C present still limit the life of measuring probes. More recently, a tip clearance sensor for active clearance control for a micro gas turbine engine was developed and measured. At the high speed of these kind of turbines (around 800000 rpm), the sensor would not be able to detect clearance for each passing blade. thus, the capacitance probe rather measures the average tip clearance between the rotor blades and the casing. A surface modification of the nonconductive compressor is used so that the rotor can be treated as a single electrode opposing the casing. A measurement range of 100 μm was achieved with a resolution of 0.8 μm, as demonstrated in [13, 14].
Even though the use of capacitive sensors is the most established thanks to its robustness at high temperature the main disadvantages of this technology are the calibration effort and the limited lateral resolution of the blade edges.

2.5.3 Eddy-current Sensors

Eddy-current sensors can be active or passive, inducing currents in the targeted object in the first case, or letting target motion induce eddy currents through a static magnetic field. At blade passage, it is possible to measure the amount of these currents by measuring the change in voltage in a conductive coil. The main advantage of eddy current sensors is that they do not need drilling holes in the turbine casing to achieve blade sensing, so that the requirements on survivability towards temperature can be much lower (around 500°C). Nevertheless, the materials composing the turbine shell (that can be made of titanium, stainless steel or aluminium) have very different impact on the sensors signal [15], so that they typically need to be calibrated for the material they are sensing.

2.5.4 Optical Sensors

Optical sensors are one of the most appealing technologies for the measurement of turbine blades because of the the high speed of response and resolution, whereas the limiting factor is the processing speed of the sensor.
Solutions using laser beams reflections off the blades to obtain ToA measurements at the operation temperature of around 500 °C exist in literature, for which the scattering of light off the target can result in reduced power received by the sensor (see for instance [16]). An optical system built using low-cost semiconductors and short optical fiber bundles is presented in [17], allowing for more compact dimensions, simplicity and efficient data processing if compared to previously reported optical methods at the time of publication. In [18] tip clearance measurement is performed by detecting the apparent width of a passing blade with two integrated fiber optic probes (IFOLPs), for which tests at NASA spin rig showed an accuracy of 13 μm over a 2mm-range. Their usefulness is demonstrated at the compressor stage of the engine, while in the turbine section effectiveness and survivability of the probes is limited by high temperatures and combustion residues.
Generally, optical sensors can attain the best resolution and the highest system bandwidth; however, compared to other sensors, they are often complex, bulky, expensive, and contain alignment sensitive elements [14]. In combustion turbines, some components like optical waveguides might suffer from a limited operation temperature while the inspection window of the optical probe may be coated by combustion by-products within a short period of time. A discussion on capabilities and limitations of a system based on optical fourier domain reflectometry (OFDR), along with a comparison with other methods for blade tip measurement can be found in [19].

2.5.5 Microwave Sensors

The use of microwaves for measurements of the blade motion has been investigated by several groups of research and companies.
The device developed in [20] consists of a dielectric-filled waveguide operating at 20 GHz and is able to perform real-time tip-clearance measurement under harsh conditions, even in presence of blade rub against probe tip. The sensor presented in [21] is also dedicated to measure tip clearance at 22-24 GHz. It consists of a metallic and ceramic antenna and an electronic module incorporating microwave monolithic integrated circuits (MMIC) based on gallium arsenide (GaAs).
The microwave system described in [22] is intended for monitoring of vibrations of steam turbine blades. The generator operates at a frequency of about 24 GHz that can be adjusted by its control circuit according to the actual distance to the blades. Pulses generated by passing blades are initially processed by a digital signal processing (DSP) circuit and then

analyzed by a computer with the appropriate software for the discrete phase method.
The solution from [5, 23] operating at 5.8 GHz is distinguished by the application of two detectors with a mutual phase shift of 90°, which makes it possible to measure both the in-phase and the quadrature components of the wave vector. The addition of the second channel allows decoupling the amount of reflected energy (dependent on RCS) from phase change (dependent on the distance to the target), so that it is possible to discriminate between a change in reflectivity and a change in distance to the target. A 5.8 GHz microwave blade tip clearance probe using this system has been successfully tested on the axial vane fan and the turbofan of an engine at NASA Glenn Research Center [24]. To overcome the limits in resolution due to the radar signal wavelength in the centimeter range, the calibration of the system is discussed in [25].
Recently, an auto-focusing radar technique has been presented in [26] with the purpose of better resolving the complex shape of the rotor blade of a stationary gas turbine. A continuous wave radar in the W-band (75-110 GHz) is applied to measure the reflection at the blade tip at its passage. For resolving the blade edge reflection, the signal is then focused numerically by applying the synthetic aperture radar (SAR) principle.
The usefulness of microwave sensors for turbine blade tip clearance measurement instrumentation is discussed and demonstrated in [2]. A microwave system and method to determine an out-of-balance condition of a rotor is presented in [27] by the same author.

2.5.6 Microwaves for Blade Tip Measurement: Challenges and Objectives

The major advantages of microwave sensors for blade tip measurement are:

- their ability to operate undisturbed by combustion products, which are essentially transparent to microwaves.
- relatively good propagation of microwave radiation both in wet air and in the environment of hot exhaust gases,
- good reflection of the microwaves by metals.

On the other hand, some challenging aspects include [28]:

- expensive manufacturing process of the microwave devices, in particular those that are meant to operate at high temperatures and frequencies (above 12 GHz),
- the need to tune the operation frequency to match dimensions of the equipment and the resulting unfeasibility to develop a universal design,
- the sensor signal is usually a function of several variables, therefore the sensors need calibration, advanced processing of signals or application of a reference sensor,

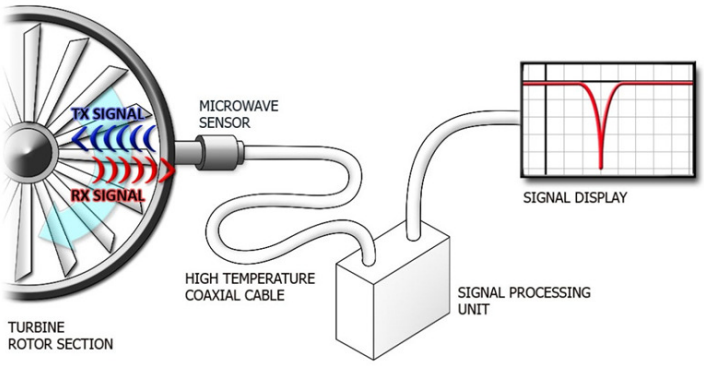

Figure 2.3: Schematics of the system

- limited spatial resolution resulting from a wavelength in the centimeter range.

The study, development and realization of a microwave sensor working at very high temperature and over a wide temperature range in a harsh environment represents a big challenge both in terms of material choice and structure. Many parameters have to be taken into account, because the high temperature affects not only the dimensions of the parts, but also the complex permittivity of the dielectrics and the conductivity of the metals. Most of the classical antenna solutions are not applicable for technological reasons.
A second challenge is the miniaturization required. Indeed for the frequencies of operation targeted in this work - 6 GHz for larger land-based gas turbines and 24 GHz for smaller aerospace engines - an outer diameter of less than 8 mm is sought for. This means a diameter of 0.14 wavelength in the lower band, which is extremely small. In the upper band the challenge resides in finding a design sufficiently robust for mechanic fabrication and dielectric tolerances due to temperature drifts, which are extremely wide especially in on-wing turbine engines.
As introduced in 1.4, one of the goals of this thesis is to propose new sensor solutions with the objective of overcoming some of the most challenging issues related to the use of microwave technology for application in power generation gas turbines and aerospace turbines. In Section 2.7 we provide an overview on the proposed solutions for the microwave system front end, which are treated in detail in Chapter 3.

2.6 System Used in This Work

The system considered in this work, which is an existing patented solution [23], works on principles that are similar to the short range radar technique [24].
The microwave sensing system measures distance by launching a continuous wave microwave signal toward a target of interest and compares the received signal with the transmitted

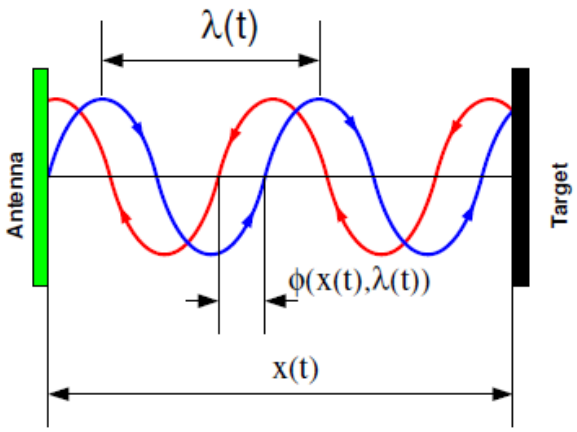

Figure 2.4: The signal transmitted by the sensor is phase-modulated by the target.

signal (see Fig. 2.3), The return signal is processed to extract the phase modulation to produce a voltage output proportional to the displacement. This technique is applicable at any microwave frequency. However, the smaller the wavelength (higher the frequency) used, the more accurate the displacement measurement when the bandwidth is held constant.

2.6.1 Measurement Principle

In the measurement system considered here, a continuous wave microwave signal (sweeping in frequency) allows the motion of the blade to phase-modulate the return signal (Fig. 2.4). A phase measurement from the return signal is compared to an internal reference signal, and changes in the phase between these signals directly correspond to changes in the displacement of the blade. The phase is related to distance by knowing the transmit frequency of the microwave signal.
The received phase ϕ can be calculated by means of the following equation where x is the distance from the sensor to the blade and λ is the transmitted signal wavelength.

$$\phi = 2\pi(\frac{2x}{\lambda}) \tag{2.2}$$

or, equivalently,

$$x = \frac{\phi\lambda}{4\pi} \tag{2.3}$$

In (2.2), the distance is multiplied by two to take into account that the wave must travel out to the blade and back to the sensor, covering twice the total distance. When the target is more than one half wavelength away, the phase could be any multiple of 360°. The actual phase measured by the sensor can only be between 0° and 360°, so if the blade is located at

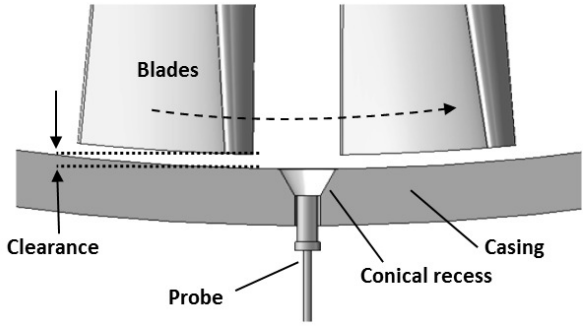

Figure 2.5: Probe installation into the turbine case.

a phase more than 360° away, there is an ambiguity as to its actual location.
For the sensors described in this work, the frequency of the transmitted signal is 6 GHz or 24 GHz, depending on the application. The half wavelengths are thus 25 mm and 6.25 mm respectively, which are sufficient to measure clearances in the targeted kinds of turbine engines and have appropriate spatial resolution to correctly detect the blade features. Standard phase unwrapping techniques can possibly be used to "count" through multiple half wavelengths when a reference wavelength location is known.

2.6.2 System Architecture

The microwave system is composed of 8 independent measurement channels operating at 6 GHz, in the version for large-frame land base turbines, or 24 GHz, in the version for smaller turbines found in aero-engines and aero-derivatives. Each channel is composed of a microwave probe installed in the engine (as it is shown in Fig. 2.5), a microwave cable and an electronics cards pair. The electronics are installed in a rack mounted inside a protective and thermally regulated enclosure located away from the hot area of the engine.

The microwave probes are connected to these electronics with 1 meter of integral high temperature cable and 7 meters of medium temperature extension cable. In addition to the microwave channels, the speed signal of the high pressure rotor is provided to the system for synchronization.
The raw signal acquisition scheme is based on period snapshots every second. Each snapshot catches exactly one rotor revolution by being synchronized with the rotor speed signal. The sensors do not make measurements in-between acquisitions and during this time signal processing is performed. Therefore, each sensor provides a tip clearance update of the rotor blades every second.
The microwave displacement measurement system is based on a frequency swept continuous-wave microwave signal which is generated by the electronics, transmitted by the probe and reflected by the blade tip back to the electronics. The reflected signal is compared to an internal reference in order to extract its phase and magnitude. A quadrature mixer architec-

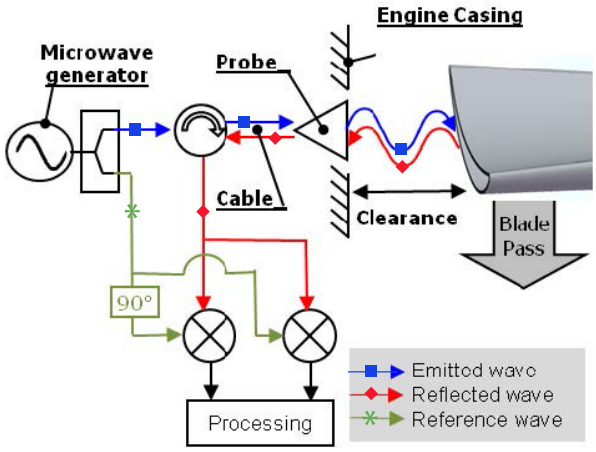

Figure 2.6: System architecture. a wave source generates an RF signal which is transmitted to the probe through a circulator. The probe sends the wave towards the passing blades and receives the wave that is reflected off at the blade tip. The reflected wave passes through the circulator and then is mixed with a reference signal from the source generator in order to get an in-phase signal I. A 90° phase shifter is used in order to get the associated quadrature signal Q. The phase φ is computed by taking the argument of the complex number I+jQ.

ture is used to extract the In-phase and Quadrature channels (baseband) from the microwave signal, as shown in Fig. 2.6. Therefore, the obtained phase is directly related to the clearance. Dedicated phase compensation signal processing allows for removing the phase contribution of the cable.
The measured clearance δ is related to the measured phase after the compensation φ_{comp} and the working wavelength λ as given in 2.4. Nevertheless, the measurement of the absolute clearance $\delta^{'}$ requires a calibration map f_{cal} which depends on probe sensitivity, blade tip geometry and installation parameters.

$$\delta = \varphi_{comp} \cdot \frac{\lambda}{4\pi} \quad \text{and} \quad \delta^{'} = f_{cal}(\delta) \tag{2.4}$$

The resonance frequency of the wave injected into the probe depends on the momentary conditions of operation of the engine such as the temperature gradient of the propagation medium of the electromagnetic wave. The sensor is configured to support the resonance frequency shift due to this gradient within the range of changing operation conditions.
The parameters of interest are both the amplitude and phase of the signal, in and out of resonance. At resonance, the EM field is radiated by the sensor and interacts with the tip of the blade, while out of resonance the EM field is not able to detect the blade, yielding a reference signal.

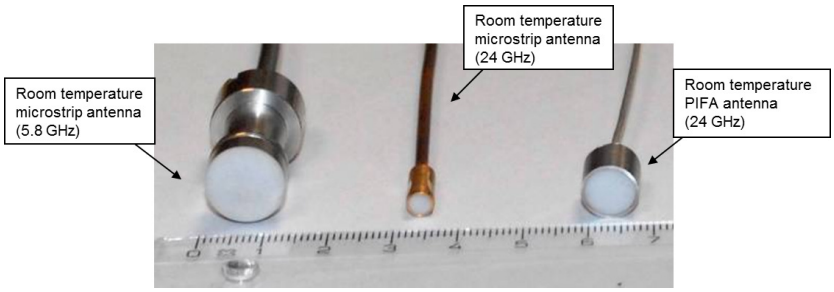

Figure 2.7: Some of the room temperature prototypes

2.7 Possible Solutions for the Microwave Front End

A system like the one described in 2.6 utilizes radiating probes mounted in the turbine case, sending an electromagnetic wave towards the passing blades and receiving the one that is reflected off at the blade tip.
For the implementation of the system front-end, different microwave solutions are possible, either based on antennas or resonators. In this work, we will describe two kinds of antenna probe designs. The first one is an existing circular patch probe [29], and the second one is a new proposed solution based on a PIFA [30].
We will also present two novel resonator-based designs, a circular waveguide resonator probe and a coaxial resonator probe [31]. Fig. 2.7 shows some of the room temperature prototypes. Possible implementations of these 4 different probes will be described detail in Chapter 3. In the following sections, we provide a review of the theoretical concepts that are useful for the treatment of the above-mentioned structures.
A comparison of the investigated solutions is provided in Section 2.7.3, in order to outline some of the advantages and drawbacks of the use of antennas and resonators as probes for the specific application considered.

2.7.1 Overview on Antenna-Based Probes

Although antenna come in an infinite variety, they all perform the same function of transducers between a guided EM wave and a free-space EM wave, and/or viceversa.
As a first consideration, we notice that the EM fields around an antenna may be divided into two principal regions, one near the antenna, called the *near field* or *Fresnel zone*, and one at a larger distance, called the *far field* or *Fraunhofer zone*. With reference to Fig. 2.8, the boundary between the two is usually placed at radius

$$R = \frac{2D^2}{\lambda} \qquad \text{(m)}, \tag{2.5}$$

where D is the maximum dimension of the antenna (in meters).
In the *far field* region, the measurable field components are transverse to the radial direction

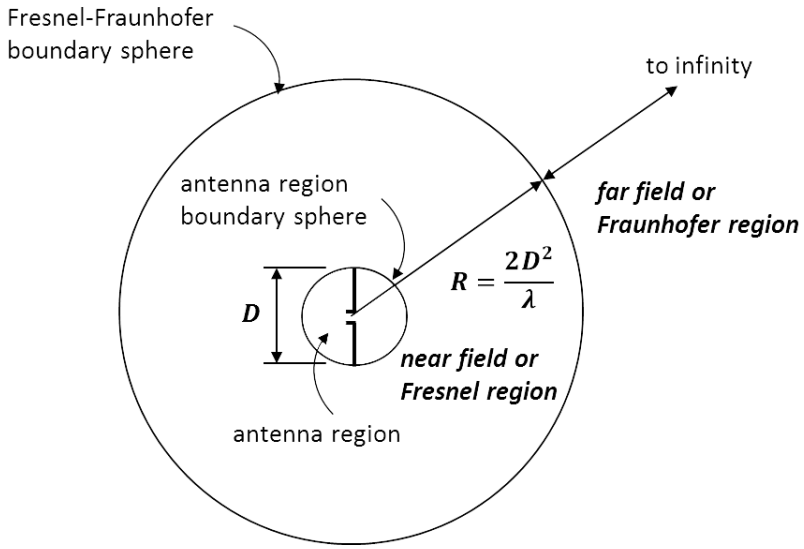

Figure 2.8: Antenna region, near field (Fresnel) region and far field (Fraunhofer) region.

from the antenna and all power flow is directed radially outward. In this region the shape of the field pattern is independent of the distance, wave propagation is consistent and wavefronts become approximately straight lines.
In the *near field* region, the longitudinal component of the electric field may be significant and power flow is not entirely radial. In this region, the shape of the field pattern depends on the distance. The EM near field can be subdivided into the *radiating* near field and the *reactive* near field. The reactive near field, that can be located within

$$d_{reactive} = \frac{\lambda}{2\pi}, \tag{2.6}$$

is rarely a region of normal operation as the interaction between the antenna and any object (e.g. the targeted blade in this work) changes the propagation characteristics of the antenna itself. A microwave turbine blade sensor operates well within the reactive near-field, introducing difficulty and uncertainty into the theoretical basis of wave propagation and reflection at these distances.
The basic parameters that direct the operation of antennas include the *radiation resistance, pattern, directivity, gain, beam area* and *aperture* [32]. Due to the short range of operation of the devices considered in this study, these concepts are not of primary interest for the application considered and will not be treated here.
Other important aspects are the band and the bandwidth of the antenna. Each antenna is designed to propagate a certain set (or band) of frequencies, while the radar waves outside the band of the antenna do not efficiently cross the aperture of the antenna to either be radiated or received by the system. The bandwidth of narrow band devices, as those considered in this

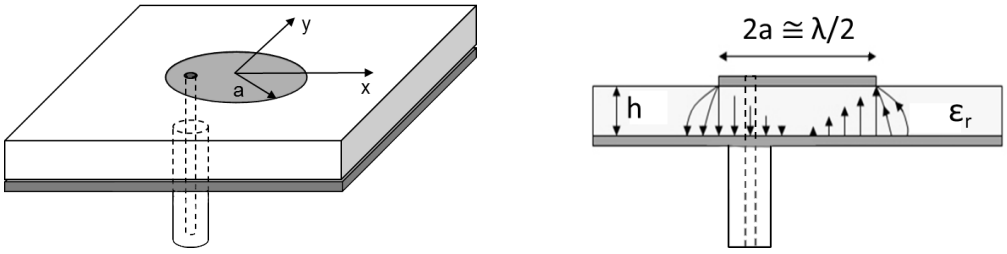

(a) (b)

Figure 2.9: Simplified structure of a circular microstrip patch antenna, (a) perspective and (b) side view.

work, can be then expressed as a percent using the following definition:

$$B = \frac{f_u - f_l}{f_c} \times 100, \tag{2.7}$$

where f_u and f_l are the upper and lower frequencies of operation for which satisfactory performance is obtained, and f_c is the center (or design) frequency. In this work, f_u and f_l are the frequencies at which the magnitude of the reflection coefficient is reduced of 3 dB with respect to its maximum value. If the bandwidth is small, the bandwidth can also be specified in terms of quality factor Q at the center frequency f_c.

2.7.1.1 Patch Antenna Probe

Microstrip antennas (MSA) are widely used in the microwave frequency region because of their simplicity and compatibility with printed-circuit technology, making them easy to manufacture either as stand-alone elements or as elements of arrays [33–35].
Their low-profile characteristics and robustness make them suitable for miniaturization, conformal applications, and low cost batch production.
In its simplest form, a microstrip patch antenna consists of a metal strip printed onto a grounded substrate (Fig. 2.9 shows a sketch of a circular patch antenna). The upper conductor of finite dimensions is deposited on top of the dielectric substrate. The shape of the patch, in principle, is arbitrary, although rectangular, circular, triangular and annular design are common in practice.
Excitation can be achieved either with a coaxial probe, stripline, or aperture electromagnetic coupling, so that a portion of the electromagnetic energy guided into the cavity region between the patch and ground plane is radiated from the patch boundary into space. The amplitude of the surface currents that flow on the conductor becomes significant when the signal frequency is close to the resonance (eigenvalue). The current patterns at resonance are the corresponding eigenfunctions, which are also called the resonance modes of the structure. Resonance starts to occur when the conductor size is of the order of a half guided wavelength,

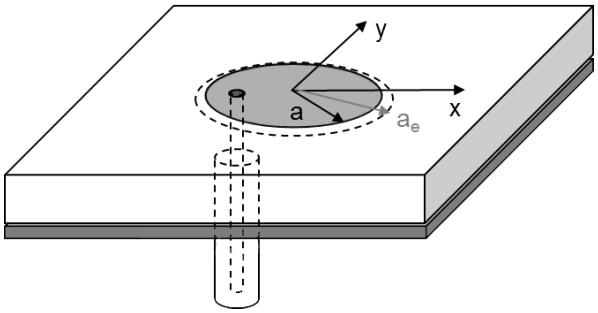

Figure 2.10: Simplified structure of a circular microstrip patch antenna and effective radius a_e

as indicated in Fig. 2.9(b).
In this work, we will limit our scope to circular geometry, providing an overview on the design procedures and important effects to be taken into account (e.g. operation at high frequencies, influence of environment and finite ground plane). Circular patches were reported to lose less energy by radiation and thus provide larger quality factors than rectangular patches [36], which is a desirable feature for operation as a resonator in a circuit but becomes a drawback when realizing antennas. The resonant frequency is determined by assuming that a perfect magnetic wall (PMC) extends under the edges of the patch. Fringing fields are taken into account by defining an effective resonator radius a_e which is slightly larger than the physical radius a [37], as shown in Fig. 2.10.
In the case of a circular MSA, the dominant mode is a TM_{110} for which the radiation patterns are given in [33, Ch. 3].
The equation for evaluating the resonant frequency of the TM_{110} of a circular MSA takes into account the radius extension a_e due to fringing effect, in agreement with the experimental values [38]:

$$f_r = \frac{p_{11} c_0}{2\pi a_e \sqrt{\epsilon_r}} \tag{2.8}$$

where

$$a_e = a\Big\{1 + \frac{2h}{\pi a \epsilon_r}(\ln\frac{\pi a}{2h} + 1.776)\Big\}^{\frac{1}{2}}, \tag{2.9}$$

$p_{11} = 1.841$ and c_0 is light velocity.
Charts showing the relationship between input impedance at edge of the resonator, dielectric constant of the substrate, unloaded Q and position of the feed point can be found in [33, Ch. 4]. By using the design charts a microstrip patch antenna can be designed in consideration of the bandwidth and the location of the feeding point can be found.

Important facts

- **Accuracy requirements:** in the microwave range of frequencies, a conducting strip becomes part of a transmission line: its width determines the characteristic impedance

of the line, while its length is related to the phase shift, proportional to the time required by any signal to travel along the line. All dimensions become significant at microwaves so that particular care during the design and fabrication is essential to ensure proper operation.

- **Mismatch at transitions:** Printed patches are connected to the outside (sources or measuring instruments) by means of microstrip-to-coaxial line transitions. While the best transition would be a smooth taper between the printed element and the input line, in practice this is not easily realizable, without involving delicate fabrication procedures (i.e. accurate positioning of the parts and soldering or bonding of small matching elements).

- **Difficult tuning:** in waveguide designs, adjustments are possible by means of tuning screws, inductive posts, or dielectric slugs. In printed elements adjustments are difficult: using miniature tunable capacitors or irreversibly removing part of the top conductor metallization is not always acceptable, which is an important drawback, especially in narrow band devices.

- **Effect of enclosure** the presence of a cover and/or sidewalls may significantly modify the antenna behavior, in particular when placed in the close vicinity. It is recommended to leave at least 10 times the substrate thickness between the circuit and the cover [39]. If this is not possible, the enclosure effect has to be accounted for in the design process. A metal enclosure in actually a microwave cavity, which resonates at some particular frequencies corresponding to its resonant modes. The size of the box should be carefully dimensioned in such a way that the signal frequency does not coincide with the unwanted resonant frequencies. When this cannot be done, spurious resonant modes can be damped by placing absorbing material (mode suppressors) at selected locations.

- **High frequency effects:** while printed circuit techniques for low-frequency electronics are well-established and have been in current use for a number of years, their extension to the range of microwaves is associated with some specific problems, requiring particular care in the design and fabrication of microstrip circuits and antennas. The standard analysis of a microstrip generally assumes that the upper conductor of a microstrip is infinitely thin and can be replaced by an equivalent surface current in the theoretical developments. On the other hand, at millimeter waves this assumption is not valid and the finite thickness of strips (few μm) must be taken into account.

In the case of the 5.8 GHz patch antenna probe treated in this work the needed degree of miniaturization required the use of a thick substrate (approx 2.5 mm thick, $\varepsilon_r \simeq 9$) with very compact dimensions (the diameter of the substrate is slightly bigger than the diameter of the patch radiator) and a metallic/ceramic shell in the close proximity of the radiating element. Thus, the effect of the enclosure and the small size of the substrate had to be accounted for in the design process (see Fig. 2.11).

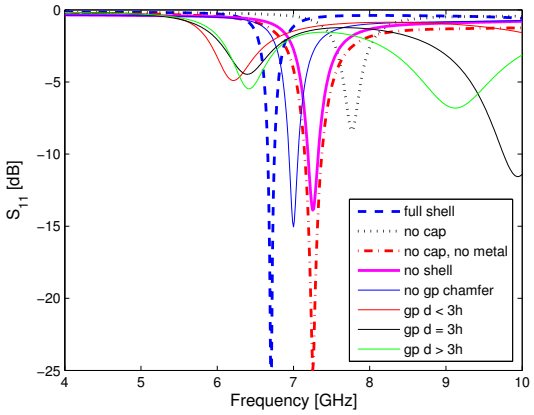

Figure 2.11: Impact of variations to the enclosure and ground plane (gp) on the patch probe response. In the figure, d is the distance between the patch and the limit of the ground plane with respect to the ground plane thickness h

2.7.1.2 Planar Inverted-F Antenna Probe

The planar inverted-F antenna (PIFA) [33, Ch. 5] is widely used in mobile communications systems thanks to its low profile, conformable structure and very compact achievable dimensions that make it suitable for integration on portable equipment such as handsets.
The PIFA typically consists of a rectangular planar element, ground plane and a short-circuit plate of narrower or equal width than that of the planar upper element. The planar element is parallel to the ground plane and fed by a pin that connects it directly to the feeding transmission line, as shown in figure 2.12.
The PIFA can also be considered as an linear Inverted-F antenna (IFA) [33, Ch. 5] with the wire radiator element replaced by a plate or as a short-circuit rectangular microstrip antenna (short-circuit MSA), which is actually a rectangular MSA resonated with the TM_{100} dominant mode. The length of the rectangular element can be halved by placing a short-circuit plate between the radiator element and the ground plane at the position where the electric field of the TM_{100} mode is zero. When the width of the short-circuit plate is set narrower than that of the planar element, the effective inductance of the antenna element increases, and the resonant frequency becomes lower than that of a conventional short-circuit MSA having the same sized planar element. As a result, the length of the PIFA can be further reduced.
The introduction of an open slot in the planar element reduces the frequency. This is due to the fact that there are currents flowing at the edge of the shaped slot, so that a capacitive loaded slot reduces the frequency and thus the antenna dimensions. The width of the short circuit plate of the PIFA plays a very important role in governing its resonant frequency. Resonant frequency decreases with the decrease in short circuit plate width, W. The resonant

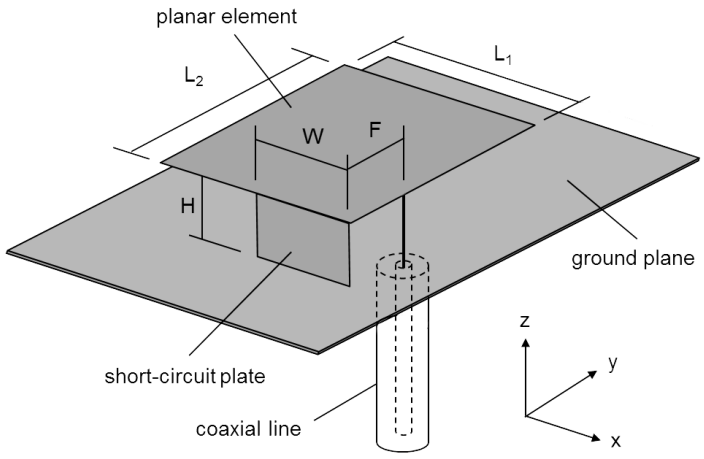

Figure 2.12: Simplified structure of a planar inverted-F antenna (PIFA).

frequency of a PIFA can be approximate with:

$$L_1 + L_2 = \frac{\lambda}{4} \tag{2.10}$$

According to the analysis results for the surface currents found in [33], one can assume that the quarter-wavelength at resonance is equal to the effective length of the current flow on the short-circuit and planar element. Then, in the case of $W/L_1 = 1$, the resonance is expressed by

$$L_2 + H = \frac{\lambda}{4}, \tag{2.11}$$

and, in the case of $W = 0$, it is expressed by

$$L_1 + L_2 + H = \frac{\lambda}{4}. \tag{2.12}$$

When the planar element height H is sufficiently shorter than the wavelength, the fringing effect in the open-circuited edge can be neglected, and the resonant frequency is calculated by (2.11) and (2.12) in agreement with measured results. The resonant frequency f_r in the case of $0 < W/L_1 < 1$, can be expressed by the following equations:

$$f_r = r \cdot f_1 + (1 - r) \cdot f_2 \ \text{ for } \ \frac{L_1}{L_2} \leq 1 \tag{2.13}$$

and

$$f_r = r^k \cdot f_1 + (1 - r^k) \cdot f_2 \ \text{ for } \ \frac{L_1}{L_2} > 1, \tag{2.14}$$

where $r = W/L_1, k = L_1/L_2$, and the resonance for frequency f_1 is given by (2.11). Resonance for frequency f_2 is expressed by

$$L_1 + L_2 + H - W = \frac{\lambda}{4}. \tag{2.15}$$

Important facts

- **Effect of enclosure:** the resonant frequency of a PIFA mounted on an infinite ground plane varies with the width of the short-circuit plate and size ratio of the planar element. However, when a PIFA is mounted on a non-ideal ground plane (e.g. the conductive housing of a handset) its characteristics are strongly affected by the size and shape of the enclosure. Therefore, it is very difficult to rigorously express the general resonant condition. At present, the size of the PIFA is individually designed by the rule of trial-and-error. Some guidelines useful in the design of a PIFA for applications requiring a small ground plane can be found in [40].

2.7.2 Overview on Resonator-Based Probes

In this work, we implemented solutions that consist of microwave resonators formed by a section of a transmission line bounded by impedance discontinuities. In particular, we considered the cases of open-ended circular waveguide resonators and open-ended coaxial resonators with longitudinal resonances.
In the following, we review the main theoretical aspects useful for the treatment of the above-mentioned structures, namely some general theory of microwave resonators, cylindrical waveguides and coaxial lines. Then we focus on the open-ended waveguide and coaxial resonators used in this work. A equivalent transmission line representation of the resonator-based probes is proposed, along with a discussion on the EM radiation characteristics and predicted trends of such structures.

In general, the role of impedance discontinuities in transmission lines microwave resonators is to cause the propagating waves to be reflected. Where the transmission line is open-circuited, the reflection coefficient is $\Gamma = +1$, and where the line is short-circuited, $\Gamma = -1$ (Fig. 2.13). If the impedance at the discontinuity differs from those mentioned above, the reflection may be partial ($0 \leq |\Gamma| \leq 1$) and the resonator leaky, or the phase angle of Γ may differ from 0° ($\Gamma = +1$) or 180° ($\Gamma = -1$).
The field in the resonator is excited by the external circuit through some kind of coupling, which can be obtained for example through an aperture, coupling loop, or coupling probe (See Sections 2.7.2.7 and 2.7.2.7). The coupling device radiates a wave into the resonator. The wave propagates along the transmission line and is reflected in alternating directions at the discontinuities.
Resonance occurs if the exciting field is in phase with the reflected components. Hence they will interfere constructively or destructively to give a standing wave pattern. This will

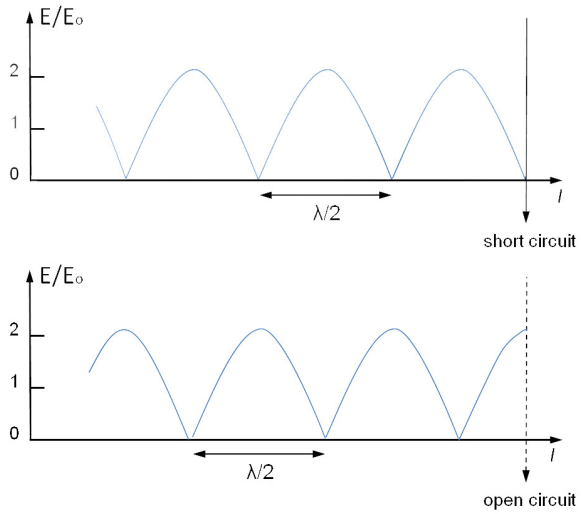

Figure 2.13: A wave of amplitude E_0, propagating in free space or along a transmission line, is reflected from a short circuit or an open circuit. The wave components, traveling in different directions, combine to form a standing wave with local maxima and zeros.

happen only at certain frequencies, where the resonance condition is fulfilled.
A standing wave with a strong field will build up, thus storing a great amount of energy. Equilibrium is reached at the level where the loss of power in the resonator (in the metal or dielectric, by radiation, or by escaping through the couplings) equals the excitation power. At resonance, the energy alternates between the electric and magnetic field, which also contain the same amount of energy.
The resonance condition is fulfilled when the mode wavelength compared to the dimensions of the resonator takes specific values, depending on the kind of terminations which bound the resonator. The reflected wave components are in phase with the exciting field if the total phase change experienced by the wave on its way back and forth along the transmission line, is a multiple of 2π:

$$\frac{2\pi}{\lambda} \cdot 2l + \phi_1 + \phi_2 = n \cdot 2\pi \tag{2.16}$$

or, equivalently,

$$l = \left(\frac{n}{2} - \frac{\phi_1 + \phi_2}{4\pi}\right)\lambda \tag{2.17}$$

where l is the length of the transmission line, ϕ_1 and ϕ_2 are the phase angles of the reflection coefficients at the terminations of the line, and n is an integer.
If the resonator is open-circuited at both ends, $\phi_1 = \phi_2 = 0$, and we obtain:

$$l = \frac{n\lambda}{2} = \frac{1}{2}\lambda, \lambda, \frac{3}{2}\lambda, 2\lambda... \tag{2.18}$$

Same result is obtained if the resonator is short-circuited at both ends, with $\phi_1 = \phi_2 = \pi$:

$$l = \Big(\frac{n}{2} - \frac{1}{2}\Big)\lambda = \frac{1}{2}\lambda, \lambda, \frac{3}{2}\lambda, 2\lambda... \tag{2.19}$$

If the resonator is short-circuited at one end and open-circuited at the other, then $\phi_1 = \pi$ and $\phi_2 = 0$ and we obtain:

$$l = \Big(\frac{n}{2} - \frac{1}{4}\Big)\lambda = \frac{1}{4}\lambda, \frac{3}{4}\lambda, \frac{5}{4}\lambda, \frac{7}{4}\lambda... \tag{2.20}$$

Therefore, an infinite series of solutions exists that satisfies the resonance condition or, in other words, each resonator has an infinite number of resonant frequencies for each wave mode.
For exact calculation of the resonant frequency, it must be noticed that the relationship between the wavelength and frequency is simple for plane waves and TEM waves, while it must be adjusted for guided waves because the wavelength of a waveguide mode is always longer than the corresponding plane wave. Equations (2.18)-(2.20) can be rewritten substituting $\lambda = \lambda_g$, where λ_g is the guide wavelength from 2.3.

2.7.2.1 Quality Factor

A resonance is characterized by two features, the resonant frequency f_r and the quality factor Q. The latter is defined as

$$Q = \frac{2\pi \times \text{energy stored in the resonator}}{\text{energy dissipated during one cycle}} = \frac{\omega \times \text{total stored energy}}{\text{loss power per cycle}} \tag{2.21}$$

The loss power can be divided into a number of terms, depending on the source of the loss. We can write the Q-factor as:

$$\frac{1}{Q_u} = \frac{1}{Q_d} + \frac{1}{Q_m} + \frac{1}{Q_{rad}} \tag{2.22}$$

where Q_u is the unloaded quality factor, Q_d accounts for the loss in the dielectric, Q_m accounts for the loss in the metallic parts, and Q_{rad} accounts for the loss through radiation.
In order to measure the resonant frequency f_c and quality factor Q_l, the resonator must be connected to the measurement circuit through some coupling. By doing this, part of the stored energy will be dissipated through the coupling device. To account for this loss we add the term Q_{ext}, obtaining the loaded quality factor Q_l:

$$\frac{1}{Q_l} = \frac{1}{Q_u} + \frac{1}{Q_{ext}} = \frac{1}{Q_d} + \frac{1}{Q_m} + \frac{1}{Q_{rad}} + \frac{1}{Q_{ext}}. \tag{2.23}$$

As mentioned in Section 2.7.2, we can think of a microwave resonator as part of a transmission line bounded by two discontinuities, so that we can express Q_u in terms of the transmission

line parameters (propagation factor $\gamma = \alpha + j\beta$), as

$$\frac{1}{Q_u} = \frac{1}{\beta l}\Big\{2\alpha l - \Big[1 - \Big(\frac{f_c}{f}\Big)^2\Big](\log_e|\Gamma_1| + \log_e|\Gamma_2|)\Big\} \tag{2.24}$$

where Γ_1 and Γ_2 are the reflection coefficients at the discontinuities.
We can measure f_c and Q_l by the method of reflection coefficient, requiring only one coupling or by the method of insertion loss, which requires two couplings and will not be treated in this work. In the method of reflection coefficient, a wave is transmitted along the cable toward the resonator and the reflected power is measured. The ratio between reflected and incident power is the power reflection coefficient $|\Gamma|^2$. With reference to the equivalent circuit of Fig. 2.23, the amplitude $|\Gamma|^2$ and phase ϕ of the power reflection coefficient near the resonant frequency can be approximated as

$$|\Gamma|^2 = 1 - \frac{4\frac{Q_l}{Q_u}\Big(1 - \frac{Q_l}{Q_u}\Big)}{1 + Q_l^2\Big(\frac{f}{f_r} - \frac{f_r}{f}\Big)^2}, \tag{2.25a}$$

$$\phi = \phi_0 - \arctan\left[\frac{2Q_l\Big(\frac{f}{f_r} - \frac{f_r}{f}\Big)\Big(1 - \frac{Q_l}{Q_u}\Big)}{2\frac{Q_l}{Q_u} - 1 + Q_l^2\Big(\frac{f}{f_r} - \frac{f_r}{f}\Big)^2}\right], \tag{2.25b}$$

where ϕ_0 is a constant that depends on the way of coupling. For coupling loops, apertures and short-circuit-like devices (inductive coupling) $\phi_0 \simeq 180^\circ = \pi$ radians, and for coupling probes (capacitive coupling) $\phi_0 \simeq 0$, in the undercoupled case ($Q_e > Q_u$). For overcoupled resonators, ($Q_e < Q_u$), 180° should be added to the values given above.
The loaded quality factor Q_l is defined as

$$Q_l = \frac{f_r}{B_{hp}} \tag{2.26}$$

where B_{hp} is measured halfway down the peak of the power reflection response, located at resonant frequency f_r.
The unloaded quality factor can be calculated from Q_l and the power reflection coefficient at resonant frequency $|\Gamma|_r^2$, as

$$Q_u = \frac{2Q_l}{1 \pm |\Gamma|_r^2} \quad \begin{cases} + & \text{undercoupled} \\ - & \text{overcoupled} \end{cases} \tag{2.27}$$

We can conveniently define a coefficient of coupling, K, as

$$K = \frac{Q_u}{Q_{ext}} \tag{2.28}$$

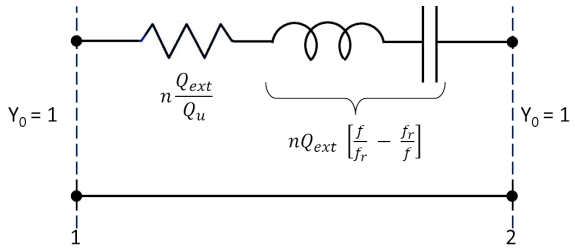

(a)

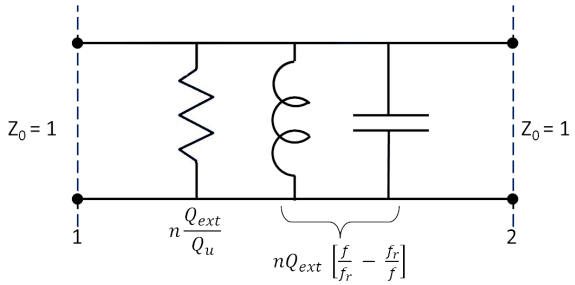

(b)

Figure 2.14: The normalized equivalent circuit of resonators. Normally, $(f/f_r - f_r/f \approx 2\Delta f/f_r)$. (a) Admittance with inductive coupling (reflection: port 2 open, $n = 1$, transmission: $n = 2$. (b) Impedance with capacitive coupling (reflection: port 2 open, $n = 1$, transmission: $n = 2$.)

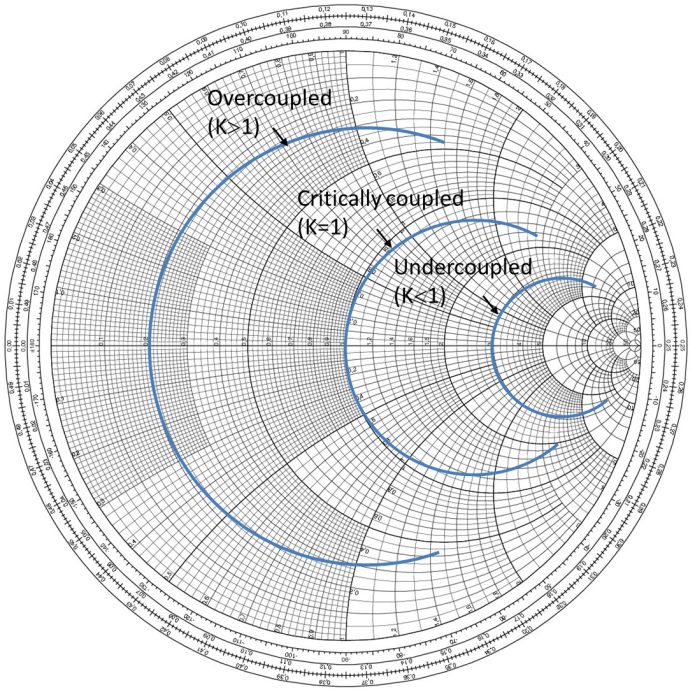

Figure 2.15: Smith chart illustrating coupling to a series RLC circuit.

which can be applied to both series ($K = Z_0/R$) and parallel ($K = R/Z_0$) resonant circuits. Then, three cases can be distinguished, as shown in Fig. 2.15:

- $K < 1$ The resonator is undercoupled to the feed line.
- $K = 1$ The resonator is critically coupled to the feed line.
- $K > 1$ The resonator is overcoupled to the feed line.

2.7.2.2 Dielectric Filled Resonators

The wavelength at a specific frequency depends on the physical properties of the propagation medium, as is evident from (2.29).
In addiction to causing attenuation (see Section 2.7.2.5), a dielectric medium also affects propagating microwaves in terms of wavelength. For nonmagnetic (with relative permeability $\mu_r = 1$), low loss ($\epsilon_r^{''} \ll \epsilon_r^{'}$) dielectric materials, which is most often the case, we have

$$\lambda = \frac{1}{Re\{f\sqrt{\mu_r\epsilon_r}\}} = \frac{1}{f\sqrt{\mu_0\epsilon_0}Re\{\sqrt{\epsilon_r}\}} = \frac{\lambda_0}{Re\{\sqrt{\epsilon_r}\}} \approx \frac{\lambda_0}{\sqrt{\epsilon_r^{'}}}. \tag{2.29}$$

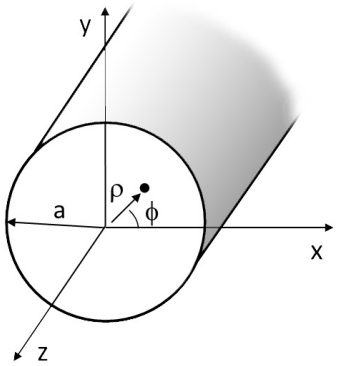

Figure 2.16: Circular waveguide geometry.

Because $\epsilon_r^{'} \gg 1$ (except for plasma), the wavelength is always shorter in a dielectric medium than in vacuum (for the same reason, the speed of propagation is lower than in vacuum, with $c = \lambda f \approx 2\pi f / k_0 \sqrt{\epsilon_r^{'}} = c_0 / \sqrt{\epsilon_r^{'}}$).
As a consequence, if a resonator is filled with dielectric, the resonance condition will be met at a lower frequency compared to a hollow resonator. Combining (2.29) with wavelength requirement for resonance, we obtain the change in resonant frequency caused by the presence of the dielectric filling as

$$\frac{1}{f_{r0}\sqrt{\mu_0 \epsilon_0}} = \frac{1}{f_r \sqrt{\mu_0 \epsilon_0 Re\{\sqrt{\epsilon_r}\}}} \tag{2.30a}$$

$$Re\{\sqrt{\epsilon_r}\} = \frac{f_{r0}}{f_r} \tag{2.30b}$$

where f_{r0} is the resonant frequency in a hollow resonator and f_r that of the filled resonator. For $\epsilon_r^{''} \ll \epsilon_r^{'}$, (2.30b) becomes

$$\epsilon_r^{'} = \left(\frac{f_{r0}}{f_r}\right)^2. \tag{2.31}$$

2.7.2.3 Circular Waveguides

A circular waveguide in its simplest form consists of an empty metal tube of circular cross-section (as shown in Fig. 2.16) that supports TE and TM waveguide modes. For such a cylindrical geometry, it is appropriate to use a use a cylindrical coordinates system. The cylindrical components of the transverse fields can be derived from the longitudinal compo-

nents as [41]:

$$E_\rho = \frac{-j}{k_c^2}(\frac{\beta\partial E_z}{\partial\rho} + \frac{\omega\mu}{\rho}\frac{\partial H_z}{\partial\phi}), \tag{2.32a}$$

$$E_\phi = \frac{-j}{k_c^2}(\frac{\beta}{\rho}\frac{\partial E_z}{\partial\phi} + \omega\mu\frac{\partial H_z}{\partial\rho}), \tag{2.32b}$$

$$H_\rho = \frac{j}{k_c^2}(\frac{\omega\epsilon}{\rho}\frac{\partial E_z}{\partial\phi} - \beta\frac{\partial H_z}{\partial\rho}), \tag{2.32c}$$

$$H_\phi = \frac{-j}{k_c^2}(\omega\epsilon\frac{\partial E_z}{\partial\phi} + \frac{\beta}{\rho}\frac{\partial H_z}{\partial\phi}), \tag{2.32d}$$

where $k_c^2 = k^2 - \beta^2$ and considering $e^{-j\beta z}$ propagation.

TE Modes For TE modes, $E_z = 0$ and H_z is a solution to the wave equation

$$\nabla^2 H_z + k^2 H_z = 0. \tag{2.33}$$

Assuming $H_z(\rho,\phi,z) = h_z(\rho,\phi)e^{-j\beta z}$, (2.33) can be expressed in cylindrical coordinates as

$$(\frac{\partial^2}{\partial\rho^2} + \frac{1}{\rho}\frac{\partial}{\partial\rho} + \frac{1}{\rho^2}\frac{\partial^2}{\partial\phi^2} + k_c^2)h_z(\rho,\phi) = 0. \tag{2.34}$$

Using the separation of variables, we substitute $h_z(\rho,\phi) = R(\rho)P(\phi)$ into (2.34). After calculations, we find

$$\rho^2\frac{d^2R}{d\rho^2} + \rho\frac{dR}{d\rho} + (\rho^2k_c^2 - n^2)R = 0. \tag{2.35}$$

This latter is known as Bessel's differential equation, with a solution taking the form

$$R(\rho) = CJ_n(k_c\rho) + DY_n(k_c\rho), \tag{2.36}$$

where $J_n(x)$ and $Y_n(x)$ are the Bessel functions of first and second kind, respectively. For a circular waveguide problem, the term $Y_n(k_c\rho)$ is not physically acceptable since it becomes infinite at $\rho = 0$. We can then reduce the solution to h_z to

$$h_z(\rho,\phi) = (A\sin n\phi + B\cos n\phi)J_n(k_c\rho). \tag{2.37}$$

The cut-off wavenumber can be determined by setting the boundary condition $E_{tangent} = 0$ on the guide wall. Since $E_z = 0$, it must be

$$E_\phi(\rho,\phi) = 0, \quad \text{at}\rho = a. \tag{2.38}$$

From (2.32b) we find E_ϕ as

$$E_\phi(\rho,\phi,z) = \frac{j\omega\mu}{k_c}(A\sin n\phi + B\cos n\phi)J_n'(k_c\rho)e^{-j\beta z}, \tag{2.39}$$

where $J_n'(k_c\rho)$ is the derivative of the Bessel function of first kind with respect to its argument. For (2.38) to be verified, it must be

$$J_n'(k_c a) = 0. \tag{2.40}$$

Defining p'_{nm} as the mth root of $J_n'(k_c\rho)$ as , so that $J_n'(p'_{nm}) = 0$, then k_c must be

$$k_{c_{nm}} = \frac{p'_{nm}}{a} \tag{2.41}$$

The values of p'_{nm} for the first three TE modes for $n = 0, 1, 2$ are given in Table 2.1.
The TE_{nm} modes are thus defined by the cut-off wavenumber $k_{c_{nm}} = p'_{nm}/a$, where n refers to the number of circumferential (ϕ) variations, and m refers to the number of radial (ρ) variations.

n	p'_{n1}	p'_{n2}	p'_{n3}
0	3.832	7.016	10.174
1	1.841	5.331	8.536
2	3.054	6.706	9.970

Table 2.1: Values of p'_{nm} for TE Modes in a circular waveguide

The propagation constant of the TE_{nm} mode is

$$\beta_{nm} = \sqrt{k^2 - k_c^2} = \sqrt{k^2 - (\frac{p'_{nm}}{a})^2}, \tag{2.42}$$

with a cut-off frequency of

$$f_{c_{nm}} = \frac{k_c}{2\pi\sqrt{\mu\epsilon}} = \frac{p'_{nm}}{2\pi a\sqrt{\mu\epsilon}}. \tag{2.43}$$

The first TE mode to propagate is the one with the smallest p'_{nm}, which is the TE_{11} mode in a circular waveguide (as can be seen in Table 2.1). This mode, also referred to as the dominant circular waveguide mode, is the most frequently used and it is one of the modes of interest in this work, as it will be shown in Chapter 3.
It can be noticed that, since $m \geq 1$, there is no TE_{10} mode.
The transverse field components for TE modes in a circular waveguide can be found as from (2.39) and are summarized in Table 2.3.
The wave impedance is then obtained from the transverse field components as

$$Z_{TE} = \frac{E_\rho}{H_\phi} = \frac{-E_\phi}{H_\rho} = \frac{\eta k}{\beta}. \tag{2.44}$$

TM Modes For the TM modes of a circular waveguide we must solve for E_z the wave equation expressed in cylindrical coordinates. Similarly to the TE case, we obtain

$$(\frac{\partial^2}{\partial\rho^2} + \frac{1}{\rho}\frac{\partial}{\partial\rho} + \frac{1}{\rho^2}\frac{\partial^2}{\partial\phi^2} + k_c^2)e_z(\rho,\phi) = 0, \tag{2.45}$$

where $E_z(\rho,\phi,z) = e_z(\rho,\phi)e^{-j\beta z}$. The general solutions for this equations are the same as for (2.34). After 2.37, we have

$$e_z(\rho,\phi) = (A\sin n\phi + B\cos n\phi)J_n(k_c\rho). \tag{2.46}$$

Differently from the TE solution, in this case the boundary conditions can be directly applied to e_z, since

$$E_z(\rho,\phi) = 0, \quad \text{at}\rho = a. \tag{2.47}$$

Then, we must have

$$J_n(k_c a) = 0, \quad k_c = \frac{p_{nm}}{a}, \tag{2.48}$$

where p_{nm} is the mth root of $J_n(x)$, so that $J_n(p_{nm}) = 0$. The values of p'_{nm} for the first three TM modes for $n = 0, 1, 2$ are given in Table 2.2.

n	p_{n1}	p_{n2}	p_{n3}
0	2.405	5.520	8.654
1	3.832	7.016	10.174
2	5.135	8.417	11.620

Table 2.2: Values of p_{nm} for TM Modes in a circular waveguide

The propagation constant of the TM_{nm} mode is

$$\beta_{nm} = \sqrt{k^2 - k_c^2} = \sqrt{k^2 - (\frac{p_{nm}}{a})^2}, \tag{2.49}$$

with a cut-off frequency of

$$f_{c_{nm}} = \frac{k_c}{2\pi\sqrt{\mu\epsilon}} = \frac{p_{nm}}{2\pi a\sqrt{\mu\epsilon}}. \tag{2.50}$$

Thus the first TM mode to propagate is the TM_{01} mode, with $p_{01} = 2.405$. It is greater than $p'_{11} = 1.841$ of the lowest order TE_{11} mode, so that the TE_{11} mode is the dominant mode of a circular waveguide. The transverse field components for TM modes in a circular waveguide can be found as from (2.39) and are summarized in table 2.3.
The wave impedance is then obtained from the transverse field components as

$$Z_{TM} = \frac{E_\rho}{H_\phi} = \frac{-E_\phi}{H_\rho} = \frac{\eta\beta}{k}. \tag{2.51}$$

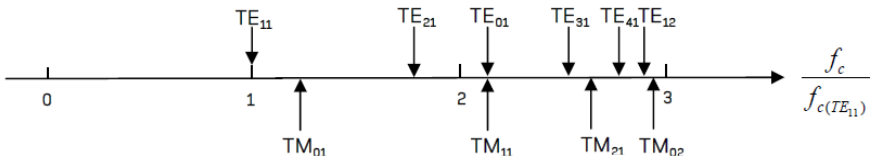

Figure 2.17: Cut-off frequencies of the first TE and TM modes of a circular waveguide [41].

Fig. 2.17 shows the cut-off frequencies of the first TE and TM modes. Field lines for some of the lower-order modes in a circular waveguide are depicted in Fig. 2.18.

Quantity	TE_{nm} **Mode**	TM_{nm} **Mode**
k	$\omega\sqrt{\mu\epsilon}$	$\omega\sqrt{\mu\epsilon}$
k_c	$\frac{p'_{nm}}{a}$	$\frac{p_{nm}}{a}$
β	$\sqrt{k^2-k_c^2}$	$\sqrt{k^2-k_c^2}$
λ_c	$\frac{2\pi}{k_c}$	$\frac{2\pi}{k_c}$
λ_g	$\frac{2\pi}{\beta}$	$\frac{2\pi}{\beta}$
v_p	$\frac{\omega}{\beta}$	$\frac{\omega}{\beta}$
α_d	$\frac{k^2\tan\delta}{2\beta}$	$\frac{k^2\tan\delta}{2\beta}$
E_z	0	$(A\sin n\phi + B\cos n\phi)J_n(k_c\rho)e^{-j\beta z}$
H_z	$(A\sin n\phi + B\cos n\phi)J_n(k_c\rho)e^{-j\beta z}$	0
E_ρ	$\frac{-j\omega\mu n}{k_c^2\rho}(A\cos n\phi - B\sin n\phi)J_n(k_c\rho)e^{-j\beta z}$	$\frac{-j\beta}{k_c}(A\sin n\phi + B\cos n\phi)J'_n(k_c\rho)e^{-j\beta z}$
E_ϕ	$\frac{j\omega\mu}{k_c}(A\sin n\phi + B\cos n\phi)J'_n(k_c\rho)e^{-j\beta z}$	$\frac{-j\beta n}{k_c^2\rho}(A\cos n\phi - B\sin n\phi)J_n(k_c\rho)e^{-j\beta z}$
H_ρ	$\frac{-j\beta}{k_c}(A\sin n\phi + B\cos n\phi)J'_n(k_c\rho)e^{-j\beta z}$	$\frac{j\omega\epsilon n}{k_c^2\rho}(A\cos n\phi - B\sin n\phi)J_n(k_c\rho)e^{-j\beta z}$
H_ϕ	$\frac{-j\beta n}{k_c^2\rho}(A\cos n\phi - B\sin n\phi)J_n(k_c\rho)e^{-j\beta z}$	$\frac{-j\omega\epsilon}{k_c}(A\sin n\phi + B\cos n\phi)J'_n(k_c\rho)e^{-j\beta z}$
Z	$Z_{TE}=\frac{\eta k}{\beta}$	$Z_{TM}=\frac{\eta\beta}{k}$

Table 2.3: Summarized Results for a Circular Waveguide.

2.7.2.4 Coaxial Lines

The coaxial line geometry is shown in Fig. 2.19, where the inner conductor of radius a is at a potential of V_o volts, while the outer conductor of radius b is at zero volts. The space between the two conductors is filled with a dielectric material. The fields can be derived from

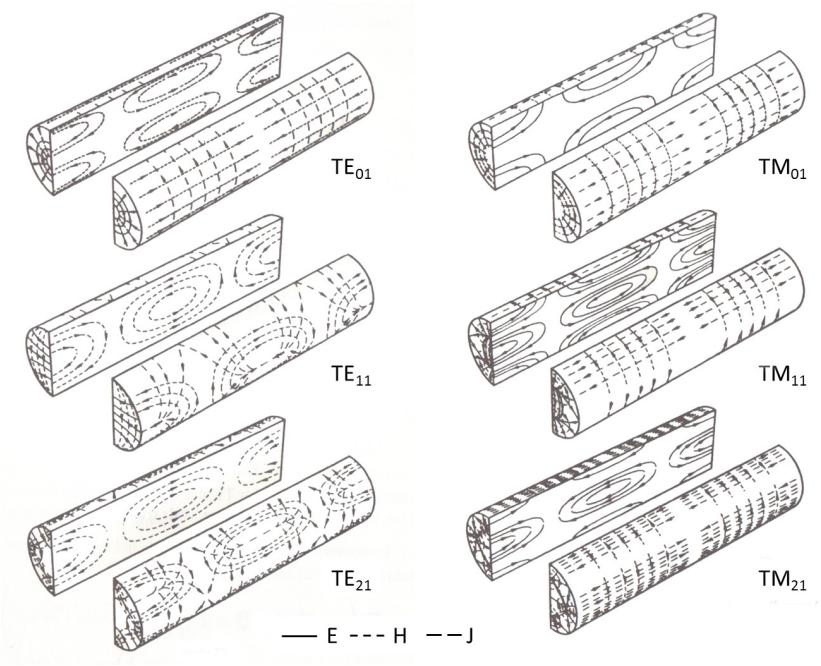

Figure 2.18: Field lines for some of the lower-order modes in a circular waveguide [42].

the scalar potential $\Phi(\rho, \phi)$ which is a solution of the Laplace's equation [41].

$$\frac{1}{\rho}\frac{\partial}{\partial\rho}(\rho\frac{\partial\Phi(\rho,\phi)}{\partial\rho}) + \frac{1}{\rho^2}\frac{\partial^2\Phi(\rho,\phi)}{\partial\phi^2} = 0, \tag{2.52}$$

and solve for $\Phi(\rho, \phi)$ under the boundary conditions

$$\Phi(a,\phi) = V_o, \tag{2.53a}$$
$$\Phi(b,\phi) = 0. \tag{2.53b}$$

Using the separation of variables, the final solution for $\Phi(\rho, \phi)$ can be written as

$$\Phi(\rho,\phi) = \frac{V_o \ln b/\rho}{\ln b/a} \tag{2.54}$$

The transverse fields can be found as

$$\bar{e}(\rho,\phi) = -\nabla_t(\rho,\phi) = -(\hat{\rho}\frac{\partial\Phi}{\partial\rho} + \frac{\hat{\phi}}{\rho}\frac{\partial\Phi}{\partial\phi}) = \frac{V_o\hat{\rho}}{\rho\ln b/a}, \tag{2.55a}$$
$$\bar{h}(\rho,\phi) = \frac{1}{\eta}\hat{z}\times\bar{e}(\rho,\phi) = \frac{V_o\hat{\phi}}{\eta\rho\ln b/a}. \tag{2.55b}$$

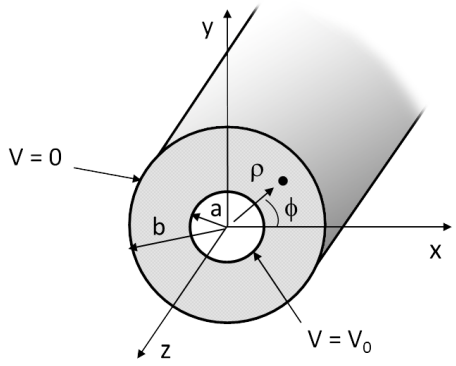

Figure 2.19: Coaxial line geometry.

Then, the total fields including the propagation factor are

$$\bar{E}(\rho,\phi,z) = \bar{e}(\rho,\phi)e^{-j\beta z} = \frac{V_o\hat{\rho}e^{-j\beta z}}{\rho\ln b/a}, \tag{2.56a}$$

$$\bar{H}(\rho,\phi) = \bar{h}(\rho,\phi)e^{-j\beta z} = \frac{V_o\hat{\phi}e^{-j\beta z}}{\eta\rho\ln b/a}. \tag{2.56b}$$

The total current on the inner conductor can be calculated as

$$I_a = \frac{2\pi V_o e^{-j\beta z}}{\eta\ln b/a}, \tag{2.57}$$

so that the characteristic impedance can be calculated as

$$Z_0 = \frac{V_o}{I_a} = \frac{\eta\ln b/a}{2\pi}. \tag{2.58}$$

Higher Order Modes The TEM propagation mode is the dominant one and has zero cut-off frequency. However, TE and TM waveguide modes also exist in coaxial lines. In practice these modes are usually cut-off (evanescent), having only a reactive effect at discontinuities or sources, where they are excited. However, it is important to calculate the cut-off frequency of the lowest-order waveguide modes, in order to avoid their propagation, causing unwanted effects due to the superposition of modes with different propagation constants.
For instance, the lowest-order waveguide mode is the TE_{11} mode, or the dominant waveguide mode of the coaxial line, with a cut-off wavelength that can be approximated to [43]

$$\lambda_c \simeq \pi(a+b) \tag{2.59}$$

2.7.2.5 Attenuation in Waveguides and Transmission Lines

The attenuation of propagating waves in transmission lines and waveguides is caused either by dielectric loss, with attenuation constant α_d or conductor loss, with attenuation constant α_c. The total attenuation constant can then be written as

$$\alpha = \alpha_d + \alpha_c. \tag{2.60}$$

The attenuation due to conductor loss depends on the field distribution inside the the guide, so that it must evaluated for each type of guiding structure. The TE_{nm} attenuation constant due to finite conductivity of the guide walls is

$$\alpha_{c_{TE}} = \frac{R_s}{\zeta a}[\frac{n^2}{(p'_{nm})^2 - n^2} + (\frac{\lambda}{\lambda_c})^2]\frac{1}{\sqrt{1-(\frac{\lambda}{\lambda_c})^2}} \tag{2.61}$$

where $\zeta = \sqrt{\frac{\mu}{\epsilon}}$ is the intrinsic impedance of the material filling the waveguide, and R_s is the frequency-dependent characteristic impedance of the metal walls, defined as

$$R_s = \sqrt{\frac{\omega\mu}{2\sigma}}, \tag{2.62}$$

where σ is the conductivity of the material.
With the same approach, the TM_{nm} attenuation constant can be defined as

$$\alpha_{c_{TM}} = \frac{R_s}{\zeta a}\frac{1}{\sqrt{1-(\frac{\lambda}{\lambda_c})^2}} \tag{2.63}$$

where the frequency-dependent characteristic resistance of the metal walls R_s is defined as in (2.62).
Finally, for coaxial lines, the attenuation of the dominant TEM mode due to dissipation in the inner and outer conductors is

$$\alpha_{c_{TEM}} = (\frac{R_a}{a} + \frac{R_b}{b})\frac{1}{2\zeta \ln\frac{b}{a}} \tag{2.64}$$

where R_a and R_b are the characteristic resistances of the metals of which the outer and inner conductors are constituted. For fixed outer radius and wavelength, the attenuation constant is a minimum when $a/b = 3.6$, provided $R_a = R_b$ [44].

The attenuation due to dielectric loss can be calculated from the propagation constant, and the result applies to any guide completely filled with a homogeneous dielectric.
In the case of $\tan\delta << 1$, which is applicable to most dielectric materials, the complex

propagation constant can be approximated to

$$\gamma = \alpha_d + j\beta = \frac{k^2 \tan\delta}{2\beta} + j\beta, \tag{2.65}$$

where $j\beta = \sqrt{k_c^2 - k^2}$ and $k^2 = \omega^2 \mu_0 \epsilon_0 \epsilon_r$ is the wavenumber in the absence of loss. (2.65) means that for small loss the phase constant $j\beta$ remains unchanged, while the attenuation constant due to dielectric loss is given by

$$\alpha_d = \frac{k^2 \tan\delta}{2\beta} \text{ Np/m} \quad \text{(valid for TE or TM waves)}. \tag{2.66}$$

This result can also be applied to TEM lines, where $k_c = 0$, with $\beta = k$:

$$\alpha_d = \frac{k \tan\delta}{2} \text{ Np/m} \quad \text{(valid for TEM waves)}. \tag{2.67}$$

2.7.2.6 Circular Open-ended Waveguide Resonator

One of the probe solutions proposed in this work, which is presented in detail in Chapter 3 (Section 3.5), is based on a circular open-ended waveguide resonator filled with low permittivity dielectric and ended with a ceramic protective cap.
The usefulness of open ended waveguides for displacement, small distances and non-destructive permittivity measurements has been pointed out by several authors [45, 46].
For this purpose, it is required to have a detailed knowledge of the fields within the probe and in the near vicinities of its aperture, as well as the relation of these fields with the reflection coefficient observed at the probe terminal, which has been investigated for simple cases in [47, 48].
In the following, we will focus on the description of the EM coupling phenomena occurring at the sensor discontinuities, in order to better understand the possible trends in the sensor response.
In order to model the scenario of the application, let us refer to Fig. 2.20(a), showing a longitudinal cut view of the circular waveguide resonator mounted into the case of the turbine, and oriented towards the moving blades.

A generalized transmission line equivalent model such as that shown in Fig. 2.20(b) can be applied to the modal analysis of the EM interactions between the feeding transmission line (#1 in the figure), the coupling probe #2, the waveguide segment #3, the dielectric cap #4 and the sensor aperture #5 coupling into the turbine region #6.
The proposed model relies on the principles that

- the interactions among the modes supported by the different sections of homogeneous transmission lines (#1, #3 and #4) are confined to the discontinuities interconnecting such sections (#2, #5 and #6),
- the propagation (or attenuation) of propagating (or evanescent) modes along these sec-

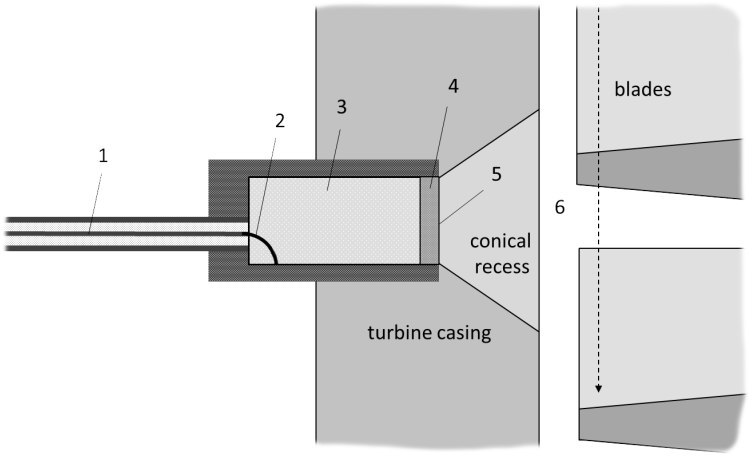

(a)

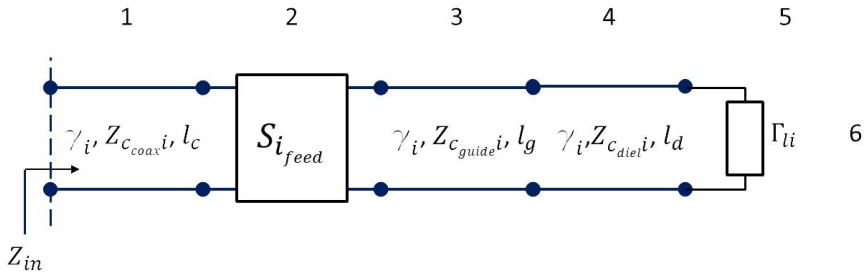

(b)

Figure 2.20: Cut view of the circular waveguide resonator mounted into the case of the turbine (a), and equivalent transmission line model (b).

tions can be modeled as through a stock of independent transmission lines (1 line per mode). These transmission lines access the multi-port network defined by the aforementioned discontinuities. This is illustrated in Fig. 2.20(b) for the i-esim mode.

The advantage of the proposed model is that for most of the "classical" transmission lines (i.e. coaxial and hollow circular, cylindrical or rectangular waveguides), the need to resort to more involved EM modeling techniques (such as the Finite Differences, Finite Elements, Mode-Matching [49–51] or the Integral Equations-Method of Moments [52, 53]) is limited to the analysis of the discontinuities, while the study of the remaining probe structure can be addressed by means of more intuitive transmission line models.
Among the different discontinuities depicted in Fig. 2.20(a), the one associated to the dielectric cap #4 can be straightforwardly incorporated into our transmission line model by properly adjusting the propagation constant along this short section of line to account for $\varepsilon_{r_{cap}}$. The rigorous modeling of the other transitions requires, however, to take into account the excitation of higher order modes and it is at this point that we shall apply dedicated EM modeling techniques such as the ones proposed above.
The transmission line parameters for the different sections of waveguide and modes can be derived from the following expressions, following the notation proposed in [52]. For each of the modes considered, Z_{ci} is the i-th modal characteristic impedance

$$Z_{ci} = Y_{ci}^{-1} = \begin{cases} \frac{j\omega\mu}{\gamma_i} & \text{TE modes} \\ \\ \frac{\gamma_i}{j\omega\varepsilon} & \text{TM modes} \end{cases} \tag{2.68}$$

with the modal propagation constants γ_i equal to

$$\gamma_{ci} = \begin{cases} j\beta_i = jk_{ci}\sqrt{1 - \left(\frac{\lambda}{\lambda_{ci}}\right)^2} & \lambda < \lambda_{ci} \\ \\ \alpha_i = k_{ci}\sqrt{1 - \left(\frac{\lambda_{ci}}{\lambda}\right)^2} & \lambda > \lambda_{ci} \end{cases} \tag{2.69}$$

where λ_{ci} is the i-th mode cut-off wavelength, and $k_{ci} = 2\pi/\lambda_{ci}$ is the i-th mode cut-off wavenumber [52].
With regard to the transitions #1 and #5, a convenient analysis approach proposed in [53] could be to apply the equivalence principle by

- replacing the discontinuities (i.e. circular and ring apertures, coaxial probe and blade scatterers) by a set of auxiliary equivalent sources (magnetic currents for the apertures and electric currents for the metallic scatterers) that satisfy the boundary conditions in such discontinuities (see Fig. 2.21(a) and 2.21(b)) and
- evaluating the interaction between these sources and all the modes that the waveguide can support to finally derive the modal scattering parameters of the multi-port networks that model these discontinuities.

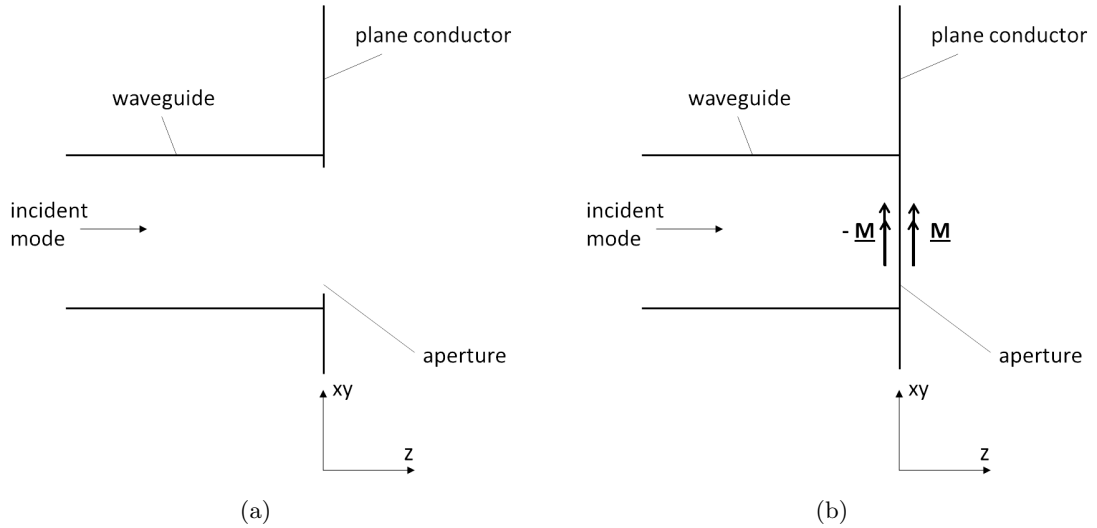

Figure 2.21: Magnetic currents at the aperture plane (a), and equivalent short circuit with auxiliary sources (b).

For the simple case of the aperture #5, the waveguide is short-circuited and the aperture is replaced by auxiliary surface magnetic currents. In order to model these currents we can consider a single vectorial function $\underline{M}$, that is defined in the domain of the aperture and that interacts with the dominant mode in the waveguide (TE_{11}) as well as with the other modes. The modal reflection coefficients that represent this interaction can be evaluated by projection of $\underline{M}$ over all the modes:

$$\iint_{guide} \underline{\mathrm{M}} \cdot u_z \times e_i \, ds = \begin{cases} 1 + \Gamma_0 & i = 0 \\ \Gamma_i & i \neq 0, \end{cases} \tag{2.70}$$

where Γ_0 is the reflection coefficient as seen by the incident mode, while Γ_i is the reflection coefficient of the remaining scattered modes. The auxiliary magnetic currents can be calculated by the Integral Equations-Method of Moments (IE-MoM) [52].
The analysis of the discontinuity between the feeding transmission line (#1) and the circular waveguide (#3) combines the interaction between two waveguide apertures and a metallic scatterer. We can then define a set of auxiliary electric and magnetic currents that interact with the modes supported by the coaxial and the circular waveguide by projection. For each mode i considered, we obtain a scattering matrix S_i, as shown in Fig. 2.20(b). An alternative analysis approach for this transition is proposed in [54].

Considerations In the previous section, we identified at least three discontinuities that that could possibly affect the measured signal with uncertainties. In particular the discontinuities at the feeding probe/loop #2 and at the probe aperture #6 are sources of high order modes

propagation, while the discontinuity at the dielectric cap #4 will just introduce a impedance step that we can easily incorporate in our transmission line model.
In general, the input impedance Z_{in} seen by the incident mode at the termination of the coaxial feeding line will depend on the loading of the probe aperture (Fig. 2.20(b)) and the scattering parameters (S_o) of the feeding probe/loop, which incorporate the contribution of the other scattered modes that are not "seen" by the measuring instrument. these modes contribute anyway to the impedance matching, by exchanging power with the dominant mode at the discontinuities.
The probe circular waveguide should be dimensioned (in terms of radius and length) such that only the dominant mode TE_{11} is propagating and the higher modes excited at a given discontinuity decay before interacting with the following one. In the case depicted in Fig. 2.20(b), the modes excited at the feeding probe/loop might interact with those excited at the aperture and viceversa.
In order to give a quantitative example, the Γ_is of the probe aperture were evaluated using an IE-MoM technique based on [52], and the scattered modes were calculated in the vicinities of the probe-loop. Results show that the level of the scattered high-order modes, among which the TM_{01} has the most important contribution, is attenuated by more than 80 dB within the frequency band of operation of the probe (24-25 GHz).

2.7.2.7 Open-ended Coaxial Resonator

Similar considerations done in Section 2.7.2.6 are applicable to the case of the open-ended coaxial probe depicted in Fig. 2.22(a), with the corresponding equivalent TL model of Fig. 2.22(b).
In the case of TEM modes, the modal characteristic impedance Z_{ci} is

$$Z_{ci} = Y_{ci}^{-1} = \sqrt{\frac{\mu}{\varepsilon}} = \eta \tag{2.71}$$

and the modal propagation constant

$$\gamma_{ci} = j\omega\sqrt{\mu\varepsilon} = \eta. \tag{2.72}$$

Feeding Methods An electromagnetic field can exist inside a cavity when an electromagnetic signal is injected by an outside circuit. The elements for the excitation of the field may be simple apertures in the cavity wall, capacitive probes, inductive loops or electron beams. Here we will treat only those feeding methods which are relevant for the solutions investigated in Chapter 3, i.e. the inductive loop and the capacitive probe. A wider overview on excitation of waveguides and cavities can be found in [55].

Inductive loop When a cavity is coupled to a transmission line (generally a coaxial line), an inductive loop is most often utilized (shown in Fig. 2.23(a). The center conductor of the feeding coaxial cable is extended into the cavity and grounded to the wall of the resonator,

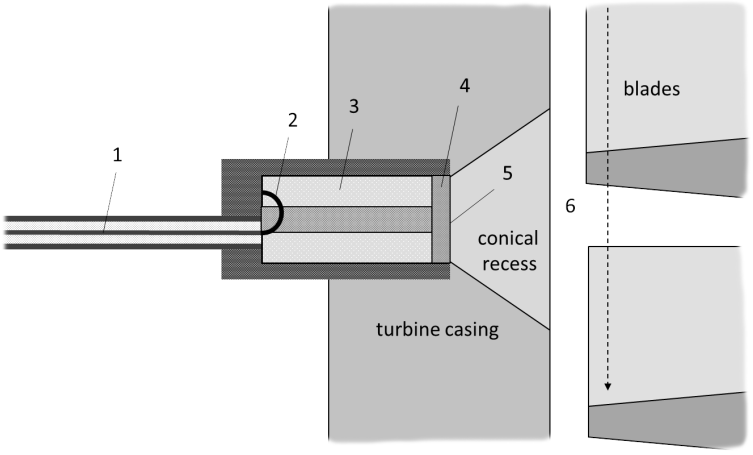

(a)

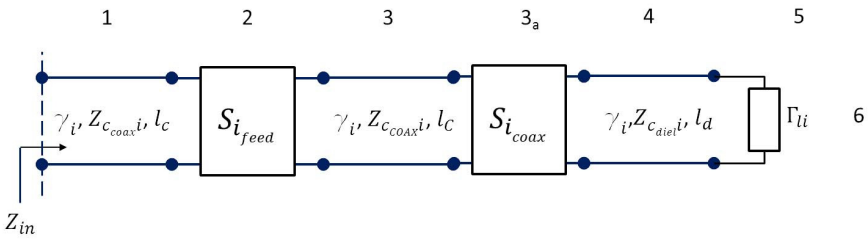

(b)

Figure 2.22: Cut view of the circular coaxial resonator mounted into the case of the turbine (a), and equivalent transmission line model (b).

the size of the loop being much smaller than the wavelength.
A current flows around the loop of conductor, generating a magnetic field perpendicular to the plane of the loop. The coupling loop excites the modes which have a magnetic field lines crossing the plane of the loop, as:

$$\int_S \underline{H}_r \cdot n \mathrm{d}A \neq 0 \qquad \text{A·m} \tag{2.73}$$

where $\underline{H}_r$ is the field of the cavity mode considered (Fig. 2.23(a)). The excitation can be optimized by placing the loop where the integral has its largest value. On the other hand, the fact that modes for which the integral vanishes are not excited can be conveniently used to position the loop so that only particular cavity modes are excited.

Capacitive probe Another coupling element convenient in the case of cavity feeding by means of coaxial lines, is the capacitive probe(shown in Fig. 2.23(b)). The inner conductor of the feeding coaxial cable is extended into the resonator and terminated into an open line, its length being short compared to the wavelength. The current flowing in the probe creates an electric field between the probe and the adjacent wall of the resonator, radiating energy into the cavity like a small monopole antenna.
The capacitive probe couples only to resonance modes that have a electric field lines parallel to it (Fig. 2.23(b)). The coupling is largest when the probe is located at a maximum of the electric field of the excited mode, while modes having zeroes of the tangential electric field at this location are not excited.
By choosing the probe/loop length and position correctly, the input impedance can be made equal to the characteristic impedance Z_c of the input coaxial line over a fairly broad range of impedances.
The basic problems of radiation from a probe antenna and a small loop antenna in waveguides are further discussed further in [55, Ch. 7].
Both the above-mentioned feeding methods can be used to probe the TE_{11} circular waveguide-based resonators and TEM circular coaxial resonators that are considered in this work, as in will be shown in Chapter 3 (Section 3.5 and 3.6).

2.7.3 A Comparison of the Investigated Solutions

Among the different possibilities for implementing the blade tip monitoring probe architecture, the antenna-based solutions suggested by the radar-like sensing system may seem, in principle, very promising candidates. However, the solutions based on antennas, which are mainly meant to interact with relatively distant targets (or sources), present large propagating fields, while the near field characteristics play (with the exception of impedance matching) a secondary role. Such a role is often considered either detrimental to the antenna performance (as it is the case of coupling phenomena with neighboring antennas and supporting structures, for example) or may provide some convenient tuning opportunities in terms of matching and miniaturization. It is therefore not surprising that in most practical antenna designs (such

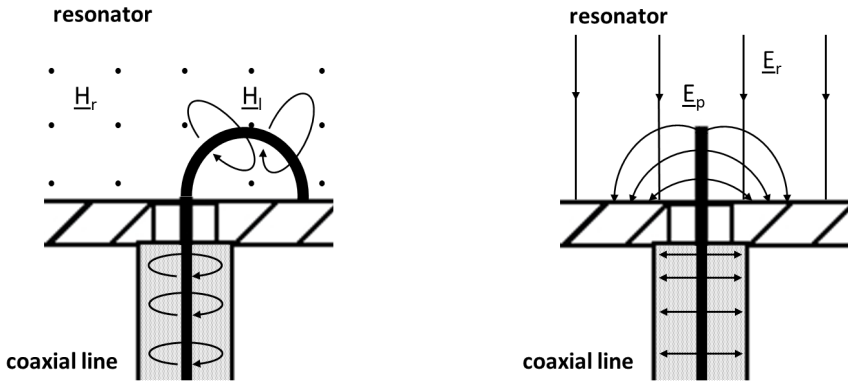

Figure 2.23: (a) The magnetic field ($\underline{H}_l$) of a coupling loop couples to the resonance mode through the magnetic field ($\underline{H}_r$) perpendicular to the plane of the loop, (b) the electric field ($\underline{E}_p$) of a coupling probe couples to the resonance mode through the electric field ($\underline{E}_r$) parallel to the probe.

as dipoles, helices and patches, for example) either the strength of the near fields tends to be very reduced, either the complexity of the field distribution increases with the antenna tuning capabilities.
These features are not desirable for a probe that is intended to operate in a small-range sensing system, under demanding thermal and mechanical constraints. In these conditions, the stability of the probe operation and the easy predictability of its near-field characteristics become decisive to guarantee reliable blade measurements.
Alternatively, resonator-based sensor architectures, as that illustrated in Fig. 2.20(a) and 2.22(a), are very sensitive to close perturbations (which can be attributed to very strong near fields) their geometries are relatively simple and they can be easily miniaturized. As a proof of simplicity, once the resonator radius that sets the cut-off frequency of the desired propagating mode has been determined, the resonant frequency is tuned by adjusting the resonator length. All these features are very well suited for the application considered in this work, since they

- are compatible with improved space resolution in very short ranges,
- ease the integration into small turbines, and
- provide enhanced operational stability within harsh environments.

Bibliography

[1] L. S. Langston, *Encyclopedia of Energy*, 2004, vol. 6, pp. 221–230.

[2] E. B. Holmquist and P. L. Jalbert, "Turbine blade tip clearance measurement instrumentation," in *Proc. ASME Turbo Expo 2007: Power of Land, Sea and Air*, Montreal, Canada May 14-17, 2007.

[3] M. W. Wiseman and T.-H. Guo, "An investigation of life extending control technoques for gas turbine engines," in *Proc. American Control Conference*, June 25-27, Arlington, VA 2001.

[4] D. Kwapisz, M. Hafner, V. Spitsyn, M. A., and V. Berezhnoy, "Test and validation of microwave tip clearance sensor on a 25 MW gas turbine engine," in *XVI International congress of propulsion engineering*, Rybachye, Ukraine 18 Sept. 2011.

[5] T. A. Holst, "Analysis of spatial filtering in phase-based microwave measurements of turbine blade tips," *M. Sc. thesis, Georgia Institute of Technology*, August, 2005.

[6] J. W. H. Chivers, "A technique for the measurement of blade tip clearances in a gas turbine," *Ph.D. Thesis, University of London, UK*, 1989.

[7] P. Tappert, A. von Flotow, and M. Mercadal, "Autonomous phm with blade-tip-sensors: algorithms and seeded fault experience," in *Aerospace Conference, 2001, IEEE Proceedings.*, vol. 7, 2001, pp. 3287–3295.

[8] D. P. Davidson, R. D. Derose, and A. J. Wennerstrom, "The mesurement of turbomachinery stator-to-drum running clearances," *ASME 83-GT-204*, 1983.

[9] A. G. Sheard and S. R. Turner, "An electromechanical measurement system for the study of blade tip-to-casing running clearances," *ASME 92-GT-50*, 1992.

[10] G. D. Bailleul and S. Albijat, "Review of progress in the development of capacitive sensors for blade tip clearance measurement," *ASME 96-TA-1*, 1996.

[11] D. Müller, A. D. Sheard, S. Mozumdar, and E. Johann, "Capacitive measurement of compressor and turbine blade tip to casing running clearance," *Journal of engineering for gas turbines and power*, vol. 119, no. 4, pp. 877–884, 1997.

[12] A. G. Sheard, "Blade by blade tip clearance measurement," *International Journal of Rotating Machinery*, vol. 2011, Article ID 516128, 13 pages, doi:10.1155/2011/516128, 2011.

[13] T. Fabian, K. Sangkyun, and F. Prinz, "Capacitive blade tip clearance measurements for a micro gas turbine," in *Proceedings of the 19th IEEE Instrumentation and Measurement Technology Conference, IMTC*, vol. 2, 2002, pp. 1011–1015.

[14] T. Fabian, F. B. Prinz, and G. Brasseur, "Capacitive sensor for active tip clearance control in a palm-sized gas turbine generator," *IEEE Transactions on Instrumentation and Measurement*, vol. 54, no. 3, pp. 1133–1143, June 2005.

[15] C. Roeseler, A. von Flotow, and P. Tappert, "Monitoring blade passage in turbomachinery through the engine case (no holes)," in *Aerospace Conference Proceedings, IEEE*, vol. 6, 2002, pp. 3125–3129.

[16] R. Jones and M. Hazell, "The in-situ measurement of aero-engine blade flap using an optical fibre sensor," in *IEE Colloquium on Advanced Vibration Measurements, Techniques and Instrumentation for the Early Prediction of Failure*, vol. 6, May 1992, pp. 1–5.

[17] T. Kawasima, H. Iinuma, and N. Minagawa, "Optical semiconductor blade vibration monitoring system for gas turbine engine," in *Instrumentation and Measurement Technology Conference, IMTC*, vol. 2, May 1994, pp. 601–604.

[18] H. S. Dhadwal and A. P. Kurkov, "Dual-laser probe tip clearance system for turbomachinery," *J. Turbomachinery*, vol. 121, no. 3, pp. 481–485, 1999.

[19] A. B. Vakhtin, S.-J. Chen, and S. M. Massick, "Optical probe for monitoring blade tip clearance," in *47th AIAA Aerospace Sciences Meeting Including The New Horizons Forum and Aerospace Exposition*, January 5-8, Orlando, FL, 2009.

[20] R. R. Grzybowski *et al.*, "Microwave recess distance and air path clearance sensor," *United States Patent No. 5,818,242*, Oct. 6, 1998.

[21] J. Wenger, M. Noweck, M. Stotz, D. Leistner, and G. Trummer, "An mmic-based microwave sensor for accurate clearance measurements in aircraft engines," *IEEE Transactions on Instrumentation and Measurement*, vol. 2, pp. 1122–1126, 1997.

[22] M. Wagner, A. Schulze, M. Vossiek, C. Stephelbauer, R. Weigel, N. Vortmeyer, and P. Heide, "Novel microwave vibration monitoring system for industrial power generating turbines," in *ARFTG Conference Digest-Spring, 51st*, vol. 33, June 1998, pp. 143–146.

[23] J. L. Geisheimer *et al.*, "Phase-based sensing system," *United States Patent No. 7,283,096*, December 3, 2002.

[24] M. R. Woike, J. W. Roeder, C. E. Hughes, and T. J. Bencic, "Testing of a microwave blade tip clearance sensor at the NASA Glenn research center," in *47th AIAA Aerospace Sciences Meeeting*, Orlando, Florida 5-8 January, 2009.

[25] D. Kwapisz, M. Hafner, and S. Queloz, "Calibration and characterization of a cw radar for blade tip clearance measurement," in *Proceedings of the 7th European Radar Conference (EuRAD)*, Sept. 30-Oct. 1 2010, pp. 320–323.

[26] A. Schicht, S. Schwarzer, and L.-P. Schmidt, "Tip clearance measurement technique for stationary gas turbines using an autofocusing millimeter-wave synthetic aperture radar," *IEEE Transactions on Instrumentation and Measurement*, no. 99, pp. 1–8, 2012.

[27] E. B. Holmquist, "Measuring rotor imbalance via blade clearance sensors," *United States Patent No. 7,775,107*, August 17, 2010.

[28] E. Nyfors, "Industrial microwave sensors - a review," *Subsurface Sensing Technologies and Applications*, vol. 1, no. 1, 2000.

[29] J. L. Geisheimer, S. A. Billington, D. Burgess, and G. Hopkins, "Microstrip patch antenna for high temperature environments," *United States Patent No. 7,283,096*, October 16, 2007.

[30] M. Violetti, J.-F. Zürcher, J. Geisheimer, and A. K. Skrivervik, "Design of antenna based sensors for blade tip clearance measurement in gas turbines," in *Proc. 4th European Conference on Antennas and Propagation*, 12-16 April, Barcelona, Spain 2010.

[31] M. Violetti, A. K. Skrivervik, Q. Xu, J. Geisheimer, and G. Egger, "Device and method for monitoring rotor blades of a turbine," *European Patent Application No. 11181622*, Sept. 16, 2011.

[32] J. D. Kraus, *Antennas*. McGraw-Hill, Inc., 1988.

[33] K. Hirasawa and M. Haneishi, *Analysis, Design and Measurement of Small and Low-Profile Antennas*. Artech House, 1992.

[34] L. Bancroft, *Microstrip and Printed Antenna Design*. Noble Publishing, 2004.

[35] G. Kumar and K. P. Ray, *Broadband Microstrip Antennas*. Artech House, 2003.

[36] J. Watkins, "Nondestructive measurement of complex permittivity for dielectric slabs," *Electronic Letters*, vol. 5, pp. 524–525, 1969.

[37] J.-F. Zürcher and F. E. Gardiol, "Nondestructive microwave measurements of materials' moisture in building walls," in *Proc. IMEKO Congress Int. Measurement Confederation, Moscow*, May 1979, pp. 393–398.

[38] J. R. James, P. S. Hall, and C. Wood, *Microstrip Antenna*. Peter Peregrinus, London, 1981.

[39] T. S. Laverghetta, *Microwave Materials and Fabrication Techniques (3rd edition)*. Artech House, 2000.

[40] M. C. Huynh and W. Stutzman, "Ground plane effects on planar inverted-f antenna (pifa) performance," *IEE Proc. Microw. Antennas Propag.*, vol. 150, No. 4, Aug. 2003.

[41] D. M. Pozar, *Microwave Engineering*. Addison-Wesley Publishing Company, Inc., 1990.

[42] F. E. Gardiol, *Introduction to Microwaves*. Artech Hose, Inc., 1984.

[43] S. Orfanidis, *Electromagnetic Waves and Antennas*. available at http://www.ece.rutgers.edu/ orfanidi/ewa/, 2008.

[44] N. Marcuvitz, *Waveguide Handbook*. McGraw Hill, New York, 1951.

[45] M. S. Ramachandraiah and F. E. Gardiol, "A noncontacting method for the measurement of small displacement and surface irregularities of conducting objects," *International Power Microwave Symposium*, pp. 48–57, May Ottawa, Canada, 1972.

[46] M. Decreton and M. Ramachandraiah, "Nondestructive measurement of complex permittivity for dielectric slabs," *IEEE Transactions on Microwave Theory and Techniques*, vol. 23, no. 12, pp. 1077–1080, Dec. 1975.

[47] L. Lewin, *Advanced theory of waveguides*. Iliffe and Sons, Ltd., 1951.

[48] J. Galejs, *Antennas in Inhomogeneous Media*. Pergamon Press, Ltd., 1969.

[49] P. Clarricoats and K. Slinn, "Numerical method for the solution of waveguide-discontinuity problems," *Electronics Letters*, vol. 2, no. 6, pp. 226 –228, Jun. 1966.

[50] A. Wexler, "Solution of waveguide discontinuities by modal analysis," *IEEE Transactions on Microwave Theory and Techniques*, vol. 15, no. 9, pp. 508 –517, Sept. 1967.

[51] J. A. Ruiz-Cruz, J. R. Montejo-Garai, and J. M. Rebollar, *Passive Microwave Components and Antennas*. Intech, 2010, ch. Computer Aided Design of Waveguide Devices by Mode-Matching Methods, pp. 118–140.

[52] R. F. Harrington and J. R. Mautz, "Electromagnetic coupling through apertures," Department of Electrical and Computer Engineering, Technical Report TR-81-4, Aug. 1981.

[53] ——, "Electromagnetic coupling through apertures by the generalized admittance approach," *Computer Physics Communications*, vol. 68, pp. 19–42, Nov. 1991.

[54] G. Gerini and M. Guglielmi, "Full-wave cad of a rectangular waveguide filter with integrated coaxial excitation," *IEEE Transactions on Microwave Theory and Techniques*, vol. 49, no. 5, pp. 986–989, May 2001.

[55] R. E. Collin, *Field Theory of Guided Waves*. 2nd ed., Wiley-Interscience, New York, 1991.

3 Microwave Solutions for Rotating Machinery Health Monitoring

3.1 Outline of the Chapter

In this chapter, we present a number of possible solutions for the front end of the microwave sensing system described in Section 2.6.
First, a 5.8 GHz patch antenna probe is described in section 3.3. This probe is an existing solution by MSS [1], suitable for blade sensing in large frame turbines. It was investigated to understand the origin of some unexpected resonances in the response of some of the measured prototypes at the temperature of ∼300°C. The probe served also as a reference to study the behavior of used materials toward a large temperature change and to propose improved solutions.
A smaller version of the patch antenna probe was previously attempted at MSS for operation at 24 GHz, but the radiating element became too small and the effect of the feeding cable too important to obtain acceptable performance.
The 24 GHz PIFA probe presented in Section 3.4 is the first proposed solution that was conceived for operation in small-sized turbines. The PIFA technology allowed to obtain a miniature device with promising performance. Room temperature prototypes were built and tested, with encouraging results. However, this solution showed significant sensitivity to temperature drift, mechanical tolerances and vibration and could not be validated for operation on real engines.
The 24 GHz waveguide resonator probe presented in Section 3.5 is one of the new resonator-based designs, proposed as a valid alternative to the more complex antenna-based designs, and intended for BTC measurement in small-size turbines. Tests performed allowed to optimize the probe for operation up to 900°C for extended time, demonstrating its robustness and suitability for blade detection in a range of 6 mm.
A further new proposed design consists of a coaxial resonator probe especially intended for BTT, operating at 5.8 GHz. This simple and robust solution allows to have excellent waveform quality in very compact dimensions. The radially symmetric TEM field configuration of the coaxial resonator is particularly suitable for blade tip measurement where radiation properties should not be sensitive to probe orientation. A smaller version of the coaxial probe was investigated for possible operation at 24 GHz, showing important sensitivity to mechanical tolerances due to its reduced size.

3.2 Microwave Probes Requirements

For the specific application considered, the probes are required to have a reflection coefficient with a a single resonance within a 5% band centered at the working frequency (6 GHz or 24 GHz, for the new probes). The resonance should be sharp and only weakly temperature dependent, with a maximum accepted drift of the resonant frequency of 700 MHz from room temperature (∼20°C) to 900°C. The phase should be as linear as possible throughout the entire signal chain (hardware, probe, blade/probe interactions).
From a mechanical standpoint, the probe must deliver stable performance towards engine vibrations for periods of operation of >20000 hours, in the presence of temperature variations of 400°C in 90 seconds for more than +2500 cycles.
The use of special high temperature and fully-dense ceramics and metal alloys in the manufacturing of the probe structure is envisaged to maintain hermeticity and robustness.
The probes should be compact to avoid interfering with the performance of the operating turbine engine, with targeted diameters of <12 mm.
Finally, the probes should be designed to be as little sensitive as possible to both the axial position relative to the blade (the axial position changes in response to the aerodynamic forces of the rotor acting on the rotor thrust bearing and thermal rotor dilatation) and mounting orientation (orientation dependence is an additional constraint during installation). It is also beneficial that any proposed sensor design would be simple to allow for mechanical stability and good repeatability of manufacturing and industrialization process.

3.3 Existing 5.8 GHz Patch Antenna Probe

The existing 5.8 GHz patch antenna probe [1] was initially studied in order to understand its performance and as a starting point in order to propose improved probe designs.
The patch probe under test consists of a circular alumina dielectric substrate (∼ 2.5 mm thick) with a conductive film (the circular patch radiator, (∼ 7.5 mm diameter)) deposited on it. The alumina dielectric used has a small variation in dielectric constant as a function of temperature, minimizing drift in the antenna center frequency as the temperature of the application environment changes. Such ability is confirmed by simulations (Section 3.3.2), in good agreement with the measurements on prototypes (Section 3.3.3).
The radiator is fed by a high temperature microwave coaxial cable.
A ceramic/metallic casing encloses the radiating element, for protection and mechanical robustness. The metallic probe body is used to mechanically retain the dielectric substrate as well as to provide the mechanical and electrical attachment between the microwave cable and the dielectric substrate.

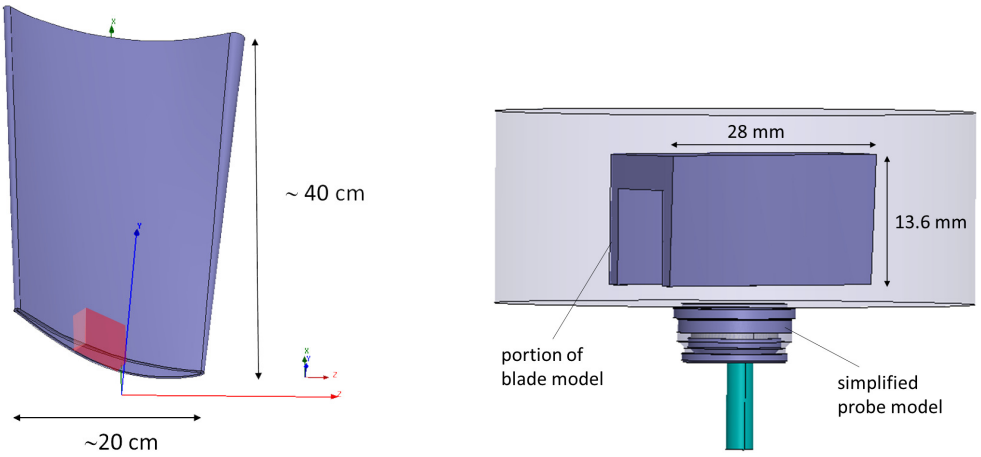

(a) (b)

Figure 3.1: 3D view of the simplified blade model (a). A smaller portion of the blade (marked in red) and a simplified probe model was used to ease software simulations (b).

3.3.1 Blade-Probe Interaction

In general, the sensor measurement capability greatly depends on the geometry of the object in front of the probe, i.e. the passing blade in the application considered here. For a fixed blade shape, the relative axial position of the probe with respect to the blade and its angular orientation can be tuned to improve performance. In fact, because of the polarization of the EM field generated by the probe, its angular orientation influences the measured data.
In order to investigate the influence of the blade presence on the probe response, a portion of a simplified pec blade model with the essential blade features (see Fig. 3.1) was used to simulate the effect of the passing blade on the EM field of the probe. The portion of the blade model was selected according to the realistic position of the probe, i.e. 26 mm axial shift with respect to the blade leading edge. The blade model was positioned at different distances from the probe tip aperture, for clearances of 0.5 to 8 mm (with a step of 0.5 mm), with a maximum axial shift of ± 10 mm from the probe center and for discrete orientation angles from 0° to 360° (with a step of 30°).

Fig. 3.2 shows the 0° position of the probe with respect to the blade, used as a reference in the performed studies.

Fig. 3.3 shows the blade-probe interaction as the blade model sweeps in front of the probe tip parallel to the 0° position line, at an average clearance of 2 mm. For simplicity, 3 positions of the axial shift are considered. As expected, reflection is maximum when the blade completely covers the probe tip aperture. The probe response toward mounting orientation angles for two different values of the blade-probe clearance are shown in Fig. 3.4(a) and 3.4(b). The corresponding electric field computed on the plane longitudinal to the blade is shown in Fig. 3.4(c) and 3.4(d). The nature of the blade-probe interaction is complex so that the probe is

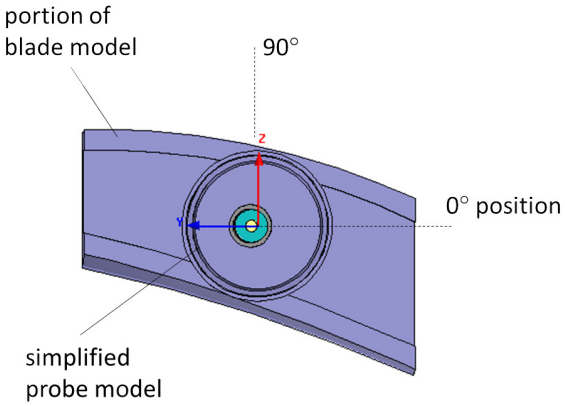

Figure 3.2: 0° position of the probe with respect to the blade.

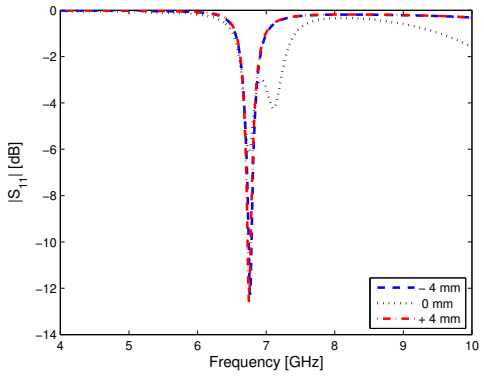

Figure 3.3: Reflection coefficient (magnitude) of the patch probe as the blade is translated parallel to the 0° position line, at -4 mm, 0 mm and +4 mm respect to the probe tip center at 2 mm-clearance.

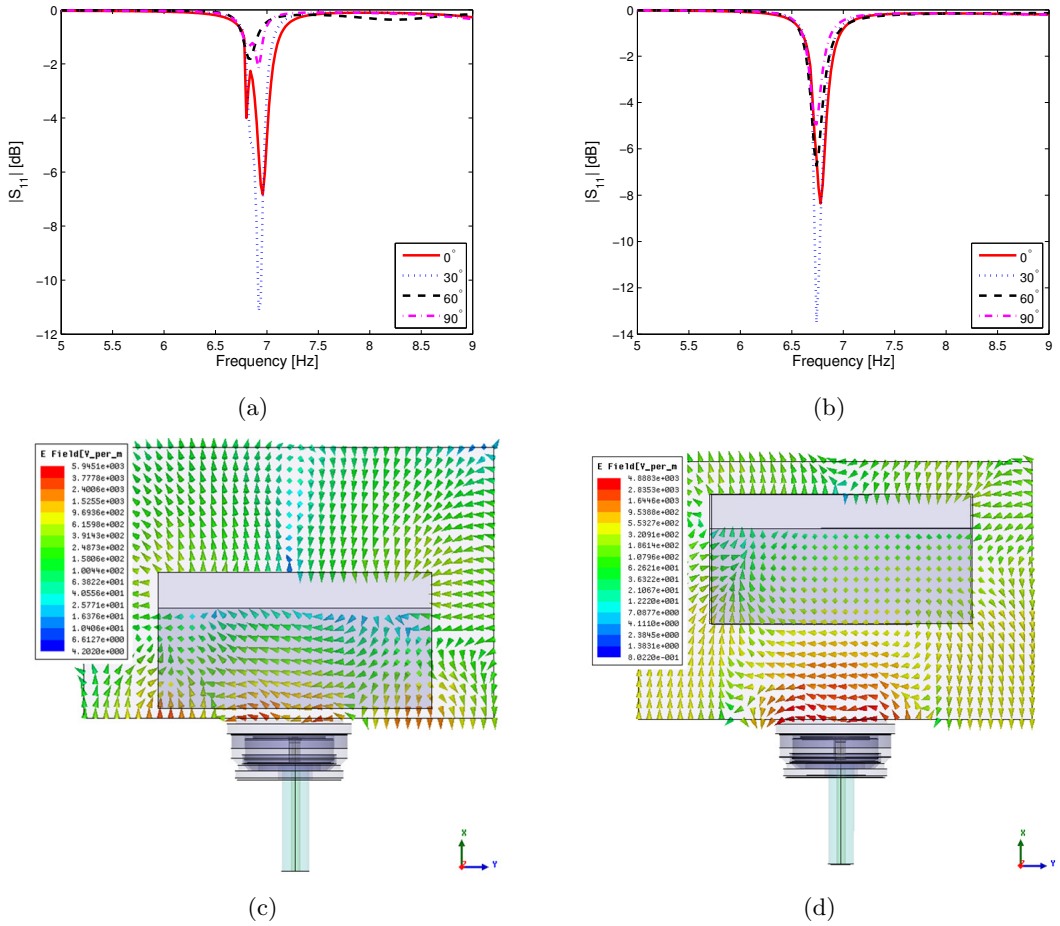

Figure 3.4: Reflection coefficient (magnitude) of the patch probe for the blade positioned above the probe tip center for different orientation angles at 0.5 mm-clearance (a) and at 8 mm-clearance (b). The electric field mapping is plotted on the plane longitudinal to the blade at 0.5 mm-clearance (c) and 8 mm-clearance (d).

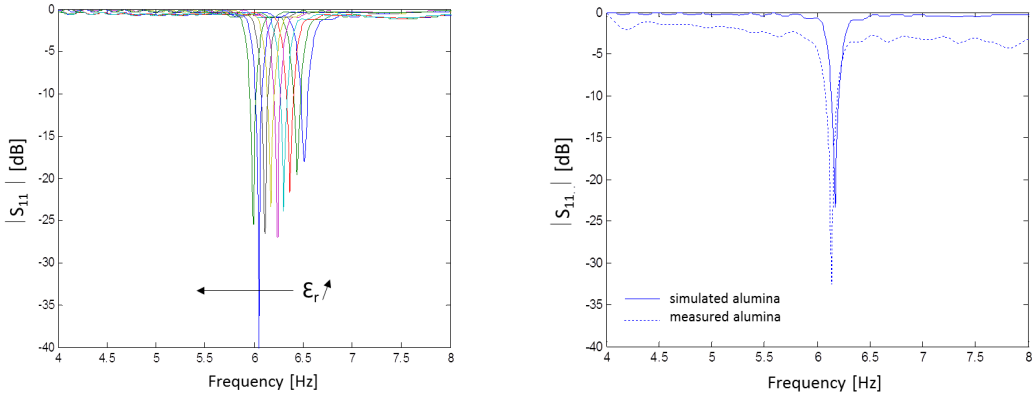

(a) (b)

Figure 3.5: (a) Simulated reflection coefficient vs. alumina permittivity variation, (b) simulated vs. measured resonance for one of the values of alumina ε_r.

typically fine-tuned during field tests, in order to have maximum consistency of measurements during engine operation.

3.3.2 Influence of Temperature on Materials

Parametric investigations were carried out to study the influence of temperature on materials: variations of alumina permittivity and loss tangent, coaxial dielectric powder permittivity, and conductivity of materials employed showed that the only parameter that has a significant influence on the resonance frequency is the alumina permittivity variation. In the study, alumina permittivity values considered range from 9 to 11 with a 0.25 step. As the permittivity increases, the resonance frequency shifts toward lower values, from 6.6 GHz to 5.95 GHz, as shown in Fig. 3.5(a).

3.3.3 Measurements on Prototypes

Thermal tests were carried out at EPFL and MSS in a range of temperature between 0°C and 800°C. The following three procedures were used to heat the probe:

- Cycle1, where the probe is baked at 800°C for 100 minutes. The heating rate is slowly increased from 80°C to 800°C, i.e. ∼12°C/minutes, so that the probe core temperature increases linearly,
- Cycle2, where the probe after assembly is baked at 800°C for 200 minutes. The heating rate is slowly increased from room temperature (∼20°C) to 800°C, i.e. ∼16°C/minutes,
- Burn-in, where the probe after assembly is baked at 800°C for 100 minutes. The heating rate is slowly increased from room temperature (∼20°C) to 800°C, i.e. ∼40°C/minutes.

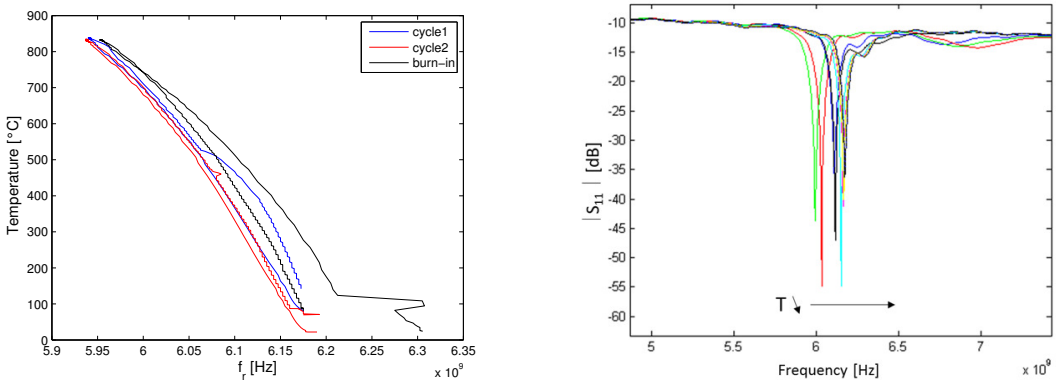

(a) (b)

Figure 3.6: (a) Resonance frequency f_r vs. temperature, (b) $|S_{11}|$ vs. temperature.

A good agreement was found between results from the measurement sessions, so that it was possible to establish a general trend for the behavior of the resonance frequency toward temperature. Figure 3.6(a) shows a shift of the resonance frequency f_r from 5.95 GHz at 800°C to ∼6.17 GHz at room temperature. The matching of the reflection coefficient is unaffected by the temperature change, as shown in Fig. 3.6(b).

In order to confirm the simulated results of the alumina permittivity variation toward temperature (see Section 3.3.2), measurements were carried out using alumina samples with different ε_r. The best agreement between simulations and measurements was found for one of the values of ε_r (see Fig. 3.5(b)), while for the other values considered the simulated resonance is higher than the measured one.

3.3.4 Remarks

Due to the vicinity of the radiating element to the turbine hot section, the probe is very sensitive to temperature.

In fact, this design can only withstand a temperature of about 800°C for a short period of time without any air cooling, as demonstrated during burn-in probe tests carried out at MSS.

A room temperature prototype of the patch antenna was scaled to operate at 24 GHz. The radiating element was miniaturized to such a small size that the feeding cable diameter became too important to have a good matching. This patch antenna has never been further tested on blade test-bed nor upgraded to high temperature version.

Moreover, the mechanical complexity of the patch probe body does not allow for robustness versus permittivity and size variation due to the large temperature change.

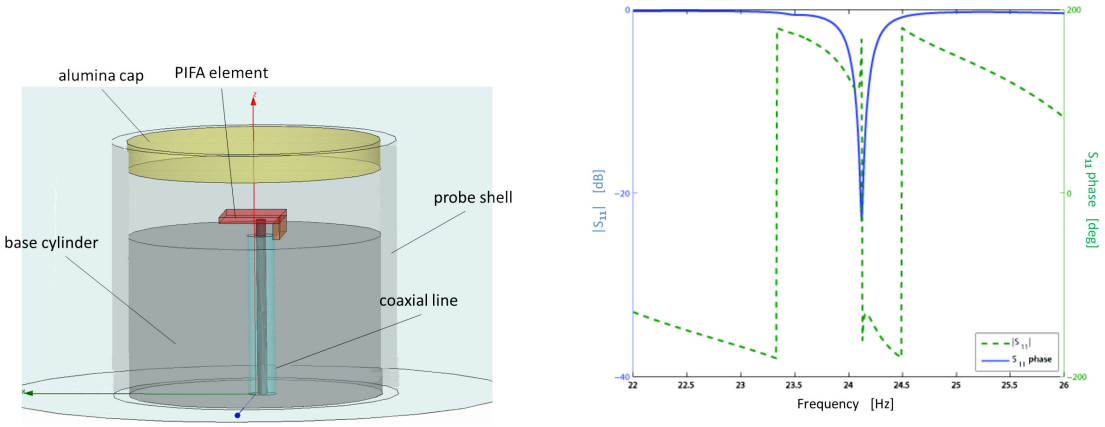

(a) (b)

Figure 3.7: 3D view of first PIFA probe model used in software simulations (a). Obtained results with the first model after optimization (b).

3.4 24 GHz PIFA Probe

The new proposed antenna-based solution for BTC measurement is a 24 GHz PIFA probe [2], which consists of a PIFA element on a metallic ground plane, fed by a high temperature coaxial cable and protected by an alumina lid. The outer diameter of the probe is 9 mm.
The PIFA technology allows maintaining the probe dimensions compact without the use of a thick dielectric substrate (except for the protective radome), reducing the complexity of the existing patch probe design.
The probe concept was studied and optimized through simulation with the finite element method solver ANSYS HFSS [3], according to the specifications required for the application (see Section 3.2). A possible solution after optimization is proposed in Section 3.4.4.

3.4.1 First Results

Fig. 3.7(a) shows the first model used for simulations. The first results (see Fig. 3.7(b)) were obtained with the set of parameters listed in Table 3.1.

3.4.2 Parametric Studies

The probe model used for the parametric study was improved with the modifications necessary to enable manufacturing process and mounting.
The feeding line is a standard 2.29 mm coaxial cable, with the center conductor directly connected to the PIFA element. An alumina tube is added to this design to both protect the

Part	Description	Parameter	Value [mm]	Material
base cylinder	diameter	d_{base}	8	Inconel, $\sigma \simeq 9.7 \cdot 10^5$ S/m
	height	H	5	
	hole diameter	d_{hole}	0.889	
	hole offset*	x_{hole}	0.2	
PIFA element	width	W	2.4	
	length	L	1.9	
	vertical wall height	h_{vert}	0.5	
	vertical wall offset*	x_{vert}	0.7	
	thickness	t_{PIFA}	0.2	
probe shell	outer diameter	d_{shell}	9	
	inner diameter	D_{shell}	8	
	height	h_{shell}	8	
cap	diameter	d_{cap}	8	Al_20_3, $\varepsilon_r \simeq 9.5$
	thickness	t_{cap}	0.8	
coaxial line	inner conductor diam.	d_{coax}	0.32	copper, $\sigma \simeq 5.8 \cdot 10^7$ S/m
	outer conductor diam.	D_{coax}	(-)	
cline2-5	dielectric diam.	d_{diel}	0.89	silica, $\varepsilon_r \simeq 1.6$

Table 3.1: PIFA probe first model - summary of the optimized dimensions.
(* the offset is relative to the cylinder center axis)

cable dielectric from pollution and to prevent the escape of the dielectric powder from the inner conductor due to vibrations.
Fig. 3.8 shows the improved probe model, with some relevant investigated dimensions. Table 3.2 shows the influence of the variation of some geometrical features dimensions on the probe response. For each investigated parameter a variation step of 0.1 mm is considered, except for the alumina permittivity variation (step of 0.5).

Description	Parameter	Δ_{nom} [mm]	$\lvert S_{11}\rvert$ [dB]	f_r [GHz]	Remarks
PIFA element width	W	1.4/1.8	-26.15/-23	25.35/25.1	by increasing W, f_r shift to lower values, as expected
alumina cap height	H	2.2/2.3	-30/-20	25.15/26.15	lower f_r with cap closer to the PIFA element
PIFA element length	L	1.6/2.0	-20/-15	25.8/24.8	by increasing L, f_r shift to lower values, as expected
PIFA element offset	x	0.7/1.1	-26/-18	25.15/25.6	by increasing x, f_r shift to higher values, as expected
PIFA element height	h	0.3/0.5	- 20/-32	25.15/22.9	by increasing L, f_r shift to lower values, as expected
alumina permittivity	ε_r	9/11.5	-31/-21	25.15/23.7	>1 GHz shift

Table 3.2: PIFA probe - parametric study

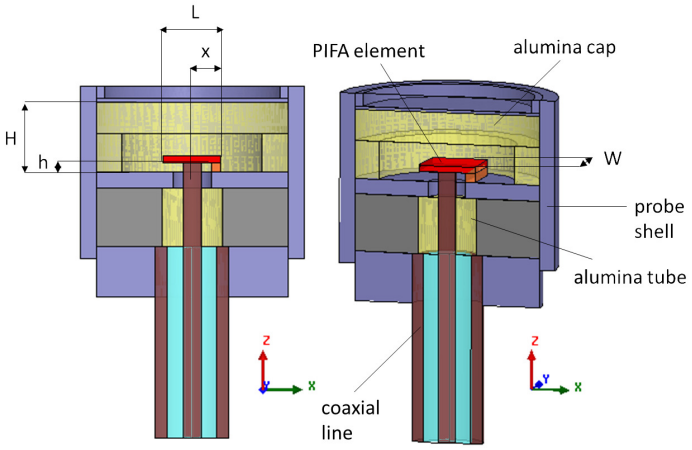

Figure 3.8: 3D and cut view of the PIFA probe showing some relevant investigated dimensions.

3.4.3 Blade-Probe Interaction

A blade passing in front of the probe was simulated using the simplified model shown in Fig. 3.1.

As an example, Fig. 3.9 shows the blade-probe interaction as the blade model sweeps in front of the probe tip perpendicular to the to the PIFA element lenght W, at an average clearance of 2 mm. For simplicity, 5 positions of the axial shift are considered.

The measured model shows good sensitivity toward variations, with maximum reflection when the blade completely covers the probe tip aperture.

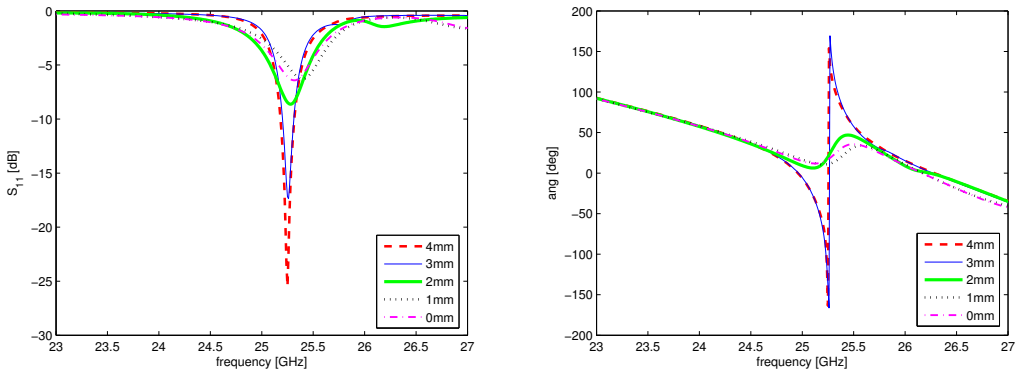

(a) (b)

Figure 3.9: Reflection coefficient of the PIFA probe as the blade is translated perpendicular to the PIFA element lenght W, from 4 mm to 0 mm with respect to the probe tip center at 2 mm-clearance.

3.4.4 Optimized Solution for Prototyping

Table 3.3 shows the set of parameters of the optimized solution proposed for prototyping. Fig. 3.10 shows the reflection coefficient and electric near field of the PIFA probe. Further

Description	Parameter	Value [mm]
PIFA element width	W	1.6
PIFA element length	L	1.8
PIFA element offset	x	0.9
PIFA element height	h	0.3
alumina cap height	H	2.2

Table 3.3: PIFA probe solution for prototyping - summary of the optimized dimensions

possible modifications to the design of the proposed solution include the addition of a tuning ring around the PIFA ground plane or the presence of a tuning slot on the PIFA horizontal element.

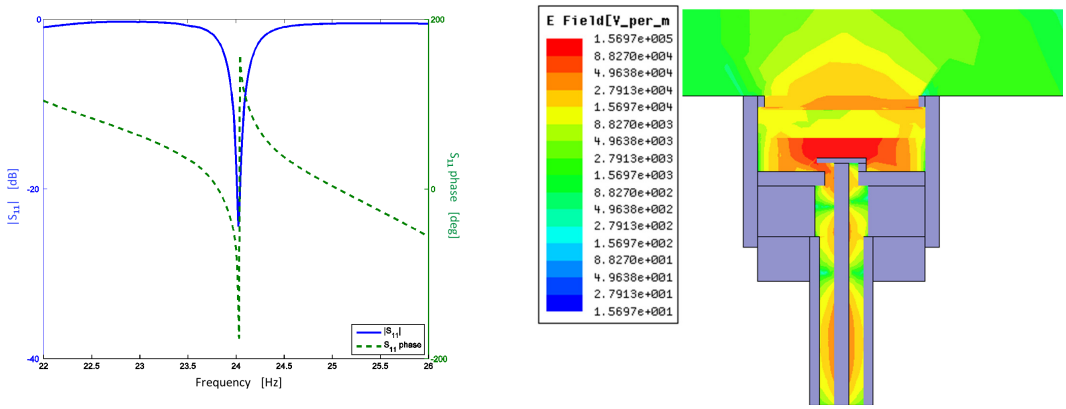

(a) (b)

Figure 3.10: PIFA optimized solution - (a) reflection coefficient and (b) electric near field.

3.4.5 Measurements on Prototypes

The tests performed on built prototypes (see Fig. 3.11) include mechanically static baking cycles up to 850°C and dynamic measurement (in front of rotating blades) at room temperature. For probe temperature cycling, a tube furnace was used that can reach temperatures of 1100°C. Fig. 3.12 shows results obtained from room temperature evaluation of one of the prototypes after cooling. The losses affecting the collected data are due to long feeding cables.

Thermal tests performed on various prototypes did not yield repetitive results, confirming

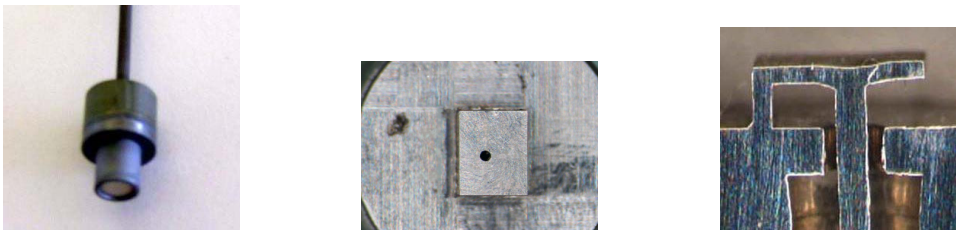

(a) (b) (c)

Figure 3.11: PIFA probe prototype - outer shell (a); insight, top view (b) and side view (c).

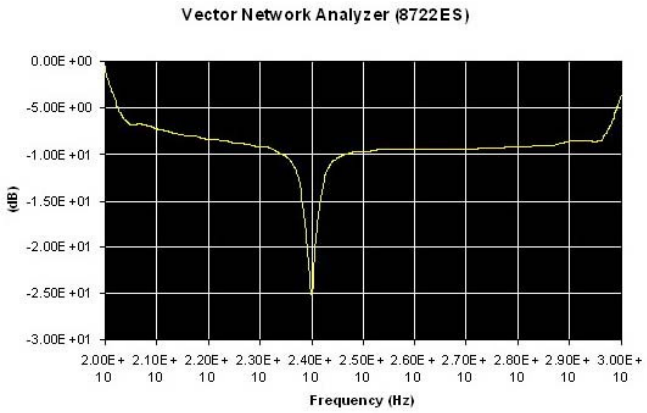

Figure 3.12: Measurements results, $|S_{11}|$

a large influence of temperature on materials (see Table 3.2) which is not acceptable for the aimed application.

3.4.6 Remarks

During the design process it was found that very small dimensional variations have an important influence in the simulations, therefore the fabrication tolerances are very critical.
Room temperature prototypes were built and tested, showing encouraging results. However, this antenna-based solution was found to be too sensitive to temperature drift (as predicted from parametric study results, see Table 3.2), mechanical tolerances and vibration and was finally not considered for testing on real turbines.

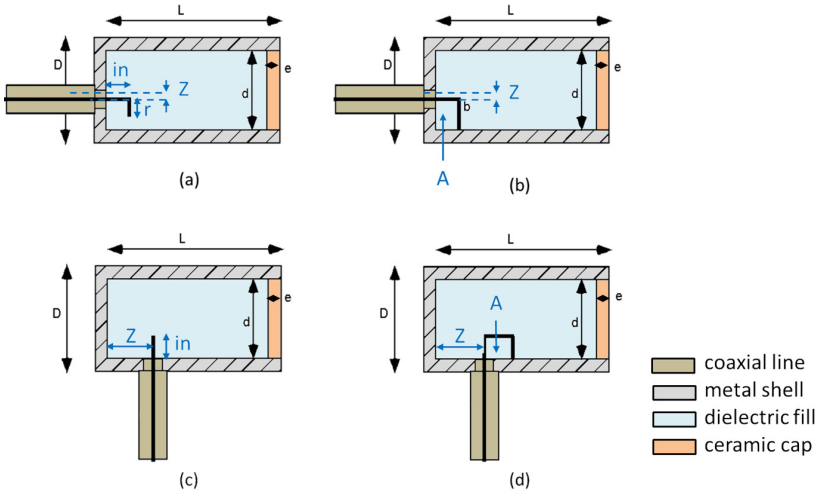

Figure 3.13: Cross-sectional views of the waveguide resonator showing four possible feeding solutions. End-launch feeding with curved coupling probe (a) and short-circuited coupling loop (b). Side-launch feeding with straight coupling probe (c) and short-circuited coupling loop (d).

3.5 24 GHz Open-ended Circular Waveguide Resonator Probe

The 24 GHz open-ended waveguide resonator probe is one of the new resonator-based designs [4, 5], proposed as a valid alternative to the more complex antenna-based designs previously presented [1, 2], and intended for BTC measurement in small-size turbines.
The principle of operation of the circular open-ended waveguide resonator probe has been introduced in Section 2.7.2.6. In this section we present some possible implementations of the probe concept (shown in Fig. 3.13), and provide results of the performed parametric studies on simulated probe models and of the prototypes measurements.
The probe design was studied and optimized through simulation with the finite element method solver ANSYS HFSS, according to the specifications required for the application. Performed investigations were aimed to optimize the probe geometry, and test its ability to operate under harsh environmental conditions (presence of vibrations and large temperature variation) and to yield useful data in the presence of the passing turbine blades.
Prototypes of an optimized probe solution were built and successfully tested in laboratory and on a real turbine engine, demonstrating the suitability of the proposed sensor design for tip monitoring in the turbine harsh environment.

3.5.1 Probe Design and EM Validation

The waveguide geometry that allows for propagating the fundamental TE_{11} mode at the desired cut-off frequency $f_{c(TE11)}$ of 24 GHz was identified according to (2.43), with $p'_{11} = 1.841$. For a hollow waveguide, the minimum radius for the propagation of the TE_{11} mode

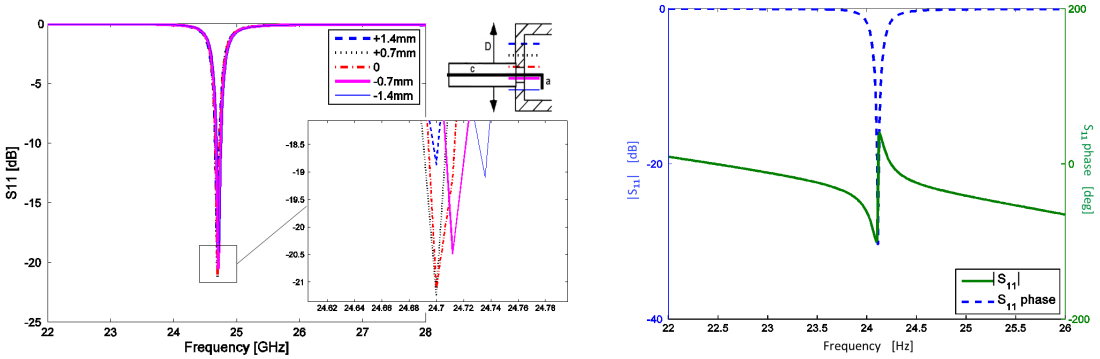

(a) (b)

Figure 3.14: (a)Influence of feed position with detailed view. The coaxial feed positions are indicated as offset with respect to the probe center (0mm), as shown in the top right sketch. Small variations of the reflection coefficient are due to the interaction between the curved end of the probe and the cavity wall, at positions -0.7mm and -1.4mm, (b) reflection coefficient of the optimized model with a side-launch coupling probe. The magnitude is -30.3 dB at 24.11 GHz, the phase is linear out of resonance.

at 24 GHz is $a \simeq 3.6$ mm, while the maximum allowable radius to avoid propagation of high-order modes is $a \simeq 6.1$ mm.
The probe length satisfying the resonance condition 2.20 was adjusted to tune the waveguide resonator at the operating frequency of 24 GHz.
A low permittivity dielectric filling was used to reduce the waveguide dimensions d and L (see Fig 3.13), compared to those of an air-filled waveguide.
The size of a standard 3.6 mm coaxial feeding line was used for simulations.

3.5.1.1 Feeding Methods

Several feeding configurations are possible, as shown in Fig. 3.13(a)-(d).
All the solutions described in Section 2.7.2.7 are capable of exciting the desired field mode. From the engine installation perspective, the side-launch fed designs are more suitable when engine casing containment is an issue, while the end-launch fed designs have as advantage to be field replaceable. From an EM performance point of view, the side-launch fed solutions are more temperature dependent, due to the relative vicinity of the feeding pin to the protective dielectric cap. The optimized model with a side-launch coupling probe shows results comparable to the end-launch solution, as shown in Fig. 3.14(b).

3.5.1.2 Parametric Studies

For a given resonator diameter d and length L, the coupling feed position, shape and depth of insertion were investigated. The relevant parameters for the parametric study are the position of the probe/loop (Z), the length of the straight section of the probe (in) and its curvature

(r), the area (A) bounded by the loop, (see Fig. 3.13). An overview of the qualitative results of optimization is given in Table 3.4. As an example, Fig. 3.14(a) shows the influence of the coaxial feed position in the case of an end-launch waveguide resonator. The change in the coupling of the reflection coefficient is negligible. Anyway, small variations exist due to the interaction between the curved end of the probe and the cavity wall.

Description	Parameter	Remarks
end-launch probe	in	by increasing in, the matching of $\|S_{11}\|$ increases, not critical influence
	r	r should be as small as possible to achieve good coupling, critical influence
	Z	negligible influence
end-launch loop	A	by increasing A good coupling is achievable, critical for large values of A
	Z	negligible influence
side-launch probe	in	by increasing in, the matching of $\|S_{11}\|$ increases, not critical influence
	Z	optimum values of Z should be found around the center of the waveguide sidewall, for Z approaching L the temperature-dependence is critical
side-launch loop	A	by increasing A good coupling is achievable, critical for large values of A with Z approaching L
	Z	critical when approaching L

Table 3.4: Waveguide resonator probe - parametric study, qualitative results

3.5.1.3 Temperature Influence

As found during the design process, the most considerable effect of the large temperature change expected inside a turbine case is the variation of the permittivity of the dielectric parts (see also Sections 3.3.2 - 3.3.3), thus emphasis was placed in minimizing the impact of the ceramic protection cap.
Different materials were tested against temperature in order to find the best candidate for the cap fabrication, i.e. Plastic_1, Alumina_1 and Alumina_2 (with 2 different degrees of purity).
A temperature variation from 25°C to 900°C was simulated by increasing the nominal permittivity value ε_r (at room temperature) of the material by 30% with a step of 5% [6]. For each material, the frequency drift (measured as % of the resonance frequency f_r) and the magnitude of the reflection coefficient $|S_{11}|$ for a maximum permittivity variation $\Delta\varepsilon_r = 30\%$ are compared in Tab. 3.5.
Alumina_1 gave the best results for the considered cavity dimensions, with a low frequency drift and an excellent quality of matching at resonance. The simulated model shows a small shift of the reflection coefficient due to temperature change (see Fig. 3.15), which meets the system bandwidth requirements.

Material	ε_r	$\Delta\varepsilon_r$	**Shift** [% **of** f_r]	$\mid S_{11} \mid$ **[dB]**
Alumina_1	9		0.1	< -14.8
Alumina_2	9.8	30%	0.2	< -11
Plastic_1	5.67		0.4	< -10.1

Table 3.5: Materials vs. simulated temperature variation

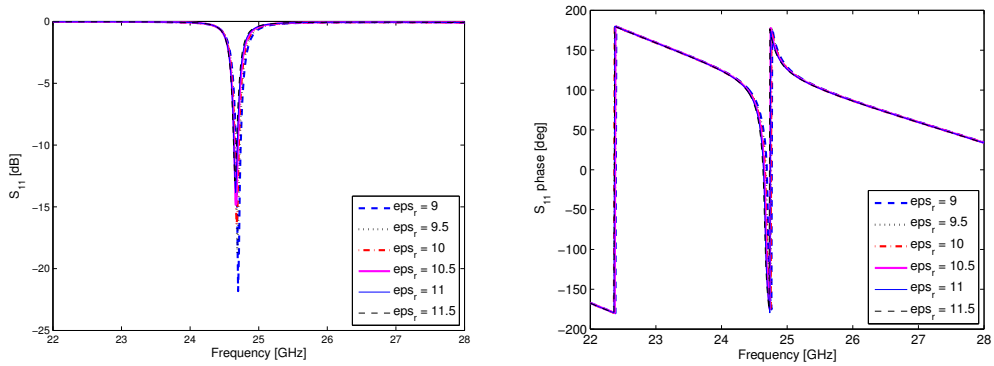

(a) (b)

Figure 3.15: Variation of Alumina_1 cap permittivity ε_r. Magnitude of reflection coefficient at resonance is comprised between -14.8 dB at 24.66 GHz and -21.8 dB at 24.7 GHz (a), phase out of resonance is linear (b).

3.5.1.4 Cap Thickness

The protection cap should be thick enough to allow for easy manufacturing and mechanical robustness, but still be compact in order not to perturb the expected behavior of the sensor. The variation of cap thickness e (see Fig. 3.13) influences the reflection coefficient, shifting the resonance to a lower frequency, as shown in Fig. 3.16

3.5.1.5 Blade-probe Interaction

The simplified blade model of Fig. 3.1 was used to simulate the effect of the passing blade on the EM field of the probe. The blade model was positioned at different distances from the probe tip aperture, for clearances of 0.5 to 6 mm (with a step of 0.5 mm), with a maximum axial shift of ± 10 mm from the probe center and for discrete orientation angles from 0° to 360° (with a step of 30°).
Fig. 3.17(a) shows the EM field of the optimized probe model in free space and the interaction

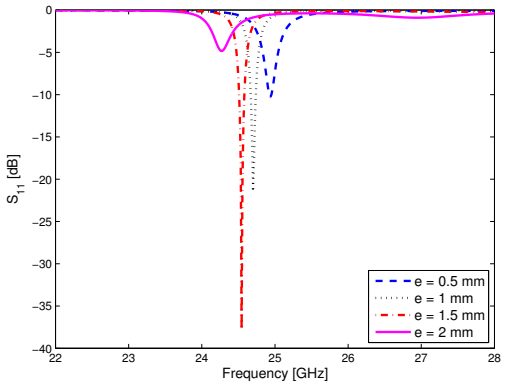

Figure 3.16: Influence of cap thickness e on the reflection coefficient. Increasing e shifts the resonance to a lower frequency.

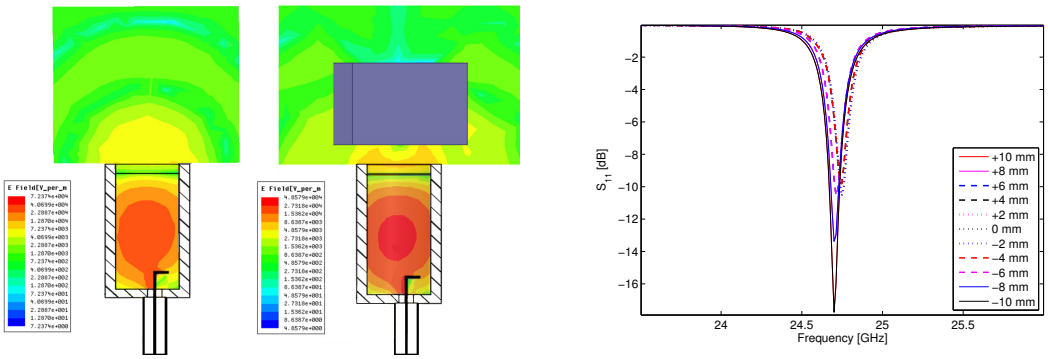

(a) (b)

Figure 3.17: (a) TE_{11} mode at resonance in free space (left), interaction between the simplified blade model and the probe EM field, for a 2 mm clearance and an angular rotation of ∼120° of the blade with respect to the feed plane (right), (b) influence of the blade presence on the reflection coefficient. The blade sweep is simulated by moving a simplified blade model above the blade tip. Results show a blade axial shift of ±10 mm from the probe center (with a step of 2mm), for a typical average clearance of 2 mm, and for an angular rotation of 120° of the blade with respect to the feed plane. The reflection is maximum when the blade completely covers the probe tip aperture.

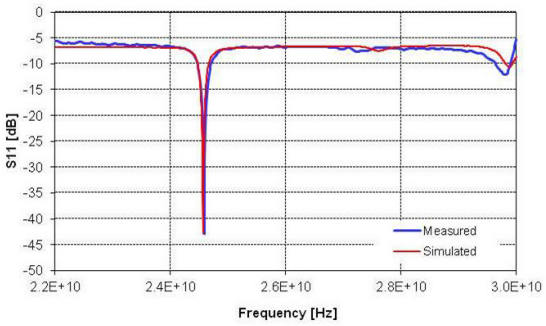

(a)

(b)

Figure 3.18: (a) Comparison between simulated and measured reflection coefficient of the optimized solution at resonance, showing excellent agreement, (b) two prototypes of the 24 GHz waveguide resonator probe.

between the simplified blade model and the probe EM field, positioned above the center of the probe tip, for a typical average clearance of 2 mm, and for an angular rotation of 120° of the blade with respect to the feed plane that was estimated to be the optimum for probe response in the presence of the blade.
The influence of the blade presence on the reflection coefficient is shown in Fig. 3.17(b). The nature of the blade-probe interaction is complex so that it is desirable to fine-tune probe installation parameters during field tests, in order to have maximum consistency of measurements during engine operation (see Section 3.5.2.4).

3.5.1.6 Optimized Solution for Prototyping

The optimized simulated model proposed for prototyping presents a single sharp resonance in the band of interest, in excellent agreement with results obtained from prototype measurement, as shown in Fig. 3.18(a).

3.5.2 Environmental Tests

The built prototypes (shown in Fig. 3.18(b)) were tested in laboratory to verify the reliability and robustness of the selected technology under harsh operating conditions. Results obtained from environmental tests, which included isothermal aging and thermal cycling, were in agreement with simulated results, showing the stability of resonance toward temperature change.
Vibration tests up to 10 kHz were carried out with success on a dedicated test bed. Also, a sensitivity test was done using a precision test set up with actual blades mounted on it, in order to verify blade detection capability inside the engine environment.
Further details on probe installation, probe positioning with respect to the blades and individual probe calibration can be found in [7].

3.5.2.1 Repeatability for Industrialization

Several prototypes were built and measured in order to verify the repeatability on EM performance of the selected technology and thus the suitability for industrial application. Fig. 3.19 shows the comparison of 8 prototypes. Obtained results show some frequency shift between the resonance notches of the measured probes that is within the 10% of the resonance frequency and is due to the manufacturing process and uncertainty on dielectric filling material. The response shift is within the band of interest and is considered acceptable for the application.

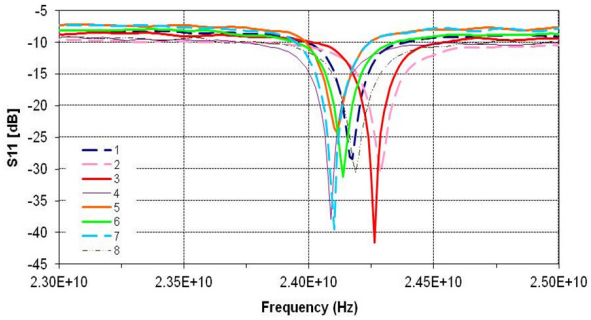

Figure 3.19: Measurement of 8 random probes. Shift of resonance notch, which is due to manufacturing process, is tolerated by the system bandwidth requirements.

3.5.2.2 Vibration Tests

Vibration tests were carried out using a dedicated shaking test bed composed by a signal generator, a power amplifier, a VNA, an oscilloscope and a shaker. Vibrations were applied in a direction perpendicular to the cavity side walls. Probes were tested for periods of 5 and

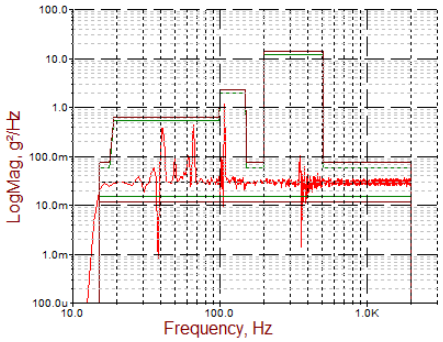

Figure 3.20: Vibration characteristics in the 15-2000 Hz band.

3 hours respectively under random sinusoidal vibration in the 15-2000 Hz frequency band (see Fig. 3.20) and in the 2000-10000 Hz frequency band (see Table 3.6). The frequency of

Vibration	Frequency Range	Parameter	Magnitude
Sinus	2000-10000 Hz	Acceleration	5 g-peak
		Sweep Rate	1 oct/min
		Vibration Time	3h

Table 3.6: Vibration characteristics in the 2000-10000 Hz band.

resonance was monitored over the entire duration of the test showing minimum change, as shown in Fig. 3.21(a) and 3.21(b). A change of 0.2 dB on the minimum value of $\mid S_{11} \mid$ occurring at high frequency vibration can be considered as noise of the measurement, and thus negligible.

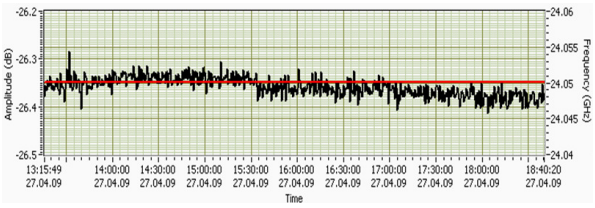

(a) Random and sinusoidal vibration at low frequency (up to 2 kHz)

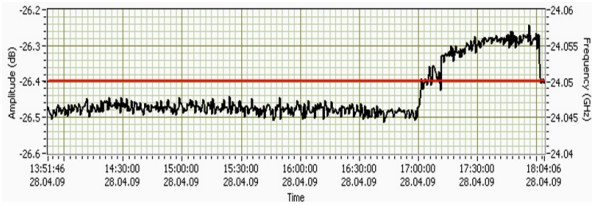

(b) Sinusoidal vibration at high frequency (2-10 kHz)

Figure 3.21: Vibration test results. Frequency notch is monitored for the entire duration of tests showing minimum oscillation around the center frequency value (straight red line).

3.5.2.3 Thermal Tests

Thermal tests included isothermal aging at 900°C for over 4500 hours and thermal cycling from 20°C to 850°C with 5 bar cooling air for about 1200 cycles. The resonance was monitored for the entire test showing great stability toward high temperature extremes, as shown in Fig. 3.22.

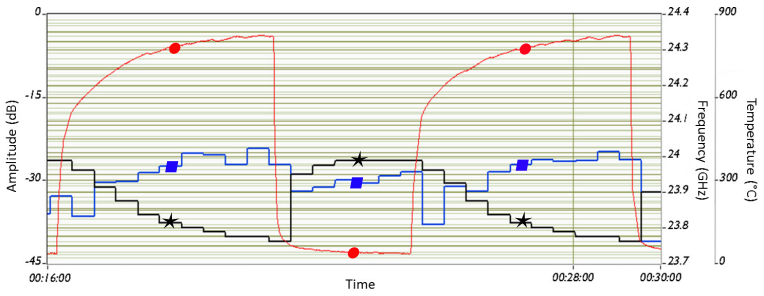

Figure 3.22: Thermal test results. Thermal gradient applied to the probe (circle). Notch depth (square) and center frequency (star) show minimum oscillation.

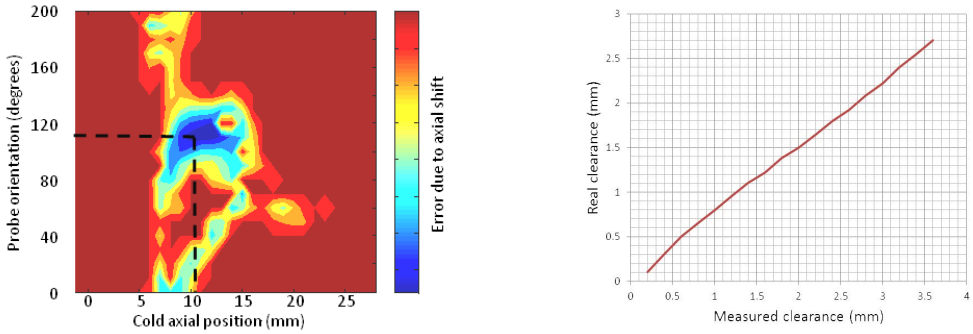

(a) (b)

Figure 3.23: (a) Optimization of probe installation position. The measurement error due to axial shift during engine operation is calculated for different combination of orientation and cold axial position. An optimum is obtained for 10 mm of cold position and 110° of orientation, (b) linearity between real and measured clearance.

3.5.2.4 Installation Sensitivity Test

In order to have an optimal blade detection capability, the positioning of probes as well as their angular orientation must be tuned with respect to the blade, taking into consideration the rotor axial shift during engine operation [8]. For this purpose, the probes axial position (0 at the leading edge of the blade) and orientation (on-axis rotation) was randomly changed and the measurement error due to the axial shift was computed. The optimum probe installation position, depending on the orientation and the cold position is indicated by the dashed lines in Fig. 3.23(a).

To further improve the measurement precision, each probe was individually calibrated using a precision test set-up, in order to remove systematic errors due to the blade geometry and probe manufacturing.

After a calibration at the optimum probe installation position, results show good linearity between real and measured clearance, as in Fig. 3.23(b). The error due to the rotor axial

shift was estimated to be within ±0.1mm.

3.5.3 On-engine Tests

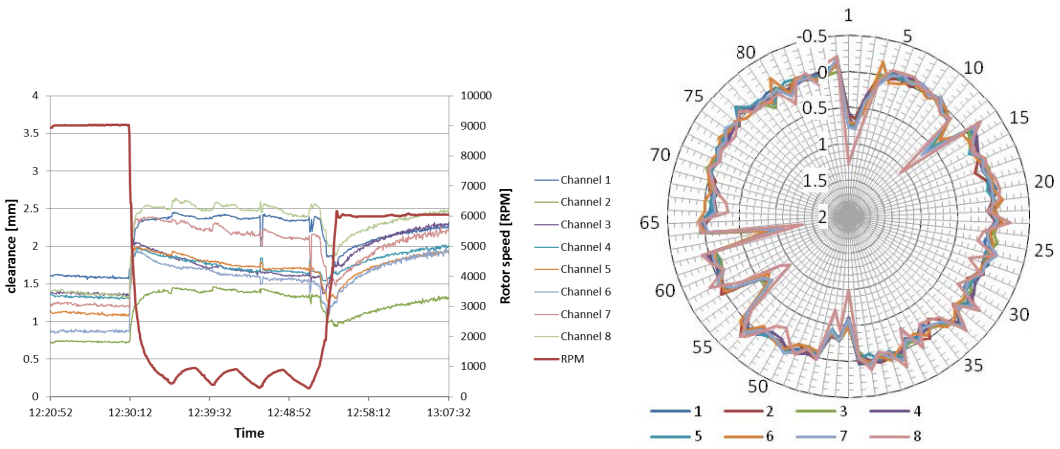

(a) (b)

Figure 3.24: (a) On-line measurements during shut-down, cooling, and hot restart (on 8 channels, 1 per probe). (b) Averaged blade patterns measured by 8 probes. Blade patterns correspond to the individual clearance relative to the mean one (the unit is in millimeters). The numbers on the external disc indicate the blade number.

The measurement capability of the tip clearance monitoring system must be validated on a real engine, as in [9]. For this purpose, a field test campaign of the system was performed on a real gas turbine engine, in collaboration with a gas turbine company.
Eight microwave probes were mounted in the high pressure turbine stage of a DM80 engine (25 MW rated output power) with clearance being monitored during engine operation. In order to evaluate the tip clearance microwave system in terms of measurement performance, two types of results are considered.
The first one is the consistency of measurements, which were carried out over different engine operation modes (i.e. engine cold start-up, shut-down, cooling, and hot restart). The microwave system was able to measure clearance correctly during the different phases, as the measured values are consistent from probe to probe and with respect to the expected engine behavior.
As a sample, Fig. 3.24(a) shows on-line measurements during an emergency shutdown from full output power (25 MW), followed by rotor spins to cool the components and a hot restart. It is clearly observed that the clearance measured on each channel is consistent with the different operating modes of the engine.
The second type of result is the ability of the system to measure individual blade clearances. This measurement is necessary to detect the minimal clearance (i.e. the blade that will rub the casing first) as well as possible blade cracks, by tracking a quick change of the blade size.

To test this, the rotor was modified by shortening ten blades at different heights and in a recognizable pattern. An example of measurement results is shown in Fig. 3.24(b).
The shorter blades are detected and correspond to the actual modification of the engine. Small differences in probes response are due to calibration imperfection and probe sensitivity to small differences in the blades geometry, as explained more in detail in [7].

3.5.4 Remarks

The new microwave monitoring system was proven to be suitable for operation inside the turbine engine harsh environment [10].
Clearance measurement obtained during the different tests are within the range of expected values and directly usable for test engineers. Long term tests campaigns are anyway recommended to confirm the stability of the system and robustness of probes towards aging.

3.6 6 GHz Open-ended Coaxial Resonator Probe

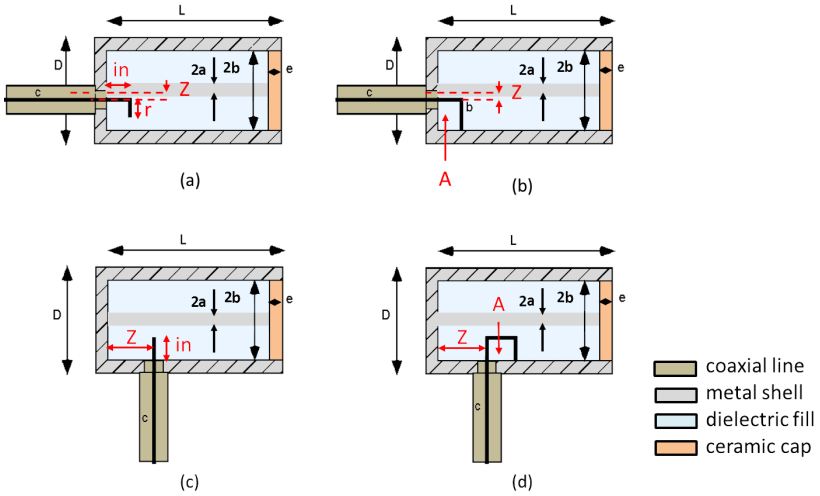

Figure 3.25: Cross-sectional views of the coaxial resonator showing four possible feeding solutions. End-launch feeding with curved coupling probe (a) and short-circuited coupling loop (b). Side-launch feeding with straight coupling probe (c) and short-circuited coupling loop (d).

The 6 GHz coaxial resonator-based design [4, 11] was studied as an interesting alternative to the 24 GHz circular waveguide resonator probe. This design can achieve further miniaturization thanks to its cut-off frequency $f_c = 0$. Furthermore, the radially symmetric dominant TEM mode supported by the coaxial resonator is particularly suitable for blade tip measurement where radiation properties should be as less sensitive as possible to probe mounting orientation.
The principle of operation of the open-ended coaxial resonator probe has been introduced in

Section 2.7.2.7. In this section we present some possible implementations of the probe concept (shown in Fig. 3.25), and provide results of the performed parametric studies on simulated probe models and of the prototypes measurements.
The probe design was studied and optimized through simulation with the finite element method solver ANSYS HFSS, according to the specifications required for the application. Performed investigations were aimed to optimize the probe geometry, and test its ability to operate under harsh environmental conditions (presence of vibrations and large temperature variation) and to yield useful data in the presence of the passing turbine blades. Prototypes of an optimized probe solution were built and successfully tested in laboratory, demonstrating that the proposed sensor is a good compromise between performance, simplicity and robustness toward the turbine harsh environment of operation, with improved performance with respect to other comparable existing probe technologies, as explained more in detail in Section 3.6.2.

3.6.1 Probe design and EM Validation

The coaxial geometry that allows for propagating the fundamental TEM mode, avoiding the propagation of higher-order modes at the desired working frequency of 6 GHz, according to (2.59), imposes an upper limit for the coaxial size being $a + b < 6$ mm.
The probe length L satisfying the resonance condition (2.20), at the operating frequency of 6 GHz, was identified and tuned to couple the EM signal into the coaxial resonator. For all the investigated solutions, the space between the coaxial conductors is air-filled ($\varepsilon_r \simeq 1$).

3.6.1.1 Parametric Studies

The relevant parameters for the parametric study are the length of the straight section of the probe (in) and its curvature (r), the area (A) bounded by the loop, the length of the resonator (L) and the cap thickness (e) (see Fig. 3.25).
On the basis of the performed parametric studies, some qualitative remarks are possible for small variation of the considered parameters:

- for a fixed coaxial length L, a and $b \rightarrow$ increasing in (or A) will increase the coupling of the probe (the loop in the Smith Chart will be wider),
- for a fixed feed length in (or increased A), a and $b \rightarrow$ increasing L will shift resonance to a lower frequency,
- for a fixed L, in (or increased A), a and $b \rightarrow$ increasing e will increase the coupling of the probe and shift the resonance to a lower frequency.

This is true for end-launch coaxial probes, but similar reasoning can be done for side-launch solutions.
It must be noticed that the position of the probe/loop (Z) should be kept at distance from

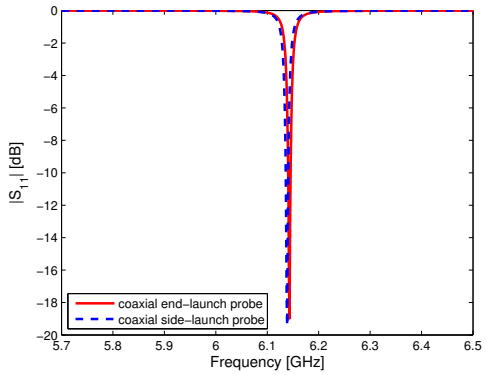

Figure 3.26: Comparison between an end-launch and a side launch fed coaxial probe, showing comparable results.

the two coaxial conductors to achieve reasonable coupling, so that it can be considered as fixed in the end-launch case. On the other hand, in the side-launch case, the position of the probe/loop (Z) has negligible impact on the probe response, provided that it is kept within the region where the field is slowly varying (around $Z = \lambda/4$).
Two possible solutions with end-launch and side-launch feed are shown in Fig. 3.26, yielding comparable results.

3.6.1.2 Temperature Influence

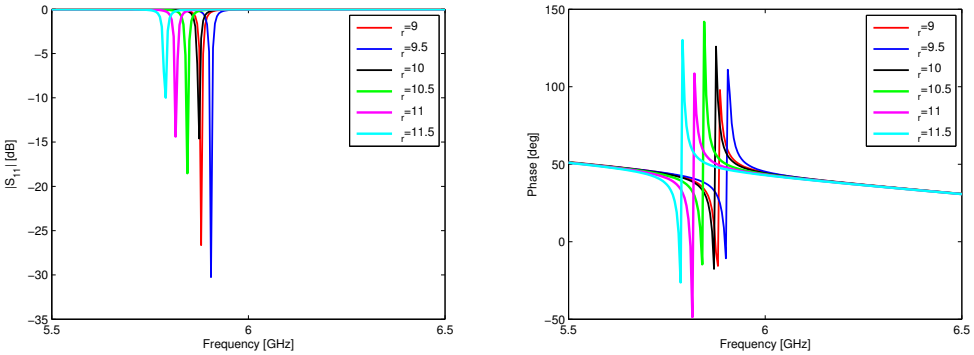

(a) (b)

Figure 3.27: Simulated reflection coefficient magnitude (a) and phase (b) of the probe in the presence of a simulated temperature change. The nominal permittivity value ϵ_r (at room temperature) of the ceramic cap is increased by 30% with a step of 0.5.

A large temperature variation was simulated by increasing the nominal permittivity value ϵ_r (at room temperature) of the ceramic cap by 30% with a step of 0.5. The simulated model

presents a shift of the reflection coefficient which remains in the acceptable frequency range, with a matching better than -20 dB, confirming that high temperature prototypes of the proposed design are feasible. (see Fig. 3.27).

3.6.1.3 Blade-probe Interaction

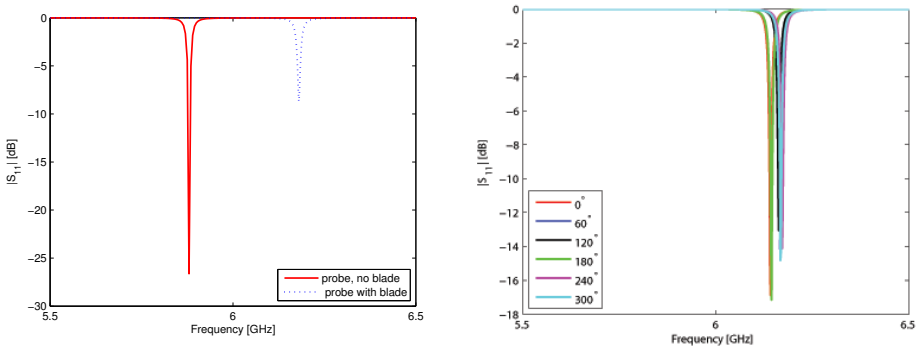

(a) (b)

Figure 3.28: Simulated reflection coefficient of the probe without blade and with blade in front of it at 0.5 mm-clearance from the probe tip. The sensor impedance matching changes with blade presence. (b) Simulated reflection coefficient of the probe for different orientations in the presence of a simplified blade model at 2mm-clearance from the probe tip.

Investigations showed that the simulated reflection coefficient of the probe changes significantly when a blade model is added near the probe tip (see for example Fig. 3.28(a)), confirming that the probe acts as an effective BTT proximity sensor. As expected, simulation results also showed a weak sensitivity of the reflection coefficient to probe orientation with respect to the target (Fig. 3.28(b)). Smalll discrepancies between the resonances might be due to the asymmetry of the feeding structure.

3.6.1.4 Optimized Solution for Prototyping

The optimized simulated solution proposed for prototyping presents a single sharp resonance in the band of interest, in excellent agreement with results obtained from prototype measurement, as in Fig. 3.29(a).

3.6.2 Environmental Tests

The built prototypes (as the one shown in Fig. 3.29(b)) were tested in laboratory to verify the reliability and robustness of the selected technology under harsh operating conditions.
The probes endured a 200°C isothermal test for 500 hours and a thermal cycling from 23 to 200°C for 500 cycles, without any degradation on EM performance observed.
The probes also went through vibration tests done in the 10-16000 Hz frequency band with

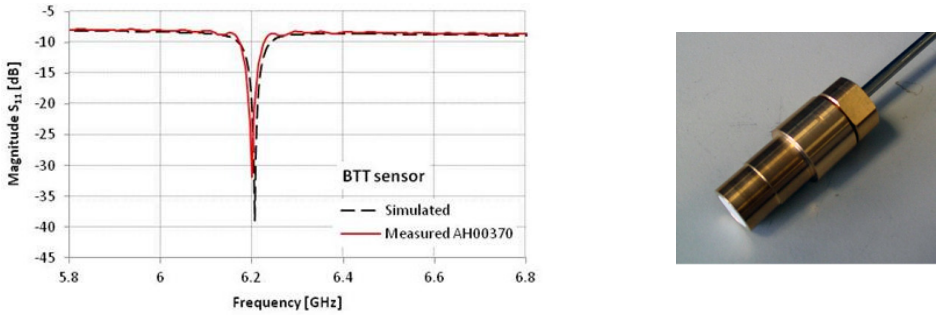

(a) (b)

Figure 3.29: (a) Comparison between simulated and measured reflection coefficient of the optimized solution at resonance, showing agreement, (b) prototype of the 6 GHz coaxial resonator probe.

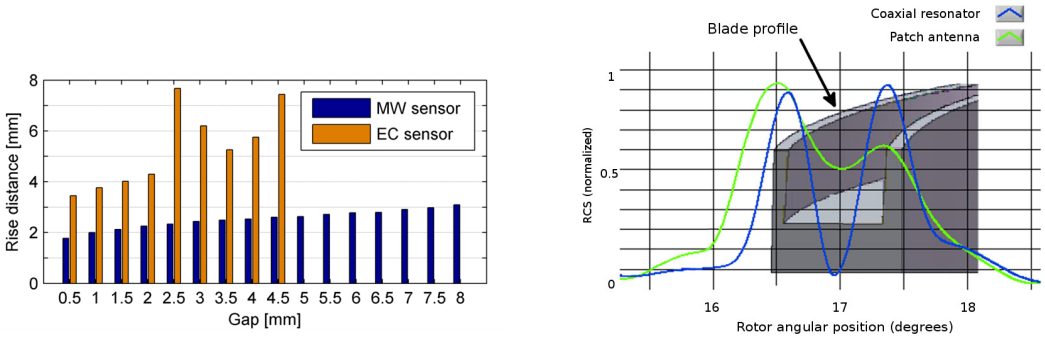

(a) (b)

Figure 3.30: (a) The rise distance of the coaxial probe is consistently lower compared to the EC sensor. In addition, the EC sensor failed to measure targets farther than 4.5mm, while the microwave probe could measure as far as 8.0 mm and above. (b) Radar Cross Section, the coaxial resonator has better spatial resolution compared to a 5.8 GHz patch probe.

an acceleration of 5g peak. Results have shown that a dwell of 10^7 cycles has no impact on probe RF performance.

The measurement capabilities of the coaxial resonator probe were evaluated and compared to those of an Eddy current (EC) probe suited for BTT measurements. Two metrics were evaluated on both probes: spatial resolution and bandwidth.

The spatial resolution was measured in term of rise distance, i.e. the distance that the blade tip needs to travel in front of the probe tip for the signal amplitude to go from 20 to 80% of its peak value (corresponding to the moment when the blade is exactly in front of the probe). Thus, a shorter rise distance indicates a better spatial resolution. A rectangular target (2.5x25.0mm) at a target-probe clearance ranging from 0.5 to 8.0 mm. The coaxial probe consistently showed an improved rise distance compared to the EC sensor, which was not

able to sense the target at clearances larger than 4.5 mm (Fig. 3.30(a)). As a consequence, the microwave sensor not only has a better spatial resolution than the EC sensor, but also a significantly greater measurement range.
The second metric used for the comparison is the bandwidth, which indicates the maximum excitation frequency that the sensor is able to sense.
In the case of BTT, a higher bandwidth allows to measure blades at higher speeds without losing accuracy. The bandwidth of the coaxial probe was measured by using a wideband horn antenna to stimulate the sensor with a modulated wave. The coaxial probe showed a significantly higher bandwidth (-3 dB attenuation point at 5.3 MHz) compared to the EC probe (-3 dB at 120 kHz), allowing BTT measurements at very high blade speeds.
The coaxial resonator probe supports a radially symmetric TEM mode, thus the sensor response is independent to the mounting orientation and is able to provide accurate BTT measurements even in the presence of torsional blade vibration modes, unlike existing 5.8 GHz patch antenna probes (see Fig. 3.30(b)).

Bibliography

[1] J. L. Geisheimer, S. A. Billington, D. Burgess, and G. Hopkins, "Microstrip patch antenna for high temperature environments," *United States Patent No. 7,283,096*, October 16, 2007.

[2] M. Violetti, J.-F. Zürcher, J. Geisheimer, and A. K. Skrivervik, "Design of antenna based sensors for blade tip clearance measurement in gas turbines," in *Proc. 4th European Conference on Antennas and Propagation*, 12-16 April, Barcelona, Spain 2010.

[3] Ansys High Frequency Structure Simulator (HFSS). [Online]. Available: http://www.ansys.com/

[4] M. Violetti, A. K. Skrivervik, Q. Xu, J. Geisheimer, and G. Egger, "Device and method for monitoring rotor blades of a turbine," *European Patent Application No. 11181622*, Sept. 16, 2011.

[5] M. Violetti, Q. Xu, M. Hafner, and A. K. Skrivervik, "New microwave sensing system for blade tip clearance measurement in gas turbines," *to be presented to IEEE Sensors Conference*, Oct. 28–31, 2012, Taipei, Taiwan.

[6] M. K. Park, H. N. Kim, S. S. Baek, E. S. Kang, Y. K. Baek, and D. K. Kim, "Dielectric properties of alumina ceramics in the microwave frequency at high temperature," *Solid State Phenomena Vols. 124-126*, pp. 743–746, 2007.

[7] D. Kwapisz, M. Hafner, V. Spitsyn, M. A., and V. Berezhnoy, "Test and validation of microwave tip clearance sensor on a 25 MW gas turbine engine," in *XVI International congress of propulsion engineering*, Rybachye, Ukraine 18 Sept. 2011.

[8] D. Kwapisz, M. Hafner, and S. Queloz, "Calibration and characterization of a cw radar for blade tip clearance measurement," in *Proceedings of the 7th European Radar Conference (EuRAD)*, Sept. 30-Oct. 1 2010, pp. 320–323.

[9] E. B. Holmquist and P. L. Jalbert, "Turbine blade tip clearance measurement instrumentation," in *Proc. ASME Turbo Expo 2007: Power of Land, Sea and Air*, Montreal, Canada May 14-17, 2007.

[10] M. Violetti, Q. Xu, M. Hafner, and A. K. Skrivervik, "New microwave sensing system for gas turbines health monitoring," in *submitted to IEEE Sensors Journal*, 2012.

[11] M. Violetti, Q. Xu, O. Hochreutiner, and A. K. Skrivervik, "New microwave sensor for on-line blade tip timing in gas and steam turbines," *submitted to Asian-Pacific Microwave Conference, APMC*, Kaohsiung, Taiwan, Dec. 4–7, 2012.

4 Rubidium Miniature Atomic Clocks

4.1 Outline of the Chapter

In this chapter we provide an overview on the physical principle of operation of atomic clocks, focusing on the specific case considered in this work, namely miniature laser-pumped double-resonance (DR) Rubidium atomic clocks (or Rubidium atomic frequency standards, RAFS). A non-exhaustive description of existing miniature atomic frequency standards is given, along with a comparison in terms of size, stability and power consumption.
This work will treat the design of the Physical Package of a miniature laser-pumped DR Rubidium atomic clock, and in particular the conception of a miniaturized microwave resonator (MWR).
In this chapter we introduce the general EM requirements of the microwave cavity and the theoretical aspects relevant for the conception of MWR suitable for atomic clocks. More specifically, we describe the principle of operation of a cavity geometry known as Loop-Gap Resonator (LGR), relevant for the design of the miniaturized MWR solutions proposed in Chapter 5.

4.2 Overview on Rubidium Atomic Clocks

Atomic frequency standards achieve unmatched frequency stability over long periods of time by exploiting a well-defined atomic transition for steering the output frequency of a quartz oscillator [1, 2]. They are of paramount importance in those systems that require an accurate measurement of time. Typical applications include radio-astronomy, navigation and positioning systems like Galileo and GPS (where an error of 1 nanosecond in time resolution means an uncertainty of 30 centimeters in the measured position), telecommunication systems (for the purpose of networks synchronization) and metrology.
Rb frequency standard clocks are low cost and can achieve a short-term stability of $10^{-12}\tau^{-\frac{1}{2}}$ (meaning an error of 1 second over 32000 years) with a less complex system compared to other existing frequency standards. This facts make them very attractive for many commercial, portable and aerospace applications.

4.2.1 Principle of Operation

The physical working principle of an atomic clock is based on the interaction between an EM radiation and the electrons of excited atoms with quantized energy levels. The interaction occurs through three phenomena: absorption, stimulated emission and spontaneous emission.

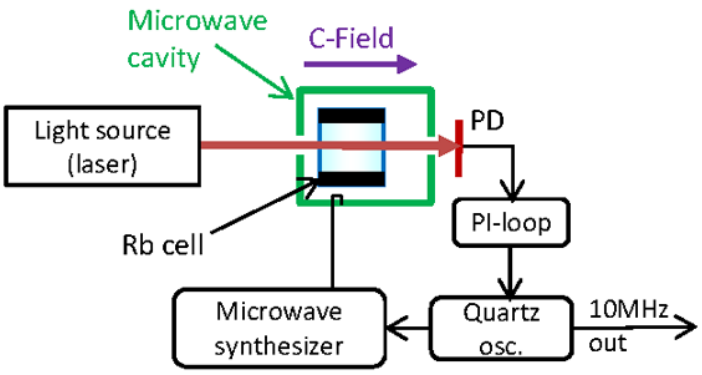

Figure 4.1: Block scheme for a DR atomic clock.

The first is simply the absorption of EM radiation energy by electrons that are excited to higher energy levels. In absence of a continuous source, the atoms come back to the fundamental state releasing the received energy in a spontaneous or stimulated way.
Cycles of absorption and emission between two atomic levels 1 and 2 can create an oscillator. However, since the energy difference between the two levels is usually in the range of microwave frequencies, in order to have a stable oscillator using stimulated emission we need a population inversion, that occurs when more electrons are present in 2 than in 1. For this purpose, an auxiliary energy level 3 is needed where to pump the electrons of the ground state 1. When an optical pumping is used, the excited electrons will spontaneously decay to both the lower ground states but the net result of the pumping will be a population inversion. The continuous optical excitation brings after a time all the electrons in the state B, and if a microwave excitation is applied with appropriate frequency is applied, oscillations are driven. The light radiation generated by this three-state oscillations represent the "clock transition" signal and can be directly detected by a photodetector (PD) as shown in Fig. 4.1.

In this work we will consider the case of Rubidium atoms, in particular the ^{87}Rb isotope used in frequency standards.
The transition that we will consider in this work is the D2 line (at 780.24 nm) between the states $5S_{\frac{1}{2}}$ and $5P_{\frac{3}{2}}$, and the degenerated levels $F = 1$ and $F = 2$ of the $5S_{\frac{1}{2}}$ state, with an energy difference corresponding to 6.835 GHz, are chosen as the clock transition.
In order to guarantee a pure spectral line and a stable frequency standard, we need to take into account that the chosen reference levels are degenerated. The degeneracy of the level $F = 1$ and $F = 2$, which must be avoided to obtain a pure spectral line and a stable frequency standard, is called Zeeman splitting and can be prevented applying a constant magnetic field (called C-field). Among all possible transitions between the levels with different m_F value, the most stable one must be selected. Denoting with $|F, m_F\rangle$ the atomic state, the best choice is the transition $|1, 0\rangle \rightarrow |1, 0\rangle$ which has acceptable stability versus the amplitude of the applied external field.
It can be demonstrated that if the microwave magnetic field is completely oriented in the

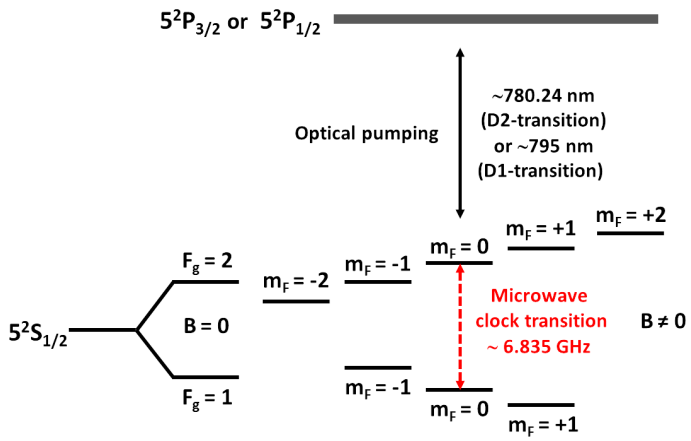

Figure 4.2: DR principle - ^{87}Rb atomic energy-level scheme.

z-direction corresponding to the quantization axis defined by the direction of the constant magnetic field (C-field), only the transitions with $\Delta m_F = 0$ (or π transitions), are possible [3], thus including the selected $|1,0\rangle \rightarrow |1,0\rangle$. If the magnetic field has components in the x- and y-direction $0 \rightarrow -1$ and $0 \rightarrow +1$ transitions will exist (σ transitions).
In summary, a Rb atomic clock is an optically pumped three-level system with a microwave coupling between the two ground states. Since the Rb atoms ground states are degenerated, a C-field is used to lift this degeneracy (split away from each other the ground levels) and isolate the 0-0 transition.
A system like the one just described uses the principle of the Double Resonance (DR), of which a detailed analysis can be found in [4].
In the DR scheme using a ^{87}Rb cell implementation considered in this work (see Fig. 4.1), resonant light from a laser source optically pumps the atoms, thus depleting one of the atomic ground states and populating the other one, i.e. creating a polarization of the atomic ground-state as shown in Fig. 4.2.
Simultaneously, a microwave field is applied to the atoms via the microwave cavity (MWR). Its frequency, resonant with the ^{87}Rb clock transition $(5^2S_{1/2}|F_g = 1, m_F = 0\rangle \rightarrow |F_g = 2, m_F = 0\rangle)$, it is generated by a voltage controlled crystal oscillator whose frequency is multiplied. The light power transmitted through the ^{87}Rb cell, as a function of the microwave frequency, is a measure of the atomic ground-state polarization, and yields the microwave "clock transition" signal which is detected in the transmitted light intensity by the PD. The "clock transition" signal typically has a Lorentzian shape, and the stabilization of the quartz oscillator to the center of this signal realizes the clock.

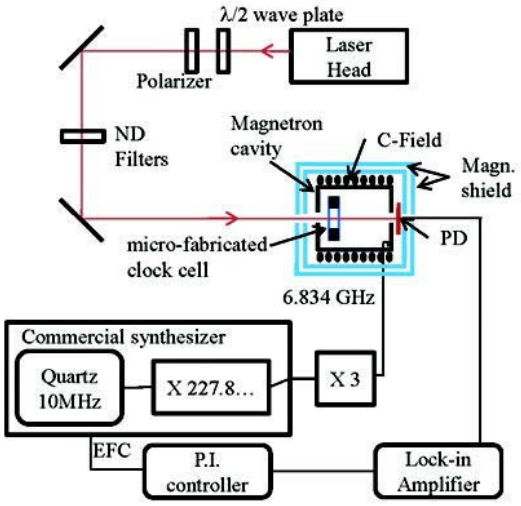

Figure 4.3: Schematics of the atomic clock structure.

4.2.2 Miniaturized Laser-Pumped DR Rubidium Atomic Clocks

The development of miniaturized frequency references is of particular relevance considering certain portable applications, for instance in telecommunications or for military purposes. The past decade has seen rapid progress in the development of chip-scale atomic clocks (CSAC), achieving clock integration in volumes of a few cm^3, and a total power consumption around 100 mW [2, 5], while showing a fractional frequency instability (Allan deviation) below 10^{-11} at 1 hour, i.e. several orders of magnitude better than a quartz oscillator of comparable size and power consumption.
Most approaches to CSAC were based on the CPT scheme [2], while the classical optical-microwave double-resonance (DR) scheme [1, 6] - although allowing for better clock stability - was only rarely studied [7, 8]. In comparison with CPT, the double-resonance approach has several advantages. Thanks to the absence of non-resonant laser modulation sidebands, the background level of the output signal is reduced. In addition, it allows a 10 times higher amplitude with degradation of the line-width by only a factor of 2. Therefore, in similar operating conditions, DR allows a typically 5 times better short-term stability [7]. In recent years, laser optical-pumping has substantially improved the achievable frequency stabilities of Rubidium vapor cell standards with respect to DR frequency standard with a spectral lamp as pumping source, as reported in [9, 10].

4.3 System Architecture

In general, the structure of an atomic clock can be divided in two parts, namely the Physics Package (PP) where the optical and microwave excitations interact with the vapor atoms,

and the Electronic Package (EP) that controls the output signal (see Fig. 4.3). In the EP, the frequency of a voltage-controlled crystal oscillator, scaled up by a factor of M, is locked to the hyper-splitting frequency (6.835 GHz for ^{87}Rb) using phase sensitive detection. The control-voltage corrects the crystal oscillator. Detailed overviews on possible implementations of the EP can be found in [1, 11].
The PP of an atomic clock can be divided in 8 parts (as shown in Fig. 4.4):

- **Rb vapor cell** - Rb atoms are contained in vapor form in a glass cell. Different types of vapor cells can be distinguished on the basis of the method used to contain the Rb atoms [12]. In this work we will consider vapor cells containing a mixture of Rubidium and buffer gas (argon or neon). The presence of a buffer gas provides an inert atmosphere for the very reactive Rb atoms and helps preventing the collisions of Rb atoms with the cell walls that might cause perturbations in the clock signal.

- **Microwave cavity** - a cavity working at 6.835 GHz is needed in order to introduce the required electromagnetic field required for the correct hyperfine transition. The cavity has holes at its bottom and top ends so that the laser beam can pass through, interact with the Rubidium atoms contained in the vapor cell and finally reach the photodetector.
- **Laser head** - laser light resonant with the Rb D2-line (λ=780 nm) and directed along the quantization axis (C-field direction) excites the Rb atoms, inducing the needed atomic polarization.
- **Photodetector (PD)** - The light intensity transmitted through the Rb vapor cell is detected on a photodiode as a function of the microwave frequency injected into the cavity.
- **C-field coil** - the constant field needed to isolate the clock transition and it is typically obtained by means of a coil wrapped around the cavity.
- **Magnetic shield** An outer magnetic shield is needed in order to isolate the Rb atoms from external uncontrolled magnetic fields (e.g. earth, steel tools, etc.). Such magnetic shield is typically made of μ-metal, i.e., a special metal with very high permeability.
- **Optical elements** - are used to focus the laser beam through the vapor cell for optimal interaction with the Rb atoms.
- **Heaters** - are used to stabilize the temperature of operation. Any fluctuation in temperature would lead to fluctuations in clock frequency, as Rb atoms frequency is temperature dependant [11, Ch. 7].

4.3.1 EM Requirements

In order to ensure the correct transition between the two Rubidium hyperfine levels $F = 1$ and $F = 2$, the MWR must satisfy the following requirements:

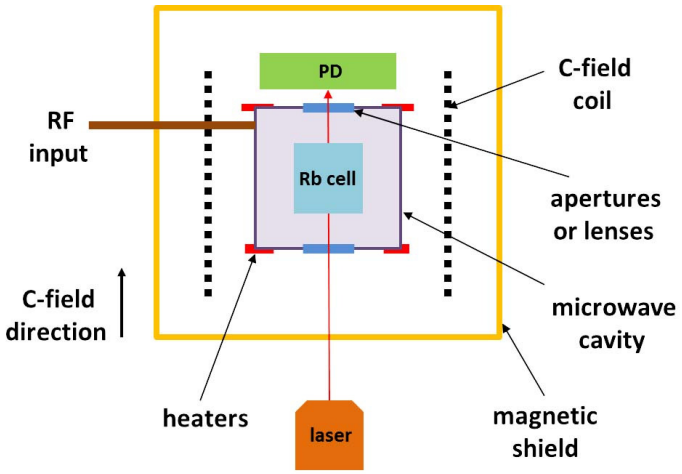

Figure 4.4: Schematics of the atomic clock PP.

- The resonance frequency of the cavity must be 6.835 GHz. This frequency is strictly related to the geometry of the cavity which must be as small as possible.

- The magnetic field distribution must be z-oriented (parallel to the light beam and to the direction of the C-field) to avoid σ Zeeman transitions, and as uniform as possible to excite all atoms in the same way. In order to evaluate the quality of the field distribution, two specific EM parameters - the filling factor (FF), and the Field Orientation Factor (FoF) - will be introduced in Section 4.4.1.2 and 4.4.1.2.

- Quality factors with values less than 200 are sufficient to assure good clock signals, while limiting the cavity pulling effect [11, Ch. 7]. This is true for passive Rb frequency standards as the one considered in this work, while in the case of active atomic clocks (Microwave Amplification by Stimulated Emission of Radiation devices, or MASERs) quality factors larger then 10000 are required [11, Ch. 7]. In any case, and in order to save power consumption, a good coupling is desired.

4.3.2 Miniaturization of the MWR

In view of mobile and battery-powered applications, there is an increasing demand for more radically miniaturized and low-power frequency standards.
For the miniaturization of a DR atomic clock, the size reduction of the MWR to well below the wavelength of the atomic transition (4.4 cm in the case of ^{87}Rb) has been a long-standing issue. Microwave cavities used for such applications include circular cylindrical cavities using the TE_{011} and TE_{111} modes, because both modes have a good quality factor. These cavities have good electromagnetic properties but are too large for many telecommunication applications. Also, the size of the cavity should be kept compact to limit the power consumption, especially in the temperature control.

In order to reduce this size, a rectangular dielectric loaded cavity using the TE_{101} mode was proposed in [13]. Many other cavity shapes using different modes have been proposed, with the aim of reducing the size and power consumption of the physics packages, while keeping a reasonable stability. One very interesting solution was proposed using a deformed coaxial cavity in the TEM mode [14], yielding a very compact design with good performances.
All these physics packages use cavity type microwave resonators in order to obtain electromagnetic field that couple with the Rb gas. This type of design is relatively bulky, and not easily compatible with miniature atomic clocks, where most if not all elements are integrated on-chip.
For chip-scale atomic clocks new microwave resonator designs are needed. Some interesting alternative designs have been proposed, like the use of coils to generate a magnetic field in the microwave range [8]. Other designs include lumped LC resonators [15], helical resonators [16] or the so-called split-ring resonator [17].
Solutions such as the magnetron-type MWR [18], miniature MWR using lumped LC elements [14], or slotted-tube MWR [19] were developed for Rb cells down to ≈1 cm size, but only few microwave structures for mm-scale cells are reported, based on strip-lines or micro coupling loops [8].
In this work we propose a new miniature MWR (the μ-LGR, which will be described in detail in Chapter 5), for use with 36 mm^3 micro-fabricated Rb cells, like the one presented in [20].

4.4 Microwave Cavities

In this work we limit the scope of our analysis to cylindrical cavities obtained by sections of circular waveguides short-circuited at both ends, as the ones encountered in many atomic clock applications. In the following, we review some relevant theoretical aspects useful to understand the design choices presented in Chapter 5.
Inside closed structures like cavities (or resonators), only discrete solutions of Maxwell's equations can exist in absence of sources. A complete mathematical formulation for the analysis of these structures can be found in [21]. Here we recall the field expressions of the resonant modes that can possibly meet the requirements over the magnetic field distribution for the application considered, i.e. TE modes satisfying the cavity pec boundary condition (metallic wall) at both ends.
As seen in Section 2.7.2.3, circular waveguide modes satisfy the necessary boundary conditions on the circular waveguide wall. From Tab. 2.3, the transverse electric fields (E_ρ, E_ϕ) of the TE_{nm} (or TM_{nm}) circular waveguide mode can be written as

$$\bar{E}(\rho,\phi,z) = \bar{e}(\rho,\phi)[A^+ e^{-j\beta_{nm}z} + A^- e^{j\beta_{nm}z}], \tag{4.1}$$

where $\bar{e}(\rho,\phi)$ represent the transverse variation of the mode and A^+ and A^- are arbitrary amplitude of the forward and backward traveling waves. In order to satisfy the have pec boundary condition at the ends of the cavity, i.e. $\bar{E}_t = 0$ in $z = 0, d$ it must be $A^+ = -A^-$

and

$$A^{+} \sin \beta_{nm} d = 0, \tag{4.2}$$

or

$$\beta_{nm} d = l\pi, \qquad \text{for} \quad l = 0, 1, 2, 3..., \tag{4.3}$$

where d is the length of the cavity and β_{nm} is the propagation constant of the TE_{nm} mode from (2.42) (or (2.49) for the TM modes). Thus, the resonance frequency of the TE_{nml} mode is

$$f_{mnl} = \frac{c}{2\pi\sqrt{\mu_r \epsilon_r}} \sqrt{(\frac{\chi_{nm}}{a})^2 + (\frac{l\pi}{d})^2} \tag{4.4}$$

with $\chi_{nm} = p'_{nm}$ for TE modes (and $\chi_{nm} = p_{nm}$ for TM modes), a is the cavity radius and d the cavity length. The dominant TE mode is thus the TE_{111} mode, while the dominant TM mode is the TM_{110} mode.

4.4.1 EM parameters for Atomic Clocks

In this section, the EM parameter useful for the analysis of microwave cavities for atomic clocks applications are reviewed. Among these parameters, the resonant frequency and the Quality factor can be used to study resonators in general. The Filling Factor (FF) and the Field Orientation Factor (FOF) are specific parameters used for evaluating the magnetic field distribution of MWR for atomic clocks.

4.4.1.1 Resonant Frequency and Quality Factor

By imposing the boundary conditions for the geometry of the cavity, we obtain a set of discrete solutions, as previously explained (Section 4.4). The resonant frequencies can be written as in 4.4. In practice, the discrete number of resonances that are present inside a cavity suffer losses due to the presence of non-pec cavity walls with finite conductivity and dielectric loading. In order to take into account these losses the concept of Quality factor is used, for which the same definition is applicable that can be found in Section 2.7.2.1.
It can be demonstrated [22] that the Quality factor Q_m due to the finite conductivity of the cavity walls can be expressed in terms of the tangential component of the magnetic field H_t at the surface S of a lossless cavity wall and the skin depth δ:

$$Q_m = \frac{2}{\delta} \frac{\int_V H^2 dV}{\oint_S H_t^2 dS}. \tag{4.5}$$

The Quality factor Q_d due to lossy dielectric is defined as the ratio between the imaginary and the real part of the complex dielectric constant of the lossy dielectric, and is given by:

$$Q_d = \frac{1}{\tan \delta}. \tag{4.6}$$

For the calculation of the unloaded and external quality factor Q_u and Q_{ext}, the same considerations apply as from Section 2.7.2.1, where the term Q_{rad} can be neglected here.
Microwave cavities with appropriate loaded Quality factor Q_L are needed in all commercial rubidium clocks based on DR to enhance (and localize) the magnetic field amplitude B and optimize the power consumption. In fact, the Q_L can be written as:

$$Q_L = 2\pi f \frac{W}{P}, \tag{4.7}$$

where P is the power at the input to the cavity, and the electromagnetic energy W stored in a cavity with volume V_c is calculated from the relation:

$$W = \frac{V_c}{2\mu_0} B^2 \tag{4.8}$$

where μ_0 is the magnetic permeability of vacuum. The necessary power P to drive the microwave cavity is thus inversely proportional to Q_L.

4.4.1.2 Filling Factor

The homogeneity of intensity and orientation of the microwave field inside the MWR are essential to the performance of the atomic standard. To characterize the magnetic field distribution, a parameter widely used for atomic frequency standards is the Filling Factor (FF), defined as in [11]:

$$\eta = \frac{1}{V_{\text{cell}}} \frac{\left(\int_{V_{\text{cell}}} H_z dV\right)^2}{\int_{V_{\text{cavity}}} H^2 dV} \tag{4.9}$$

where V_{cell} is the volume occupied by Rb atoms, V_{cavity} is the total volume of the microwave cavity inside the shield, including the cell volume, and H_z is the component of the magnetic field along the axial direction: η is thus a measure of the part of magnetic field energy useful for the clock signal compared to the total microwave energy stored in the cavity.
It must be noticed that the FF is strongly dependent on the cavity geometry because it is normalized with respect to the total magnetic field. Thus, the FF will be very low when the ratio of Rb cell volume to cavity volume is small, as it is the case for the implementation considered in this work. For this reason, in the following section we introduce a different parameter, the FOF, that is used to better evaluate the magnetic field distribution.

4.4.1.3 Field Orientation Factor

The FOF, ξ, can be used as a figure of merit in order to evaluate the part of the magnetic field energy inside the Rb cell which is useful for the atomic clock signal, independently from the cavity geometry:

$$\xi = \frac{1}{V_{\text{cell}}} \frac{\left(\int_{V_{\text{cell}}} H_z dV\right)^2}{\int_{V_{\text{cell}}} H^2 dV} \tag{4.10}$$

where V_{cell} is the volume occupied by Rb atoms, and H_z is the component of the magnetic field along the direction of the C-field, z in our case. The magnetic energy stored in the component H_z should represent at least the 70% of the overall magnetic field energy, thus $\xi \geq 0.7$ is required.
In this way, for fixed cell dimensions, ξ can be used to compare the homogeneity of the relevant field direction inside the cell for different microwave cavities. The ideal value for an atomic clock would be $\xi = 1$, implying that the field is completely z-directed so that undesired σ Zeeman transitions are avoided [23].

4.4.2 Non-homogeneous Cavities

In atomic clock applications, a vapor cell normally made of dielectric material (like glass and silicon), is placed into the MWR, as shown in Section 4.3. The presence of dielectric perturbs the field distribution and changes the resonant frequency, as can be deduced by (4.4).
Due to the presence of a material discontinuity, the discrete set of solutions for the resonant frequencies corresponds to hybrid modes where both the E field and the H field have a z component. The only cases where pure TE and TM modes can exist are when $m = 0$ (no angular dependency) and at the cut-off frequency [24].
A method for the calculation of complex modes of propagation in dielectric-loaded circular structures is provided in [24, 25]. Such an analysis is not trivial and becomes even more complex in the presence of material discontinuities along the propagation direction, where other modes can be excited. As a general rule, special care must be put in the treatment of non-homogeneous cavities, in order to account for the presence of hybrid modes.

4.4.3 Cavity Perturbations

The principle of perturbation allows to find the solution of a *perturbed* electromagnetic problem, where some parameters such as the configuration of the boundaries, the material in the volume or the material in the boundary change slightly, once the solution of the *unperturbed* problem is known [22].
The formulations of the perturbation principle in the cases of disturbances by means of conducting or insulating objects introduced into the cavity [26, 27] can be advantageously used to produce an intentional variation (mechanical tuning) of the resonance frequency.

4.4.3.1 Cavity Wall Perturbation

The cavity wall perturbation consists in introducing a small deformation in the cavity wall, or a small conductive perturbing object into the cavity.
In can be shown [22] that the change in frequency due to this perturbation is approximately equal to

$$\frac{\Delta f}{f_0} \approx \frac{\int_{\Delta V}(\mu H_0^2 - \epsilon E_0^2)dV}{\int_V(\epsilon E_0^2 + \mu H_0^2)dV}. \tag{4.11}$$

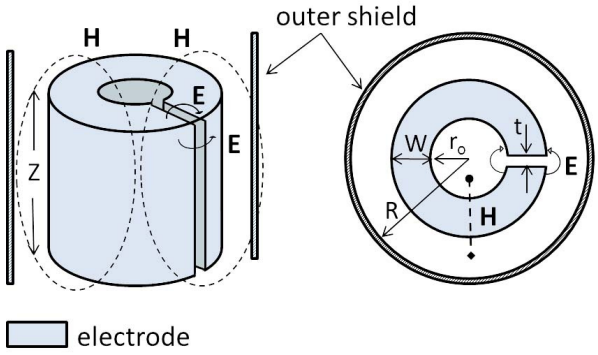

Figure 4.5: The loop-gap resonator perspective and top view, showing the principal components, inspired to [28].

In this formula, the denominator is proportional to the total energy stored in the cavity, whereas the numerator is proportional the electric and magnetic energies removed by the perturbation, so that 4.11 can be rewritten as

$$\frac{\Delta f}{f_0} \approx \frac{\Delta W_m - \Delta W_e}{W}, \tag{4.12}$$

where W is the total energy stored in the unperturbed cavity and ΔW_m and ΔW_e are the time average magnetic and electric energy, respectively, originally stored in the volume ΔV of the perturbing object.
The perturbation formula shows that an inward perturbation of the wall will cause the frequency to raise if it is operated at a point with large magnetic field (high W_m) and small electric field (low W_e), and will lower the frequency if it is operated at a point with large electric field (high W_e) and small magnetic field (low W_m).

4.4.3.2 Material Perturbation of a Cavity

The material perturbation of the cavity [27] takes place if an insulating object of volume ΔV with permittivity ϵ_r and permeability μ_r is introduced into the cavity, slightly changing the frequency of the cavity.
Different formulations of the material perturbation principle can be found in [22], for small variations $\Delta\epsilon_r$ and $\Delta\mu_r$, for $\Delta V \rightarrow V_{cavity}$ and others. In any case, the perturbation formula predicts that any increase in μ and ϵ can only decrease the frequency of the cavity, independently from whether the electric or magnetic field is perturbed.

4.5 The Loop-Gap Resonator

The Loop-Gap Resonator (LGR) [29], also referred to as split-ring resonator [17] or slotted tube cavity [30], can be represented, in its simplest model, by a lumped elements model, i.e. an LC circuit where the loop is an inductor and the gap is a capacitor.
The electric fields, as shown in Fig. 4.5, are supported by the gap with the magnetic fields surrounding the loop [28]. When the dimensions of the resonator are substantially smaller than the half-wavelength of the resonant microwave frequency, the lumped element model can be used and the electric and magnetic fields can be considered separated.
In a first order approximation represented by (4.13), the resonance frequency of the resonator is defined by the geometry of the electrode structure, including the radius (r_o), the thickness (w) and the length (Z) of the electrodes, the width (t) and number (n) of gaps, and the medium inside the shield (ε_r, μ_r):

$$C = \varepsilon_r \frac{wZ}{nt}, L = \mu_r \frac{\pi r_o^2}{Z} \;\rightarrow\; f = \frac{1}{2\pi\sqrt{LC}} \tag{4.13}$$

In order to take into account the fringing fields and the presence of the shield (see Fig. 4.5), correction terms must be added to the formula, so that the resonance frequency depends on the outer shield radius R, as in the expression derived in [17]. In [29], an experimental correction factor is added for the fringe electric fields. In all the calculation methods mentioned, the approximation of infinite length was used. The expression developed in [28, 31] comprises a correction factor for the effect of the limited length of the resonator, and it is expressed as

$$f = \underbrace{\frac{1}{2\pi}\sqrt{\frac{n}{\pi r_o^2 \varepsilon_r \mu_r}\frac{t}{w}}}_{LC}\underbrace{\sqrt{1+\frac{r_o^2}{R^2-(r_o+w)^2}}}_{\text{shield}}\underbrace{\sqrt{\frac{1+\frac{\Delta Z}{Z}}{1+\frac{\Delta w}{w}}}}_{\text{correction factor}} \tag{4.14}$$

Where r_o is the inner loop radius, Z is the length of the resonator, w is the gap width, t is the gap between the electrodes, and R is the shield radius, as in Fig. 4.5.
The parameter ΔZ is the equivalent length extension due to the magnetic fringe fields at the two ends of the resonator and Δw is the equivalent length extension of the gap width due to the gap electric fringe fields.
The values $\Delta Z \simeq 0.18R$ and $\Delta w \simeq 3t$, estimated in [28], lose accuracy when the gap t is large ($t/r_o > 0.2$). More general expressions for ΔZ and Δw are given in [31].

4.5.1 Usefulness of the Proposed Model

In order to evaluate the usefulness of the LGR model expressed by (4.14), theoretical predictions over different geometrical parameters of the LGR were compared with ANSYS HFSS simulations . Reference values $R = 6$, $r = 3$, $Z = 5$, $w = 0.5$ and $t = 2$ were varied, for fixed $n = 2$ and considering an $\varepsilon_r = 1$. Fig. 5.5(a)-(d) shows the comparison between the simulated results and the model computation, yielding good agreement.

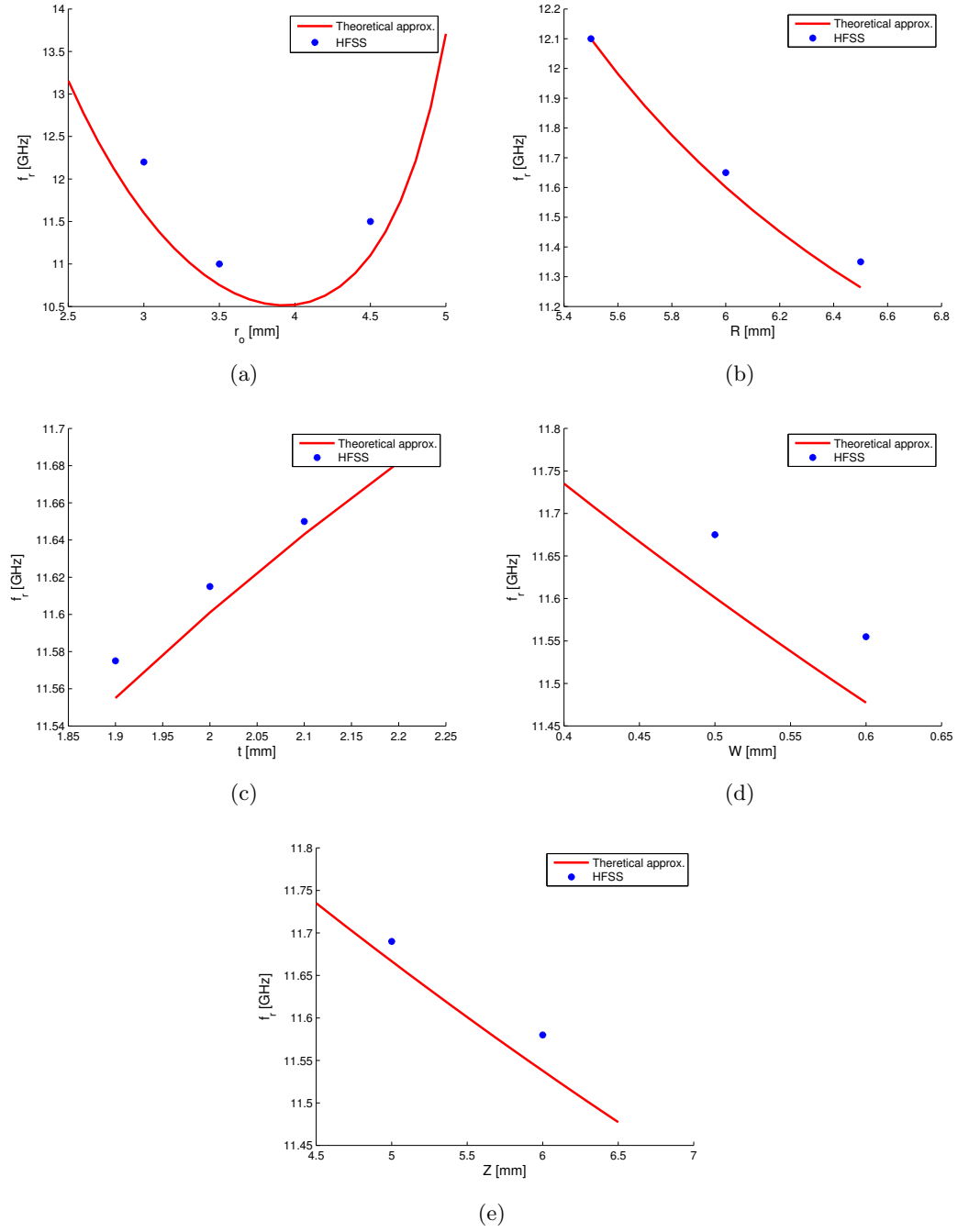

Figure 4.6: Comparison between HFSS simulations and the theoretical approximation for the resonance frequency f_r of the LGR. Variations of the reference values $R = 6$, $r = 3$, $Z = 5$, $w = 0.5$ and $t = 2$ ($n = 2$, $\varepsilon_r = 1$) are shown.

Thus, (4.14) can be considered as a useful frequency estimation in the design of a LGR cavity. The number of gaps, the loop radius and the gap dimensions (w and t) provide a reasonable freedom in the cavity design. The LGR is an interesting solution for Rb atomic clocks where, once a cell of fixed dimensions is given, a compact resonant cavity at 6.835 GHz is required.

4.5.2 Coupling and Tuning Methods

An LGR can be coupled to external circuits both by capacitive or inductive means.
In the first case a monopole probe is placed in proximity of the gap and it interacts with the gap fringe electric fields. In the latter case, an inductive loop can be used for coupling to the magnetic fields at either end of the resonator.
In order to correct for inevitable manufacturing tolerances, fine tuning of the resonant frequency can be electronic or mechanical. Various solutions can be found in literature, based on a varactor to control the capacitance of the gap [28], a tuning loop, a dielectric slab, a conductive plate [17] or a tuning screw [32].

Bibliography

[1] J. Camparo, "The rubidium atomic clock and basic research," *Physics Today*, pp. 33–39, Nov. 2007.

[2] S. Knappe, "MEMS atomic clocks," in *Comprehensive Microsystems*. Elsevier B.V., 2008, vol. 3.

[3] A. B. Sannigrahi, "Derivation of selection rules for magnetic dipole transitions," *Journal of Chemical Education*, vol. 59, n. 10, p. 819, 1982.

[4] J. Brossel and F. Bitter, "A new "double resonance" method for investigating atomic energy levels. application to hg^3p_1," *Physical Review*, vol. 86, n. 3, pp. 308-316, 1952.

[5] *SA.45s CSAC Chip Scale Atomic Clock datasheet*, Symmetricom Inc., San Jose CA, USA, document DS/SA.45s CSAC/123010/pdf, 2010.

[6] M. Pellaton, C. Affolderbach, Y. Pétremand, N. de Rooij, and G. Mileti, "Study of laser-pumped double-resonance clock signals using a microfabricated cell," *Physica Scripta*, vol. T149, 014013, 2012.

[7] R. Lutwak *et al.*, "The chip-scale atomic clock - coherent population trapping vs. conventional interrogation," *Proc. 34th Annual Precise Time and Time Interval (PTTI) Meeting*, pp. 1–12, Dec. 2002.

[8] A. M. Braun *et al.*, "RF-interrogated end-state chip-scale atomic clock," *Proc. 39th Annual Precise Time and Time Interval (PTTI) Meeting*, pp. 233–248, Nov. 2007.

[9] J. Vanier and C. Mandache, "The passive optically pumped Rb frequency standard: the laser approach," *Applied Physics B*, vol. 87, no. 4, pp. 565–593, 2007.

[10] C. Affolderbach and G. Mileti, "A compact laser head with high-frequency stability for rb atomic clocks and optical instrumentation," *Rev. Sci. Instrum.*, vol. 76, p. 073108, 2005.

[11] J. Vanier and C. Audoin, *The quantum physics of atomic frequency standards*. A. Hilger (Bristol and Philadelphia), 1989.

[12] J. Vanier, R. Kunski, P. Paulin, J. Savard, M. Tetu, and N. Cyr, "On the light shift and buffer gas shift in passive rubidium frequency standard," in *36th Annual Symposium on Frequency Control*, 1982, pp. 348–354.

[13] T. M. Kwon and H. E. Williams, "Us patent 4,495,478," 1985.

[14] J. Deng, "Subminiature microwave cavity for atomic frequency standards," *Proc. of IEEE International Frequency Control Symposium and PDA Exhibition*, pp. 85–88, 2001.

[15] H. E. Peter, *US patent 4,123,727*, 1978.

[16] G. Busca and L. Johnson, *US patent 4,947,137*, 1990.

[17] W. N. Hardy and L. A. Whitehead, "Split ring resonator for use in magnetic resonance from 200-2000 MHz," *Rev. Sci. Instrum.*, vol. 52(2), pp. 213–216, 1981.

[18] H. Schweda, G. Busca, and P. Rochat, "Atomic frequency standard," *European patent EP 0561261*, 1997.

[19] B. Xia, S. Zhong, D. An, and G. Mei, "Characteristics of a novel kind of miniature cell cavity assembly for rubidium frequency standards," *IEEE Trans. on Instrum. and Measurement*, vol. 55, pp. 1000–1005, 2006.

[20] Y. Pétremand, C. Affolderbach, R. Straessle, M. Pellaton, D. Briand, G. Mileti, and N. F. De Rooij, "Microfabricated rubidium vapour cell with a thick glass core for small-scale atomic clock applications," *J. Micromech. Microeng.*, vol. 22(2), 025013, 2012.

[21] R. E. Collin, *Foundations of Microwave Engineering*. 2nd ed., McGraw-Hill, Inc., 1992.

[22] K. Zhang and D. Li, *Electromagnetic Theory for Microwaves and Optoelectronics*. 2nd ed., Springer, Inc., 2007.

[23] E. Arimondo, M. Inguscio, and P. Violino, "Experimental determinations of the hyperfine structure in the alkali atoms," *Rev. Mod. Phys.*, vol. 49, pp. 31–75, Jan. 1977.

[24] T. Sphicopoulos, L.-G. Bernier, and F. E. Gardiol, "Theoretical analysis for the design of a compact circular cavity with empty core," in *14th European Microwave Conference*, Sept. 1984, pp. 329 –334.

[25] P. Clarricoats and K. Slinn, "Complex modes of propagation in dielectric-loaded circular waveguide," *Electronics Letters*, vol. 1, no. 5, pp. 145 –146, Jul. 1965.

[26] R. F. Harrington, *Time-harmonic electromagnetic fields*. McGraw-Hill, 1961.

[27] J. C. Slater, *Microwave Electronics*. D. Van Nostrand Company, Inc., 1950.

[28] M. Mehdizadeh, T. Ishii, J. Hyde, and W. Froncisz, "Loop-gap resonator: a lumped mode midrowave resonant structure," *IEEE Trans. Microw. Theory Tech.*, vol. 31, pp. 1059–1064, 1983.

[29] W. Froncisz and J. S. Hyde, "The loop-gap resonator: a new microwave lumped circuit ESR sample structure," *J. Magn. Reson.*, vol. 47, pp. 515–521, 1982.

[30] T. Sphicopoulos and F. Gardiol, "Slotted tube cavity: a compact resonator with empty core," *IEE Proceedings*, vol. 134, no. 5, pp. 405–410, 1987.

[31] M. Mehdizadeh, "An investigation on electromagnetic fields and properties of the loop-gap resonator, a lumped mode microwave resonant structure," *Ph.D. Thesis, Marquette University*, 1983.

[32] G. Mei, D. Zhong, S. An, J. Liu, and X. Huang, "Miniaturized microwave cavity for atomic frequency standard," *US Patent 6,225,870 B1*, May 1, 2001.

5 Miniature MWR Solutions for Rubidium Atomic Clocks

5.1 Outline of the Chapter

In this chapter we propose different solutions for the MWR in miniature laser-pumped DR Rubidium atomic clocks, using micro-fabricated alkali vapor cells filled with buffer gas.
In the initial part of the chapter, we investigate a new compact MWR solution suitable for the integration of glass-silicon 3D cells as those presented in [1]. We present the performed studies that led to the conception of a novel MWR design based on a miniature multi-layered printed LGR structure, that is referred to as the μ-LGR in its optimized version for prototyping [2]. Then, an overview on the tests performed on prototypes, which included microwave characterization and tuning with a VNA at room temperature and in the presence of a temperature change from $\sim 20°C$ to $100°C$, will be given. Finally, the DR signal and the state-of-the-art results on stability obtained with 3D cell integrated into the μ-LGR will be presented to prove the potential of the newly patented μ-LGR [3, 4] for integration in miniature Rubidium atomic clocks.
In the latter part of the chapter, we introduce a possible investigated solution for micro-fabricated 2D cells with outer dimensions of 7x4x3 mm. The proposed solution consists of a planar resonator printed on a dielectric substrate [5], that represents a promising candidate for new miniature MWR designs, as shown by simulated studies.

5.2 First Proposed Solutions for the Miniaturized MWR

The LGR structure previously presented in Chapter 4, was selected as a possible means to achieve a very compact MWR design. Standard cavity resonators have excellent Quality factors but the Filling Factors become rather low for reasonably sized vapor cells, and in addition the cavity may be simply too large for the space available [6].
A further point is that the RF fields in standard hollow cavities are necessarily inhomogeneous and therefore high homogeneity is only obtained by restricting the size of the cell.
The LGR type of resonator has a high field homogeneity (as it will be also confirmed by experimental results in Section 5.2.2), a Filling Factor of a solenoid and very high Q. It is also of easy fabrication, which is an additional advantage in view of a possible batch fabrication of manufactured prototypes.

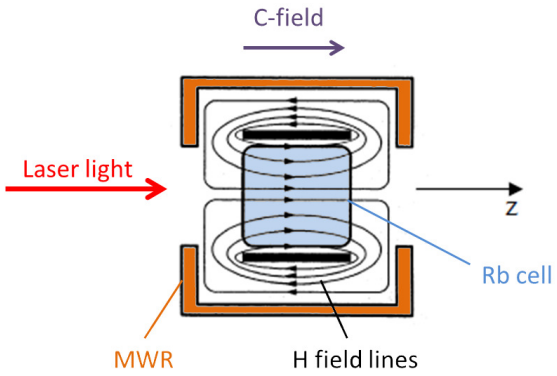

Figure 5.1: Geometry of the microwave magnetic field lines in a magnetron-type resonator (of the type used at LTF in Rb atomic clocks) using a 1 cm^3 Rb cell.

5.2.1 MW Specifications

For the specific application considered, guidelines values were provided with respect to the following parameters:

- **Field orientation:** the pump light beam sent through the cell travels along the C-field direction, i.e. the z-axis, as sketched in Fig. 5.1. In order to observe the clock resonance, both the static magnetic C-field and the magnetic component of the microwave field also have to be parallel to the z-axis, at least over the volume of the Rb cell,

- **Field homogeneity (orientation):** the part of the magnetic field energy inside the Rb cell which is useful for the atomic clock signal is evaluated through the FOF (as defined in Section 4.4.1.3), which should be > 0.7 according to previous experimental estimations made at LTF using magnetron-like cavities like the one shown in Fig. 5.1.

- **Field homogeneity (amplitude):** inhomogeneity of the microwave magnetic field amplitude will cause different power-shifts of the clock transition at different points inside the cell volume. In a buffer-gas cell this will cause inhomogeneous broadening of the observed resonance line. However, at the typical levels of microwave power applied in Rb cell clocks, the power shifts are on the order of 10 Hz, negligible with respect to a total linewidth around 1 kHz.

- **Rb cell:** The micro-fabricated vapor Rb cell conceived and manufactured by SAMLAB-LTF [1] consists of a stack of Pyrex glass and bonding silicon layers with cuboidal shape and dimensions of 6x6x5.05 mm. It is shown in Fig. 5.2 in its initial design that was minimally modified by chamfering its edges, in order to make the realization of the of the μ-LGR stack feasible.

- **Filling Factor:** as seen in Section 4.4.1.2 the FF is a parameter commonly used for atomic clocks. For a magnetron-type resonator cavity, typically a value of $\eta = 0.3$ is

found for the passive maser [7].
However, the FF highly depends on the cavity geometry (as discussed in Section 4.4.1.2) and the use of a different figure of merit, i.e. the FOF is thus desirable.

- **Quality factor:** as long as the required microwave field amplitude can be met, a moderate-to-low Q of < 200 is desirable. This will help to avoid frequency drifts arising from cavity pulling [8], but this effect is not expected to be a limiting factor in a miniature atomic clock.

- **Microwave field amplitude:** an amplitude of the magnetic flux field of $B = 10^{-8}$ T is optimum for double-resonance spectroscopy, as explained more in detail in [9, Ch. 7]. For simplicity, this value can be taken as the average value of B.

- **Power input and Power loss:** for the LTF magnetron resonator, typical obtained values are a P_{in} on the μW level and $P_{loss} \approx 50$ nW.
Experimentally, useful signals are typically obtained with a magnetron resonator at input power levels on the order of -40dBm to -30dBm thus roughly one order of magnitude higher than calculated.
The microwave power absorbed by the Rb atoms can be calculated from the microwave photon absorption rate: $R_{photon} = 1000$/second. Combining with the microwave photon energy one obtains the energy absorption rate per atom: $R_{atom} = 4.5\text{x}10^{-21}$ W. At typical cell temperature around 80°C, that is required to maintain the atoms in equilibrium with the liquid phase and at a sufficient density for observation of the atomic resonance [10], one finds the Rb vapor pressure $p_{Rb} = 2\text{x}10^{-5}$Pa, equivalent to $5\text{x}10^{-12}$ atoms/mm^3.
The microwave power absorbed per cell volume by the atoms is thus: 2.5 pW/mm^3.

- **Volume of the cell:** the cell should be as compact as possible to allow for reducing the package dimensions of the atomic clock. A cavity volume $V_c \sim 1cm^3$, similar to the ones of other existing MWR was taken as a reference value.

5.2.2 Parametric Studies

The simple LGR design shown in Fig. 5.3 was used as a reference model for simulations, with the dimensions listed in Table 5.1. The presence of a simplified cylindrical cell model (with Pyrex glass walls, $\varepsilon_r = 4.5$) with two different dimensions is considered. The cell size has significant impact on the FF of the LGR: the value of the FF is approaching the "theoretical" desired value of 0.3, while is reduced to a half when the cell dimensions are smaller, confirming the remarks done in Section 4.4.1.2 and the need of a different figure of merit (i.e. the FOF). Fig. 5.4 shows the magnetic field distribution inside the LGR with a big cell (a) and a small cell (b), showing comparable field homogeneity.

The proposed solution was validated through ANSYS HFSS software simulation. In order to achieve the compact printed μ-LGR from the simpler $n = 2$ LGR, the structure was optimized

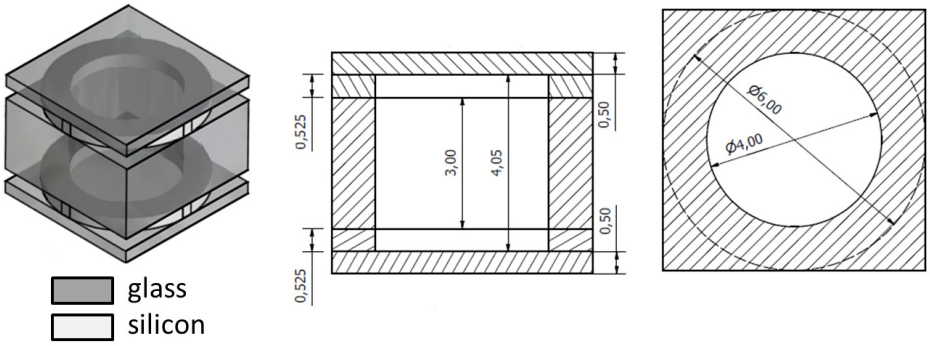

Figure 5.2: The SAMLAB-LTF 3D micro-fabricated cell.

Description	Parameter	Value [mm]		HFSS Simulations f_r	Q_0	FF
LGR inner radius	r	3	no cell	7.813	300	-
cell inner radius	r_{cell}	2.25				
LGR shield radius	R	6	big cell (6∅x10 mm)	6.450	315	0.28
LGR thickness	w	1				
LGR gap	t	0.5	small cell (6∅x5.05 mm)	6.890	427	0.14
LGR height	Z	6				
cell walls thickness	t_{cell}	0.75				

Table 5.1: Simple LGR (n= 2) with and without cell - summary of the simulated dimensions.

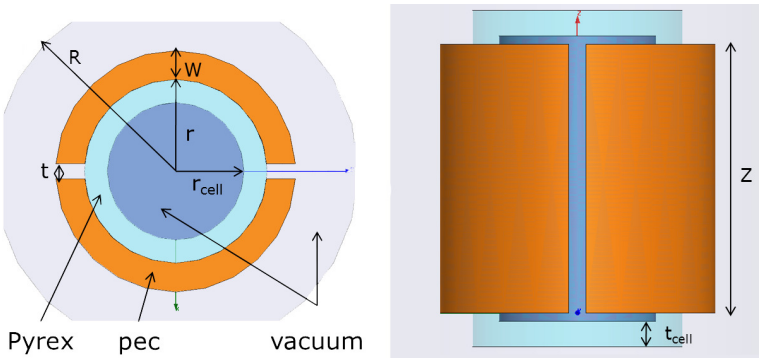

Figure 5.3: Simple simulated LGR model ($n = 2$).

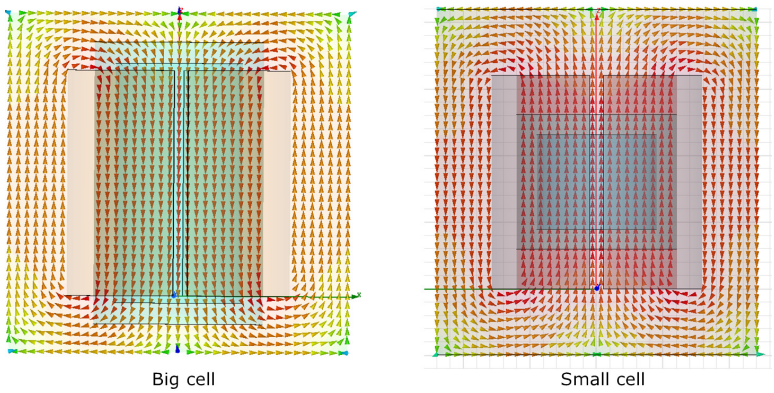

Figure 5.4: Magnetic field distribution inside the LGR with a big cell (a) and a small cell (b).

in several steps taking into account the Rb cell presence.
In particular, the influence of gap size (t) and width of electrodes (w) were investigated in order to get the desired resonance frequency.
As an example, Fig. 5.5(a) shows the simulated reflection coefficient for three different values of the gap size. The resonance shifts to higher frequencies as both L and C decrease, while the matching is also affected when t becomes too large.
Also, the influence of cavity apertures and dielectric properties of different materials were studied in order to determine a package suitable for manufacturing.
Finally the influence of tuning screws was considered during the optimization of the electrodes structure, given their strong impact on both magnetic and electric fields.
For $t = 2.0$ mm, the magnetic field at resonance has the desired TE mode distribution shown in Fig.5.5(b), with $\xi > 0.8$.

5.3 Optimized Solution: the μ-LGR

After optimization in terms of geometry and selection of materials, the μ-LGR has the following characteristics:

- the 3D micro-fabricated Rb cell (6x6x5.05 mm) is positioned inside the LGR resonator stack,
- the resonator comprises a multi-layered structure of 4 conductive electrodes ($w = 0.5$ mm, thickness 34 μm) separated by 3 cylindrical dielectric layers, stacked along the axial direction (z). The conductive electrodes are two-dimensional structures, formed by patterns of metal film printed onto the dielectric layers,
- the dielectric layers, have different thicknesses, in order to fit the cell height so that the occupied volume is minimized.

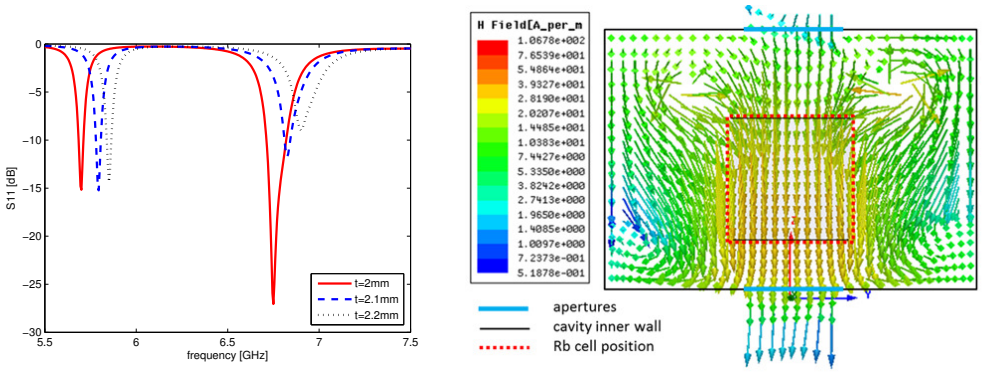

(a) (b)

Figure 5.5: (a) Influence of gap size t on reflection coefficient. Resonance of interest is at 6.835 GHz (right), while the resonance at ∼5.8 GHz (left) is a TM mode due to the cavity size, (b) simulated magnetic field of the TE mode at 6.835GHz ($t = 2.0$mm). The dotted red square indicates the position of the micro-fabricated Rb vapor cell.

In particular, the bottom and top layer are 1.524 mm-thick, while the central layer is 1.905 mm-thick, with a total resonator height of ∼5 mm. The 3 dielectric layers are made of the same material,

- the dielectric material composing the resonator layers is Rogers TMM® 3 ($\varepsilon_r = 3.27$, [11]), which has a temperature-compensated dielectric constant in the microwave region,

- the electrodes are planar realizations of loop gap resonators, juxtaposed in pairs in order to obtain a series of stacked loops with 2 gaps ($n = 2$) on each layer. The different layers of the electrode structure are electrically connected by means of metallized vias, but not in electrical contact with the outer metal enclosure,

- the shape of the electrodes and of the center openings in the supporting substrates is adjusted to fit the available vapor cell geometry.

- coupling to the microwave excitation is achieved by a loop-shaped strip-line fed by a 1.20 mm-coaxial line (semirigid EZ_47_CU_TP H+S [12]). The excitation loop is printed onto an additional thin dielectric layer, placed above the loop-gap multi-layered structure,

- a metal outer shield consisting of a cylindrical brass box is placed around the multi-layer resonator structure, the coupling device and the Rb cell. The metal box is in contact with the outer jacket of the 1.20 mm-coaxial line and detached from the other parts of the cavity by means of 2 spacing washers. The metal enclosure has 3 mm-diameter apertures at its ends to allow for the laser beam to interact with the Rubidium atoms vapor,

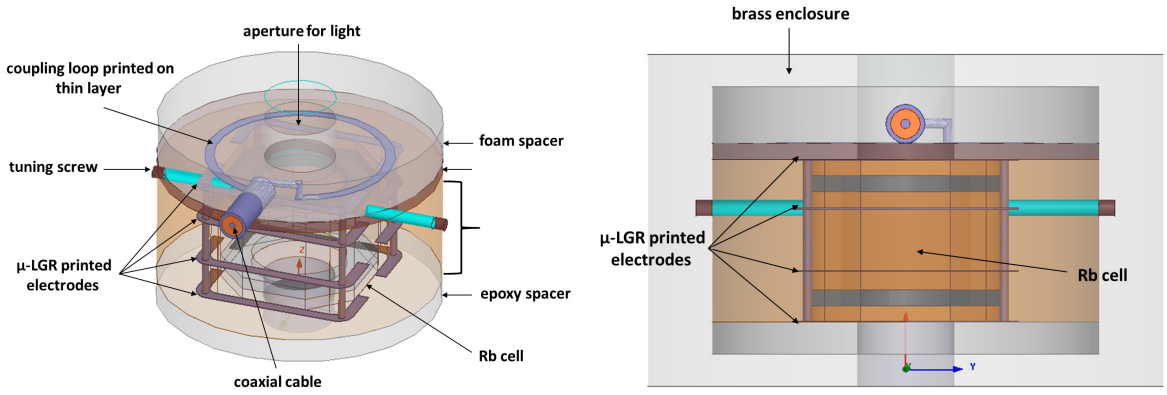

(a) (b)

Figure 5.6: (a) 3D view of the cavity stack (the brass enclosure is not shown for simplicity), (b) side view of the cavity stack.

- the two spacing washers are placed above the coupling structure and below the resonator stack bottom. The above spacer (1.67 mm thick) is made of Rohacell® thick foam ($\varepsilon_r = 1.06$, [13]), the bottom spacer (1 mm-thick) is made of FR 4 Epoxy $\varepsilon_r = 4.4$),
- adjustment of coupling can be done by changing the elevation of the excitation layer by means of thin dielectric spacers made of Pyralux® AP ($\varepsilon_r = 3.2$, [14]),
- the fine tuning of the resonance frequency is obtained by two 5 mm-long M1.6 tuning screws with thinner ends of 0.5 mm diameter, introduced into the cavity and manually controllable from the outside of the metal shield. The tips of the metal screws are able to perturb the electric field concentrated in the gap. Similarly, other solutions can be found in literature, based on a single tuning screw [15], a dielectric slab, or a conductive plate [6].

The 3 electrode layers composing the loop-gap resonator, the coupling layer and the spacing layers have shapes and dimensions that allow stacking them inside the metal shield in a precise and repeatable position without the use of adhesives, that would add a source of uncertainty to the cavity performance.
Thanks to this, the structure is fully demountable in case the vapor cell or other parts of the cavity need to be removed or changed. Fig. 5.6 shows the simulated model of the complete stack (the outer brass enclosure is not shown for simplicity). Table 5.3 provides a summary of the structure dimensions and the characteristics of the materials used.

5.4 Measurements on Prototypes

Several prototypes based on the μ-LGR optimized solution were built, as shown in Fig. 5.9. Considering the influence of the gap width on resonance frequency, the prototypes present

Part	**Material**	**Description**	**Parameter**	**Value**
bottom spacer	FR 4 Epoxy	diameter	d	12
		height	h_{Epoxy}	1
		hole diameter	d_{hole}	3
		permittivity	$\varepsilon_{r_{Epoxy}}$	4.4
		loss tangent	$\tan\delta$	0.02
μ-LGR dielectric stack	Rogers TMM3	diameter	d	12
		total height	h_{TMM}	5
		square hole side	s_{cell}	6
		permittivity	$\varepsilon_{r_{TMM}}$	3.27
		loss tangent	$\tan\delta_{TMM}$	0.002
electrodes	copper	layer width	w	0.5
		layer thickness	h_{metal}	0.034
		inner side	s_{cell}	6
		gap width	t	1.9-2.3
		diameter vias	r_{metal}	0.15
		conductivity	σ_{CU}	5.96x10^7 [S/m]
coupling spacers	Pyralux AP	diameter	d	12
		thickness(x1)	t_{PyAP}	0.025
		total height(x20)	h_{PyAP}	0.5
		permittivity	$\varepsilon_{r_{PyAP}}$	3.2
		loss tangent	$\tan\delta_{PyAP}$	0.003
coupling loop	copper	metal width	W	0.5
		metal thickness	h_{metal}	0.034
		inner diameter	d_{loop}	7
		conductivity	σ_{CU}	5.96x10^7 [S/m]
top spacer	Rohacell	diameter	d	12
		height	h_{foam}	1.775
		hole diameter	d_{hole}	3
		permittivity	$\varepsilon_{r_{foam}}$	1.06
		loss tangent	$\tan\delta$	0.0008
brass box	brass	inner diameter	d	12
		outer diameter	D	18-20
		apertures diam.	d_{hole}	3
		caps thickness	t_{cap}	1
		conductivity	σ_{brass}	1.59x10^7 [S/m]

Table 5.2: μ-LGR cavity - summary of the optimized dimensions and materials (dimensions are given in mm).

(a) (b) (c) (d) (e)

Figure 5.7: (a) Some of the built prototypes, (b) manufactured layers for the cavity stack, (c) the μ-LGR showing the holes for the tuning screws (inset show one of the 5-mm long tuning screws), (d) assembled μ-LGR (the outer diameter is 12 mm) containing the miniature Rb cell (e) brass enclosure: the feeding coaxial, one of the cavity apertures and one of the tuning screws are visible.

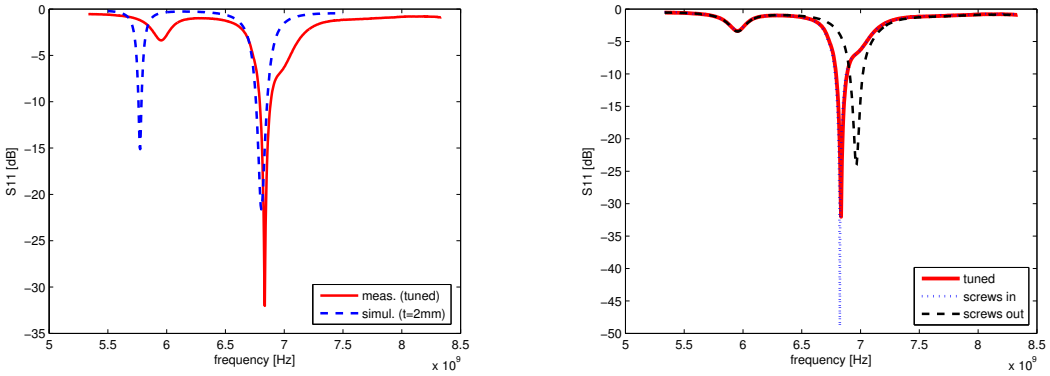

(a) (b)

Figure 5.8: (a) Comparison between the reflection coefficient of one measured prototype (t = 2.0 mm, tuned) and simulation of model t = 2.0 mm with maximum insertion of the two screws. Frequency is higher in the measured prototype due to the presence of air inside the cavity, (b) tuning of the μ-LGR prototype (t = 2.0 mm) at 6.835 GHz.

different values of t (from 1.9 to 2.3 mm, with a step of 0.1 mm). The built resonators were measured and tuned using a VNA (Agilent 8720D). The magnitude of the reflection coefficient $|S_{11}|$ at the coaxial cable port was monitored during the tuning process. In Fig. 5.8(a) the simulated model of one of the prototypes (t = 2.0 mm) is compared to the equivalent measured resonator. Results show good agreement and the small frequency shift is due to the presence of air inside the real assembled device. Loaded quality factor Q_L is $\simeq$26.

The two tuning screws were proven to be an efficient means to achieve the desired Rb resonance frequency at 6.835 GHz. The average tuning capability is 140 MHz for the built prototypes. The tuning of one prototype (t = 2.0 mm) is shown in Fig. 5.8(b).
A comparison of the results obtained by simulations and measurements on prototypes is given in Table 5.3.

	f_r screws in [GHz]		f_r screws out [GHz]			
Prototype	HFSS	Meas.	HFSS	Meas.	tuning range [MHz]	Q_L
t = 1.9	6.700	6.778	6.815	6.891	113	30
t = 2.0	6.715	6.811	6.805	6.943	132	26
t = 2.1	6.745	6.824	6.830	7.016	192	23
t = 2.2	6.770	6.815	6.860	6.937	122	26
t = 2.3	6.785	6.830	6.910	6.975	145	26

Table 5.3: μ-LGR, comparison between HFSS simulations and measured prototypes.

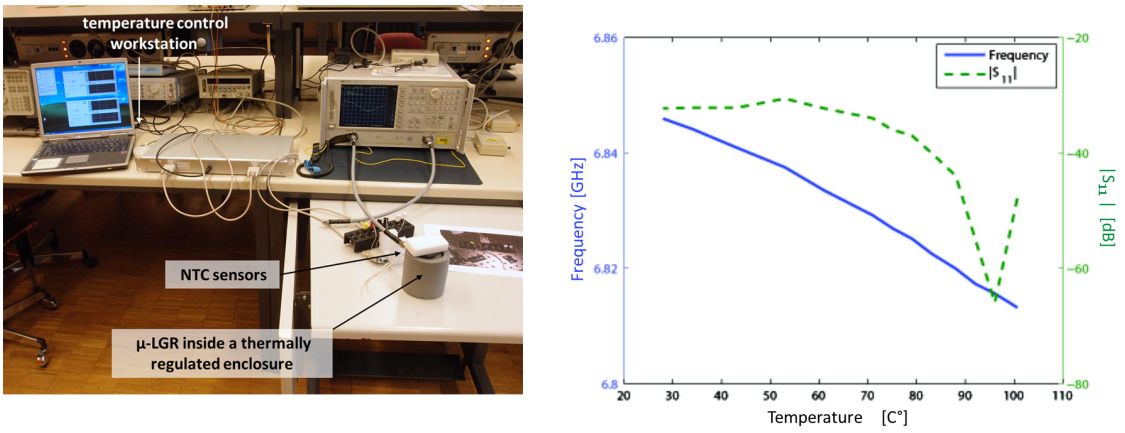

(a) (b)

Figure 5.9: (a) Test bed used for the measurement of the μ-LGR reflection coefficient vs. temperature, (b) results showing the influence of a temperature change from 20° to 100° on the $|S_{11}|$.

5.4.1 Temperature Influence

The influence of temperature on the resonance frequency of the μ-LGR cavity was investigated by means of the test bed shown in Fig. 5.9(a). The heating of the cavity was realized with a resistive wire and the temperature was recorded with NTC sensors. A temperature from 20°C to 100°Cwas applied to the cavity, in order to evaluate its impact on the performance of the atomic clock at the temperature of operation of 80°C.
Results show an overall frequency shift of $\sim$ 30 MHz which can be corrected for by means of the tuning screws. The reflection coefficient remains $\leq$-30 dB, as shown in Fig. 5.9(b).

5.5 Spectroscopic Results

In order to verify the suitability of the proposed solution, a Double Resonance experiment of the entire Physics Package integrating the μ-LGR cavity and the 3D micro-fabricated cell has been performed.
In Fig. 5.10 the experimental setup is shown. The Physics Package integrating μ-LGR cavity with the 3D Rb cell is visible. The main parts of the system are:

- **the vertical-cavity surface emitting laser (VCSEL) module**, stabilized at the D_2 line of ^{87}Rb and used for the optical pumping of the system,
- **the photodetector**, consisting of a photoresistor with an input impedance of 1kΩ, was used to detect the signal. In general, the higher is the resistance of the photodetector, the better is the precision of the acquired signal but more noise is added to the system,
- **optical elements**, like mirrors and lenses are used to guide the laser beam into the

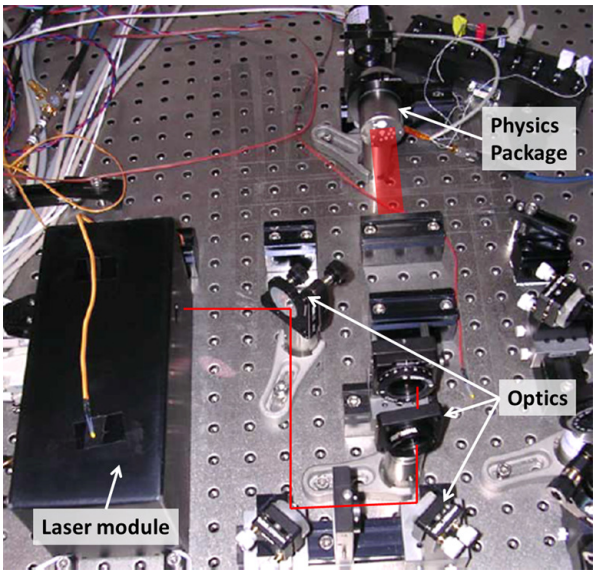

Figure 5.10: Double Resonance experiment setup

physics package. In addition, a polarizer is used to control the polarization and the intensity of the laser beam,

- **the Physics Package**, which contains the μ-LGR cavity with the Rb cell, two C-field coils, the heaters, the magnetic shields, and NTC sensors for temperature monitoring, as shown in Fig. 5.16. The cavity and the cell are heated at around 80°C. This temperature is set in order to have a good output signal and was previously determined by UNINE on the basis of experimental factors that take especially into account the characteristics of the buffer gas inside the vapor cell. The applied C-field was fixed to 8 μT,
- **an electronic control unit** stabilizes the cell temperature and allows to control the input current to generate the C-field,
- **a microwave synthesizer** with attenuators provides the RF power to the microwave cavity through the coaxial cable,
- **oscilloscopes** monitor the output signal,
- **a workstation** allows to drive and record the parameters of the experiment by software control.

5.5.1 Double Resonance Signal

The combination of the μ-LGR and the 3D-cell gave rise to a clock signal with a contrast of more than 12% and a linewidth of 5.6 kHz (see Fig. 5.12), as well as a figure of merit (FoM)

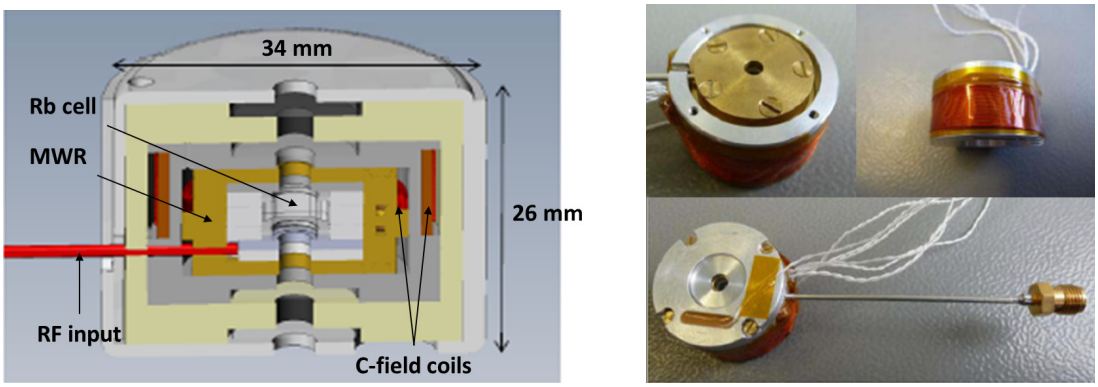

(a) (b)

Figure 5.11: (a) 3D cut view and (b) different views of the PP prototype containing the μ-LGR cavity with the Rb cell, two C-field coils, the heaters, the magnetic shields, and NTC sensors for temperature monitoring.

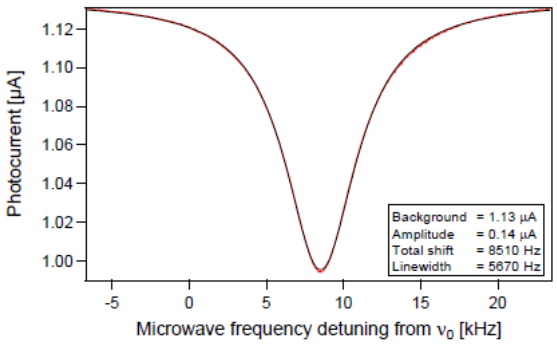

Figure 5.12: DR signal with the μ-LGR and the 3D cell.

of 20, (as defined in [16] as 106 Hz·contrast/linewidth [Hz]) and a discriminator slope of 23 pA/Hz [17].

5.5.2 Zeeman Transitions

This spectroscopic measurement allows a qualitative interpretation of the FOF inside the μ-LGR. In order to retrieve the spectrum showed in Fig. 5.13, the microwave frequency is swept all over the allowed magnetic transitions of the ^{87}Rb. As discussed in Chapter 3, two distinct magnetic transitions transitions are allowed: $\pi-$ and $\sigma-$ transitions, which are a direct consequence of the longitudinal and the transverse MW field, respectively.
Since $\sigma-$transitions are clearly visible on the figure, but smaller than the $\pi-$transition, it can be deduced that the FOF is well within the required values (FOF > 0.7). The "chair" patterns present in some of the $\sigma-$transitions are due to inhomogeneities in the C-field strength inside the cell.

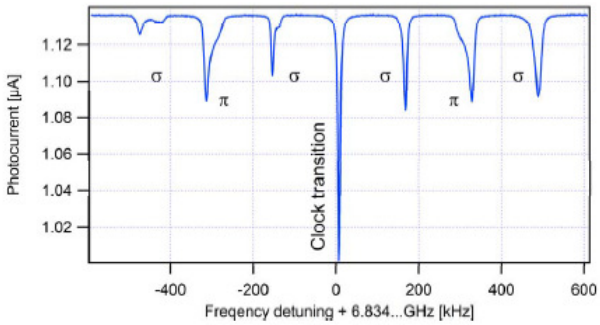

Figure 5.13: Zeeman lines with the μ-LGR and the 3D cell.

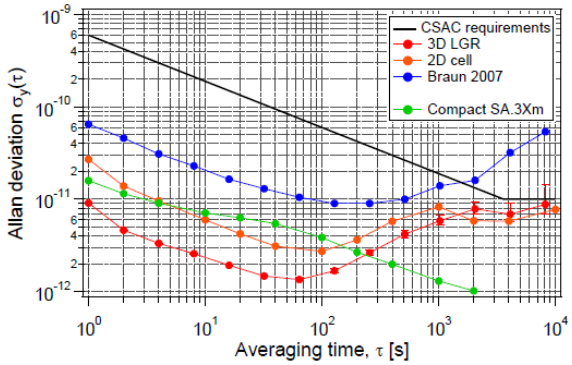

Figure 5.14: Atomic clock short-term stability with the μ-LGR and the 3D cell.

5.5.3 Stability

The S/N limited short-term stability is estimated around $6.6\text{x}10^{-12}$ at 1 s. The measured short-term stability is $7.1\text{x}10^{-12}\tau^{-1/2}$ (1-100 s). This short-term stability is better than the best other clocks using microfabricated cells [18–20], as shown in Fig. 5.14.
The medium- to long-term clock stability is currently limited by a relatively strong intensity-light-shift coefficient of the cell ($2.6\text{x}10^{-10}$/%) inducing a substantial temperature sensitivity (of $1.1\text{x}10^{-9}$/K) [17].

5.6 Miniature Planar Resonator for 2D Microfabricated cells

The planar MWR presented in this section was proposed for the integration of 2D Rubidium cells of dimensions of 7x4x3 mm, as shown in Fig. 5.15. This cell design geometry was not fully optimized for microfabrication, but it served as a reference cell to imagine suitable MWR solutions. The material considered for fabrication are pyrex and silicon.
The proposed MWR solution consists of a planar coil with integrated tuning elements [5] (see Fig. 5.16(a)). Such structure has the advantage of being completely 2D and can be

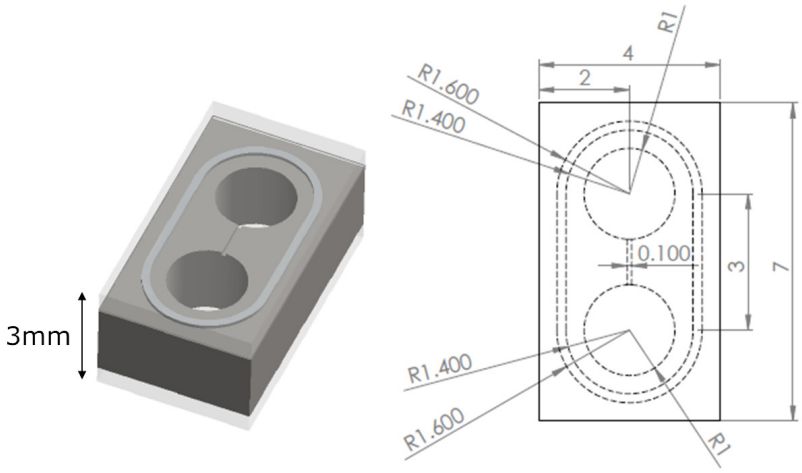

Figure 5.15: Perspective and schematics of the 2D cell in its preliminary design.

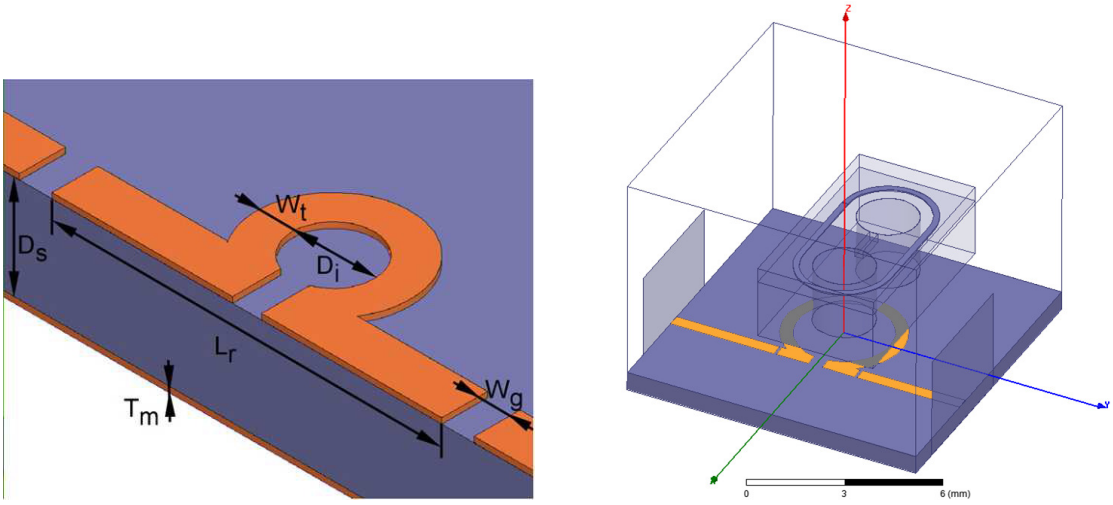

(a) (b)

Figure 5.16: (a) Cross section of the microstrip resonator with an incorporated coil, as in [5], (b) simulated resonator model with the 2D cell and a substrate of 10x10 mm ($\varepsilon_r = 2.2$).

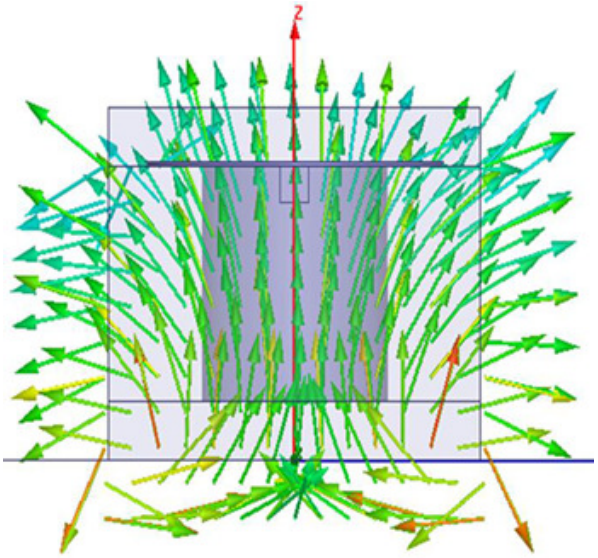

Figure 5.17: Magnetic field distribution of the planar resonator with the 2D cell, at 6.83 GHz.

thus easily manufactured using standard microtechnology. It may also represent an ideal candidate in case a possible on-chip integration of the physics package is envisaged. The planar resonator is composed of two parallel capacitors (the gaps) with an LC resonator (the microstrip coil) in between. The resonant frequency is thus given by the coil according to the relation $f_r = 1/(2\pi\sqrt{LC})$. The gaps on both sides of the resonator may be used to tune the Quality factor and the resonance depth.
The simulated parametric studies of the planar MWR gave encouraging results for further investigations, as demonstrated by the values of Table 5.4. Parameter notations are the same as in Fig. 5.16(a) (the simulated resonator model with the 2D cell is depicted in Fig. 5.16(b)). Fig. 5.17 shows the magnetic field distribution at 6.83 GHz, which yields a FOF=0.86.

Parameter	**Value [mm]**	$\lvert S_{11}\rvert$ **[dB]**	f_r **[GHz]**	**FOF**
W_t	0.5			
D_i	4			
W_g	0.3	-14.9	6.83	0.86
L_r	2.5			
D_s	0.635			

Table 5.4: Planar resonator with 2D cell

Bibliography

[1] Y. Pétremand, C. Affolderbach, R. Straessle, M. Pellaton, D. Briand, G. Mileti, and N. F. De Rooij, "Microfabricated rubidium vapour cell with a thick glass core for small-scale atomic clock applications," *J. Micromech. Microeng.*, vol. 22(2), 025013, 2012.

[2] M. Violetti, C. Affolderbach, F. Merli, M. G. Zürcher, and A. K. Skrivervik, "Miniaturized microwave cavity for rubidium atomic frequency standards," in *to be presented to European Microwave Week (EuMW)*, Oct. 28–Nov. 2 Amsterdam RAI, The Netherlands, 2012.

[3] M. Violetti, C. Afforderbach, F. Merli, G. Mileti, and A. K. Skrivervik, "Microwave resonator, quantum sensor, and atomic clock," *European Patent Application No. 12155696*, February 16, 2012.

[4] M. Violetti, M. Pellaton, C. Affolderbach, F. Merli, M. G. Zürcher, and A. K. Skrivervik, "New miniaturized microwave cavity for rubidium atomic clocks," *to be presented to IEEE Sensors Conference*, Oct. 28–31, 2012, Taipei, Taiwan.

[5] R. Narkowicz, D. Suter, and R. Stonies, "Planar microresonators for epr experiments," *Journal of Magnetic Resonance*, 175 (2005) 275–284.

[6] W. N. Hardy and L. A. Whitehead, "Split ring resonator for use in magnetic resonance from 200-2000 MHz," *Rev. Sci. Instrum.*, vol. 52(2), pp. 213–216, 1981.

[7] H. Schweda, *Private communication.*

[8] J. Viennet, C. Audoin, and M. Desaintfuscien, "Discussion of cavity pulling in passive frequency standards," *25th Annual Symposium on Frequency Control*, pp. 337–342, 1971.

[9] J. Vanier and C. Audoin, *The quantum physics of atomic frequency standards.* A. Hilger (Bristol and Philadelphia), 1989.

[10] J. Kitching, "Chip-scale atomic clocks at NIST," *NCSL International Workshop and Symposium*, Washington, USA, 2005.

[11] Rogers Corporation. [Online]. Available: http://www.rogerscorp.com/

[12] Huber+Suhner. [Online]. Available: http://www.hubersuhner.com

[13] Rohacell, Evonik Industries. [Online]. Available: http://www.rohacell.com/

[14] Pyralux, DuPont. [Online]. Available: http://www.dupont.com/

[15] G. Mei, D. Zhong, S. An, J. Liu, and X. Huang, "Miniaturized microwave cavity for atomic frequency standard," *US Patent 6,225,870 B1*, May 1, 2001.

[16] J. Deng, P. Vlitas, D. Taylor, L. Perletz, and R. Lutwak, "A commercial CPT rubidium clock," *in Proc. of 22nd EFTF*, Toulouse, 2008.

[17] T. Bandi, M. Pellaton, D. Miletic, C. Affolderbach, F. Gruet, R. Matthey, G. Mileti, C. Stefanucci, M. Violetti, F. Merli, J.-F. Zürcher, and A. K. Skrivervik, "Double resonance in alkali vapor cells for high performance and miniature atomic clocks," in *Proc. IEEE International Frequency Control Symposium, IFCS*, May 21–24, Baltimore, MD, USA 2012.

[18] R. Lutwak *et al.*, "The chip-scale atomic clock - prototype evaluation," *in Proc. of 21st EFTF*, Geneva, 2007.

[19] R. Boudot *et al.*, "Characterization of compact CS CPT clocks based on a Cs-Ne microfacricated cell," *in Proc. of 26st EFTF*, Göteborg, 2012.

[20] A. M. Braun *et al.*, "RF-interrogated end-state chip-scale atomic clock," *Proc. 39th Annual Precise Time and Time Interval (PTTI) Meeting*, pp. 233–248, Nov. 2007.

6 Conclusion

6.1 Thesis assessment

In this thesis, several innovative miniature microwave cavity solutions have been presented, which were proven useful in at least two scopes of industrial and scientific application.

For the first application, new devices were proposed as microwave front-ends of a short-range radar system for on-line blade tip monitoring in gas turbines (i.e. land-based large-frame turbines at 6 GHz, aero-derivatives and aero-engines at 24 GHz).
In general, microwave probes are advantageous for blade tip sensing: contrary to other existing techniques, they can survive to high temperatures for extended period of operation, unaffected by contaminants, like gases and dust particles. Nonetheless, the microwave front-end of such systems is of difficult implementation, due to the demanding thermo-mechanical constraints of the specific field of application (i.e. a large temperature change, the presence of vibrations) and the tight requirements on the size of the probe. At the beginning of this research work, antenna-based tip monitoring probes have been studied. These probes were found to suffer from a certain structural complexity, and with radiation characteristics that are not entirely well suited for short range sensing. Finally, resonator-based probes were found to represent a more practical alternative, thanks to an improved compromise between robustness, miniaturization and simplicity of operation.

These topics are described in more detail through Chapter 2, where a state-of-the-art of existing techniques for blade tip monitoring is provided and the microwave sensing system considered in this work is presented [1]. Then, an overview on the operating principles of the considered antenna sensors (based on a miniature patch antenna and a miniature PIFA) and resonator based sensors (an open-ended waveguide resonator probe and an open-ended coaxial resonator probe) is given, along with some possible general remarks regarding the suitability of the two approaches for the implementation of blade tip monitoring microwave probes.

Chapter 3 addresses the implementation of a number of possible solutions for the microwave front-end of the blade tip monitoring system. First, an existing 5.8 GHz patch antenna probe [2] is presented. The behavior of such probe was investigated in detail in order to foresee possible new designs. Second, a 24 GHz miniature PIFA probe [3] is proposed as a new antenna-based solution. This approach has allowed to achieve great miniaturization with reduced complexity compared to the existing patch probe. Results from simulated

models were found very promising and room temperature prototypes were built for testing. Measurements evidenced, however, an important sensitivity of the PIFA prototypes to temperature variations. Moreover, manufacturing tolerances did not allow repetitive results, and the proposed solution was not considered for high temperature validation.
Finally, two cavity-based probe solutions are proposed, namely a miniature 24 GHz waveguide resonator probe and a 6 GHz coaxial resonator probe [4, 5]. Tests in laboratory and on real turbine engines demonstrated the suitability of such devices for the aimed application and confirmed significant performance and reliability improvements with respect to other comparable techniques, like antenna-based and eddy-current sensors.

Within the second application, new solutions are proposed as miniature microwave cavities for scientific instruments, such as Rubidium (Rb) atomic clocks and quantum sensors.
Atomic clocks based on Rb frequency standard are low cost and can achieve an interesting short-term stability, so that they are very attractive for many commercial, portable and aerospace applications. Attempts to miniaturize such kind of systems are usually limited by the dimensional constraints of standard microwave cavity resonators (MWR), which account for a large part of the volume of the physics package.
In Chapter 4, the Rubidium atomic clocks principle of operation and a number of existing solutions for the conception of compact MWRs for miniature Rb clocks are reviewed along with the requirements and theoretical aspects related to the implementation and the miniaturization of the MWRs. In particular, a theoretical model of the resonator structure known as Loop-Gap Resonator (LGR) [6, 7] is presented and discussed, in order to understand the principle of operation of the μ-LGR solution proposed in Chapter 5.

Chapter 5 proposes a new miniature MWR based on a loop-gap resonator structure, also referred to as the μ-LGR [8, 9]. This cavity design, conceived to enclose 3D microfabricated cells [10], was proven to meet the required specifications for the atomic clock operation, achieving an interesting size-reduction. Its suitability for integration in a miniature Rb atomic clock was demonstrated in the frame of a laboratory atomic clock experiment, where the Rb miniature atomic clock, integrating the μ-LGR and the 3D micro-cell, achieved unmatched short-term stability [11] compared to other clocks using microfabricated cells.
Finally, a planar miniature MWR is proposed, which is conceived for the integration of 2D microfabricated cells. Simulation results have provided very promising results, and encourage further investigation on this possible solution.

6.2 Perspectives

This thesis has proposed several innovative solutions for the implementation of miniature microwave cavities, useful for at least two industrial and scientific applications. The development of these solutions suggested new ideas, open issues and potential improvements

that are discussed in the following paragraph.

6.2.1 Microwave Solutions for Rotating Machinery Health Monitoring

- A simple but rigorous model of the operation of open-ended resonator-based probes is proposed in Section 2.7.2.6. This model may provide a deeper insight of the behavior of the proposed resonator-based sensors, that could enable a more accurate prediction of the nature of the blade-probe interaction. However, a meticulous model of the turbine environment of operation is needed to estimate the sensor response with increased accuracy.

- In this work, a probe based on an open-ended circular waveguide working in its fundamental TE_{11} mode is proposed. In general, the operation of this sensor is very sensitive to the polarization of the fields at its open end. Alternatively, other field distributions different from the TE_{11} mode are also supported by the circular waveguide (higher order modes) and their impact on the operation of the sensor is considered to deserve further investigation (i.e. modes with azimuthal symmetry). However, as the frequency increases with the mode order, larger resonant cavities should be considered.

- While the presented open-ended coaxial resonator probe solution is designed for the working frequency of 6 GHz, a smaller version of the coaxial probe was attempted for operation at 24 GHz. However, the simulated probe models showed a considerable sensitivity to small geometric variations, so that further investigation on more stable solutions is desirable.

6.2.2 Miniature MWR Solutions for Rubidium Atomic Clocks

- The proposed μ-LGR metallic enclosure is a simple brass box sealed by screwed caps. However, a size reduction of the enclosure is considered to be possible, with the use of different manufacturing techniques and/or materials.

- In this work, we proposed an effective and simple method for the fine-tuning of the μ-LGR, consisting of adjustable tuning screws. Nonetheless, other tuning methods can be sought for, that could also enable for further miniaturization of the cavity enclosure. As an example, one or more tunable capacities could be inserted between the electrodes at one or more stages of the μ-LGR stack.

- The proposed μ-LGR coupling, achieved by a coaxial-fed printed loop provides a practical solution, that enable easy tuning of the loop clearance (with respect to the μ-LGR stack) and loop dimensions (in terms of metallization width and diameter), if needed. However, other coupling methods than the proposed proximity coupling could be considered, that may also enable further miniaturization of the μ-LGR cavity (e.g. merging of the coupling device with the μ-LGR stack).

- With the use of suitable manufacturing techniques and/or materials, a further miniaturization of the proposed MWR solutions may be achieved by merging the resonator electrodes within the Rubidium cell cavity walls.

Bibliography

[1] J. L. Geisheimer *et al.*, "Phase-based sensing system," *United States Patent No. 7,283,096*, December 3, 2002.

[2] J. L. Geisheimer, S. A. Billington, D. Burgess, and G. Hopkins, "Microstrip patch antenna for high temperature environments," *United States Patent No. 7,283,096*, October 16, 2007.

[3] M. Violetti, J.-F. Zürcher, J. Geisheimer, and A. K. Skrivervik, "Design of antenna based sensors for blade tip clearance measurement in gas turbines," in *Proc. 4th European Conference on Antennas and Propagation*, 12-16 April, Barcelona, Spain 2010.

[4] M. Violetti, A. K. Skrivervik, Q. Xu, J. Geisheimer, and G. Egger, "Device and method for monitoring rotor blades of a turbine," *European Patent Application No. 11181622*, Sept. 16, 2011.

[5] M. Violetti, Q. Xu, M. Hafner, and A. K. Skrivervik, "New microwave sensing system for blade tip clearance measurement in gas turbines," *to be presented to IEEE Sensors Conference*, Oct. 28–31, 2012, Taipei, Taiwan.

[6] W. Froncisz and J. S. Hyde, "The loop-gap resonator: a new microwave lumped circuit ESR sample structure," *J. Magn. Reson.*, vol. 47, pp. 515–521, 1982.

[7] M. Mehdizadeh, T. Ishii, J. Hyde, and W. Froncisz, "Loop-gap resonator: a lumped mode midrowave resonant structure," *IEEE Trans. Microw. Theory Tech.*, vol. 31, pp. 1059–1064, 1983.

[8] M. Violetti, C. Afforderbach, F. Merli, G. Mileti, and A. K. Skrivervik, "Microwave resonator, quantum sensor, and atomic clock," *European Patent Application No. 12155696*, February 16, 2012.

[9] M. Violetti, M. Pellaton, C. Affolderbach, F. Merli, M. G. Zürcher, and A. K. Skrivervik, "New miniaturized microwave cavity for rubidium atomic clocks," *to be presented to IEEE Sensors Conference*, Oct. 28–31, 2012, Taipei, Taiwan.

[10] Y. Pétremand, C. Affolderbach, R. Straessle, M. Pellaton, D. Briand, G. Mileti, and N. F. De Rooij, "Microfabricated rubidium vapour cell with a thick glass core for small-scale atomic clock applications," *J. Micromech. Microeng.*, vol. 22(2), 025013, 2012.

[11] T. Bandi, M. Pellaton, D. Miletic, C. Affolderbach, F. Gruet, R. Matthey, G. Mileti, C. Stefanucci, M. Violetti, F. Merli, J.-F. Zürcher, and A. K. Skrivervik, "Double resonance in alkali vapor cells for high performance and miniature atomic clocks," in *Proc. IEEE International Frequency Control Symposium, IFCS*, May 21–24, Baltimore, MD, USA 2012.

Publications

Journal Publications

M. Violetti, Q. Xu, M. Hafnër, J.-F. Zürcher and A. Skrivervik, "New Sensing System for Gas Turbines Health Monitoring", *IEEE Sensors Journal*, in review.

M. Violetti, M. Pellaton, C. Affolderbach, G. Mileti and A. Skrivervik, "Miniature Microwave Cavity for Rubidium Atomic Clocks", *IEEE Transactions on Instrumentation and Measurement*, in preparation.

Conference Publications

M. Violetti, Q. Xu, O. Hochreutiner and A. Skrivervik, "New Microwave Sensor for Online Blade Tip Timing in Gas Turbines", to be presented to *Asia-Pacific Microwave Conference, APMC*, Kaohsiung, Taiwan, Dec. 4–7, 2012.

M. Violetti, Q. Xu, M. Hafnër and A. Skrivervik, "New Microwave Sensing System for Blade Tip Clearance Measurement in Gas Turbines", to be presented to *IEEE Sensors Conference*, Taipei, Taiwan, Oct. 28–31, 2012.

M. Violetti, M. Pellaton, C. Affolderbach, F. Merli, J.-F. Zürcher, G. Mileti and A. Skrivervik, "New Miniaturized Microwave Cavity for Rubidium Atomic Clocks", to be presented to *IEEE Sensors Conference*, Taipei, Taiwan, Oct. 28–31, 2012.

M. Violetti, C. Affolderbach, F. Merli, J.-F. Zürcher, G. Mileti and A. Skrivervik, "Miniaturized Microwave Cavity for Rubidium Atomic Frequency Standards", to be presented to *European Microwave Week, EuMW*, Amsterdam RAI, The Netherlands, Oct. 28–Nov. 2, 2012.

T. Bandi, M. Pellaton, D. Miletic, C. Affolderbach, F. Gruet, R. Matthey, G. Mileti, C. Stefanucci, **M. Violetti**, F. Merli, and J.-F. Zürcher and A. Skrivervik, "Double resonance in alkali vapor cells for high performance and miniature atomic clocks", *in Proc. IEEE International Frequency Control Symposium, IFCS*, Baltimore, MD, USA, May 21–24, 2012.

M. Violetti, Q. Xu and A. Skrivervik, "New Microwave Sensor for Blade Tip Monitoring", *in Proc. 5th EVI-GTI International Gas Turbine Instrumentation Conference*, Munich, Germany, Oct. 10–14, 2011.

M. Violetti, J.-F. Zürcher, J. Geisheimer and A. Skrivervik, "Design of antenna based sensors for blade tip clearance measurement in gas turbines", *in Proc. 5th European Conference on Antennas and Propagation, EuCAP*, Barcelona, Spain, Apr. 12–16, 2010.

Patents

M. Violetti, C. Affolderbach, F. Merli, G. Mileti and A. Skrivervik, "Microwave Resonator, Quantum Sensor, and Atomic Clock", *European Patent application n^o 12155696*, 16 Feb. 2012.

M. Violetti, A. Skrivervik, Q. Xu, J. Geisheimer and G. Egger, "Device and method for monitoring rotor blades of a turbine", *European Patent application n^o 11181622*, 16 Sep. 2011.

List of Acronyms

ACCS	Active Clearance Control System
BTC	Blade Tip Clearance
BTT	Blade Tip Timing
CPT	Coherent Population Trapping
CSAC	Computational Electromagnetics
CTI	Combined Field Integral Equations
CW	Continuous Wave
DR	Double Resonance
DSP	Digital Signal Processing
EGT	Exhaust Gas Temperature
EM	Electromagnetic
EPFL	École Polytechnique Fédérale de Lausanne
FF	Filling Factor
FMCP	Frequency Modulation Capacitive Probe
FNS	Fonds National Suisse
FOF	Field Orientation Factor
GaAS	Gallium Arsenide
HPT	High Pressure Turbine
IFA	Inverted-F Antenna
LGR	Loop-Gap Resonator
LTF	Laboratoire Temps-Fréquence
MMIC	Monolithic microwave integrated circuit

MSA	Microstrip Antenna
MWR	Microwave Resonator
NSMS	Non-Intrusive Stress Measurement System
NTC	Negative Temperature Coefficient
PD	PhotoDetector
pec	perfect electric conductor
PIFA	Planar Inverted-F Antenna
pmc	perfect magnetic conductor
RADAR	Radio Detection and Ranging
RAFS	Rubidium Atomic Frequency Standard
RCS	Radar Cross Section
RF	Radio Frequency
SAR	Specific Absorption Rate
SFC	Specific Fuel Consumption
T/R	Transmitter/Receiver
TE	Transverse Electric
TEM	Transverse Electromagnetic
TM	Transverse Magnetic
ToA	Time of Arrival
TOW	Time-on-Wing
UHF	Ultra High Frequency
UNINE	Université de Neuchâtel
VCO	Voltage-controlled Oscillator
VCSEL	Vertical Cavity Surface Emitting Laser
VNA	Vector Network Analyzer

List of Figures

List of Tables